THESIS

DESIGN, FABRICATION, AND CHARACTERIZATION OF 3D PRINTED CERAMIC SCAFFOLDS FOR BONE REGENERATION

Submitted by

Vail Olin Baumer

Department of Mechanical Engineering

In partial fulfillment of the requirements

For the Degree of Master of Science

Colorado State University

Fort Collins, Colorado

Spring 2024

Master's Committee:

Advisor: David Prawel

Kirk McGilvray
Paul Heyliger

ABSTRACT

DESIGN, FABRICATION, AND CHARACTERIZATION OF 3D PRINTED CERAMIC SCAFFOLDS FOR BONE REGENERATION

Synthetic bone tissue scaffolds are a promising alternative to current clinical techniques for treating critically large bone defects. Scaffolds provide a three-dimensional (3D) environment that mimics the properties of bone to accelerate bone regeneration. Optimal scaffolds should match the mechanical properties of the implantation site, feature a highly porous network of interconnected channels to facilitate mass transport, and exhibit surface properties for the attachment, proliferation, and differentiation of bone cell lineages. 3D printing has enabled the manufacture of complex scaffold topologies that meet these requirements in a variety of biomaterials which has led to rapidly expanding research. Structural innovations such as triply periodic minimal surfaces (TPMS) are enabling the production of scaffolds that are stiffer and stronger than traditional rectilinear topologies. TPMS are proving to be ideal candidates for bone tissue engineering (BTE) due to their relatively high mechanical energy absorption and robustness, interconnected internal porous structure, scalable unit cell topology, and smooth internal surfaces with relatively high surface area per volume. Among the material options, calcium phosphate-based ceramics, such as hydroxyapatite and tricalcium phosphate, are popular for BTE due to their high levels of bioactivity (osteoconductivity, osteoinductivity and osteointegration), compositional similarities to human bone mineral, non-immunogenicity, tunable degradation rates, and promising drug delivery capabilities. Despite the potential for TPMS ceramic scaffolds in BTE, few studies have explored beyond the popular Gyroid topology. Of the many TPMS options, the

Fischer Koch S (FKS) has been simulated to be stronger, be more isotropic, have higher surface area, and absorb more energy than Gyroid at high porosities. In this report, we present a method for photocasting any TPMS in hydroxyapatite which is used to 3D print the first FKS ceramic scaffold. Results indicated that the resolution and accuracy of the process is suitable for BTE, and the custom software for producing the scaffolds was made available to the open-source community. Then, FKS and Gyroid scaffolds were designed to match the properties of trabecular bone using this method for use in critical bone defect repair. The scaffolds were printed and characterized using compressive and flow-based testing to reveal that, while both designs could mimic the low end of natural bone performance, the FKS were 32% stronger and only 11% less permeable than Gyroid. These findings emphasized the need for further characterization of these scaffolds beyond mechanical analysis and into studies of cell growth. To accomplish this, a custom multi-channel perfusion bioreactor was designed to culture cells on these scaffolds to investigate differences in cell behavior with higher efficiency than current designs. The design, capable of culturing many samples simultaneously, was validated using computational fluid dynamics and cell growth assays to demonstrate osteogenic effects and repeatability. In this work, novel TPMS scaffolds were fabricated from hydroxyapatite with sufficient accuracy and quality for large defects, testing of these scaffolds matched trabecular bone performance and suggested that FKS may be superior to Gyroid, and lastly, a four-channel bioreactor system was designed and validated to enable researchers to further characterize scaffolds for BTE.

ACKNOWLEDGEMENTS

I would like to thank my parents Jeff, Jill, and Tracy for providing me with all the opportunities that have brought me here and for always supporting my goals. Additionally, thank you to my siblings, Alyssa, Brick, and India, as well as my friends for the meaning they give to life. And thanks to my partner, Danielle, and our dog Soda, for their continuous love and support.

None of this work would have happened without the guidance and assistance of my advisor, Dr. David Prawel. Thank you for all you have done for my learning and career. I would also like to thank the past students of this lab on which this work was built. And lastly, thank you to my fellow graduate students, Oto, Genesis, and Shashank, and the whole undergraduate team for all the work they did contributing to this work. It could not have happened without each one of you.

TABLE OF CONTENTS

PROLOGUE

My work presented in this thesis is the combination of three independent manuscripts in the field of bone tissue engineering where I was the primary author. The first chapter, titled "ROBOCASTING OF CERAMIC FISCHER–KOCH S SCAFFOLDS FOR BONE TISSUE ENGINEERING", was published in April 2023 to the Journal of Functional Biomaterials. This paper covers the fabrication of our scaffolds. It is essential to understand the accuracy, capabilities, and limitations of your process before moving to any testing. The second chapter, titled "COMPARING FISHER-KOCH-S AND GYROID HYDROXYAPATITE SCAFFOLDS FOR TREATING LARGE BONE DEFECTS", is in review for publication and builds from the previous paper. The purpose of this project was to use our established fabrication process to design and test scaffolds to match structural and functional characteristics of trabecular bone. And lastly, the third chapter, titled "METHODS FOR A MULTI-CHANNEL PERFUSION BIOREACTOR SYSTEM FOR MINERALIZING 3D SCAFFOLDS IN BONE TISSUE ENGINEERING", describes my design and validation of a system to study cell behavior on our scaffolds in an efficient and reproducible way. When I joined our lab, we had no bioreactor system, so it was my responsibility to build one. A bioreactor allows us to characterize the cell behavior of the scaffolds we have designed and fabricated. This last chapter features preliminary data from a draft manuscript intended for publication later this year. Together, these papers detail our approach and my work towards designing, fabricating, and characterizing scaffolds to improve the field of bone tissue engineering.

INTRODUCTION

Critically sized bone defects are a significant and growing healthcare issue that has clear need for improvements in repair techniques. In 2015, 1.5 million Americans were affected by this condition with an associated cost of over a billion dollars in treatments[1]. Critically sized defects typically affect the long bones of the body and are characterized by a loss of bone volume and structure that is so significant that they will never spontaneously heal without surgical intervention[2]. These injuries, often created by impact trauma, bone disease, or a combination of both, have been increasing in occurrence by 25% per decade due to aging populations with longer life expectancies[3]. The current standard of clinical treatment is to secure the long bone with some type of metal stabilizer, such as an intramedullary nail or fixation plate, and then fill the void with grafted bone to initiate healing[4]. However, these techniques have limited success in modern medicine. A systematic review of critical bone defect repairs in 2021 showed that 1 in 6 patients required additional surgeries, 1 in 12 had significant infections, and 1 in 30 had their limb later amputated[5]. Autografts and allografts have limited potential due to their inherent shortcomings. Autografts extract bone from a secondary location on the patient, often from the iliac crest, which restricts the size and shape of harvestable tissue[4]. This method also creates a second surgical site which is also prone to injury and infection, which is evident from the 30% of autograft patients that report chronic pain[6]. Allografts are similarly restricted on harvestable tissue based on donor availability, and on top of that, they add the immune risks associated with foreign transplantation. Lastly, 10% of treatments still report delayed or non-union of the fracture site which means that even though limb function may have been restored, the patient is reliant on the metal stabilizer and may keep it for life[7]. There is a demonstrated need to improve techniques for repairing critical bone defects.

Biomimetic constructs in the form of 3D printed scaffolds have emerged as a viable solution to replace bone grafts. Scaffolds, like grafts, serve as a 3D support structure inside the void of a large defect to guide cell migration, proliferation, and differentiation[6]. Ideal scaffolds mimic many of the properties of trabecular bone to accelerate the body's own healing process. Optimal scaffolds should be biocompatible to avoid adverse immune responses, biodegradable to allow for tissue in-growth and replacement, feature a highly porous network of interconnected channels to facilitate mass transport, have attractive surface properties for bone cells, and have mechanical properties that match the implantation site[6]. 3D printing can produce complex structures in a variety of biomaterials that meet these requirements while alleviating many shortcomings of grafts[8]. 3D printing provides a reliable method for producing large scaffolds that can be customized to the patient, tissue, and anatomical location for highly specific solutions. Despite the advantages of synthetic scaffolds, clinical use has not been fully adopted and few grafting alternatives are commercially available[9]. In addition to securing regulatory approval, the performance and economics of scaffolds must surpass that of grafts to see a true transformation of bedside procedures[6]. Fracture healing can be described using the diamond model which states that success is driven by four main factors: osteogenic cells, osteoconductive scaffolds, growth factors, and mechanics[10]. Researchers are investigating scaffold applications from all these angles to maximize osteogenic effects and accelerate translation, but this work will specifically focus on just one aspect: osteoconductive scaffolds. Scaffold design in this context is fundamentally driven by the fabrication method, material selection, and macro-structure. This report will explore our lab's novel approach using these drivers to fabricate and test highly bioactive scaffolds for use in critical bone defect repair. This work is broken down into three independent manuscripts which each contribute insights and tools to the bone tissue engineering

community on the design, manufacture, and characterization of our 3D printed ceramic scaffolds. The first chapter presents our low-cost method for 3D printing a highly desirable and complex structure, the Fischer Koch S (FKS), using a calcium phosphate-based material, hydroxyapatite. Therein, the resolution, accuracy, and challenges of the process are discussed in depth. The second chapter explores the performance of the FKS scaffold in the context of regenerating large bone defects using a popular industry structure, the Gyroid, as a control. And lastly, the third chapter describes the methods and validation of a bioreactor system capable of characterizing the *in vitro* cell growth on these, or any scaffold structure, for predicting *in vivo* performance.

References

[1] B.-N. B. Nguyen, H. Ko, R. A. Moriarty, J. M. Etheridge, and J. P. Fisher, "Dynamic Bioreactor Culture of High Volume Engineered Bone Tissue," *Tissue Engineering Part A*, vol. 22, no. 3–4, pp. 263–271, Feb. 2016, doi: 10.1089/ten.tea.2015.0395.

[2] M. Panagiotis, "Classification of non-union," *Injury*, vol. 36, no. 4, Supplement, pp. S30–S37, Nov. 2005, doi: 10.1016/j.injury.2005.10.008.

[3] R. Burge, B. Dawson-Hughes, D. H. Solomon, J. B. Wong, A. King, and A. Tosteson, "Incidence and economic burden of osteoporosis-related fractures in the United States, 2005-2025," *J Bone Miner Res*, vol. 22, no. 3, pp. 465–475, Mar. 2007, doi: 10.1359/jbmr.061113.

[4] L. Vidal, C. Kampleitner, M. Á. Brennan, A. Hoornaert, and P. Layrolle, "Reconstruction of Large Skeletal Defects: Current Clinical Therapeutic Strategies and Future Directions Using 3D Printing," *Front. Bioeng. Biotechnol.*, vol. 8, p. 61, Feb. 2020, doi: 10.3389/fbioe.2020.00061.

[5] H. Bezstarosti *et al.*, "Management of critical-sized bone defects in the treatment of fracture-related infection: a systematic review and pooled analysis," *Arch Orthop Trauma Surg*, vol. 141, no. 7, pp. 1215–1230, Jul. 2021, doi: 10.1007/s00402-020-03525-0.

[6] J. Henkel *et al.*, "Bone Regeneration Based on Tissue Engineering Conceptions — A 21st Century Perspective," *Bone Res.*, vol. 1, no. 3, pp. 216–248, Sep. 2013, doi: 10.4248/BR201303002.

[7] D. J. Hak *et al.*, "Delayed union and nonunions: Epidemiology, clinical issues, and financial aspects," *Injury*, vol. 45, pp. S3–S7, Jun. 2014, doi: 10.1016/j.injury.2014.04.002.

[8] S. Bose, D. Ke, H. Sahasrabudhe, and A. Bandyopadhyay, "Additive manufacturing of biomaterials," *Progress in Materials Science*, vol. 93, pp. 45–111, Apr. 2018, doi: 10.1016/j.pmatsci.2017.08.003.

[9] M. Govoni, L. Vivarelli, A. Mazzotta, C. Stagni, A. Maso, and D. Dallari, "Commercial Bone Grafts Claimed as an Alternative to Autografts: Current Trends for Clinical Applications in Orthopaedics," *Materials*, vol. 14, no. 12, Art. no. 12, Jan. 2021, doi: 10.3390/ma14123290.

[10] P. V. Giannoudis, T. A. Einhorn, and D. Marsh, "Fracture healing: The diamond concept," *Injury*, vol. 38, pp. S3–S6, Sep. 2007, doi: 10.1016/S0020-1383(08)70003-2.

CHAPTER 1: ROBOCASTING OF CERAMIC FISCHER–KOCH S SCAFFOLDS FOR BONE TISSUE ENGINEERING

2.1 Introduction

Bone fractures are a significant and growing healthcare issue in the United States. Poor healing of large bone defects is one of the biggest challenges in human orthopedic medicine, affecting more than 1.5 million Americans per year and often leading to infections, reoperations, poor functional outcomes, and ultimately, all too often, limb loss [1]. In 2015, this resulted in significant personal and economic costs of more than $1 billion [1]. By 2025, these figures are expected to rise by 50% [2]. Furthermore, additional indirect costs due to productivity loss are estimated at 42% of the direct expenditure on average. These indirect costs more than double for patients experiencing delayed or non-union healing [3]. Populations over 50 years of age experience these fractures more often than their younger counterparts, and fracture rates increase exponentially between ages 50 and 85 [4]. Extended life expectancies paired with bone diseases such as osteosarcoma and osteoporosis further contribute to this increased fracture rate and emphasize the importance of new therapeutic techniques.

Autologous bone grafting is the current gold standard procedure to remediate large bone defects, but reported outcomes are too often unsatisfactory. Healing strategies using bone grafts and bone fillers exhibit recurring failures with non-union rates as high as 21% [5], and complication rates of 50% due to delayed or non-union, 30% from allograft fracture, and 15% from infection [6]. Autografts are limited by availability and the size of harvestable tissue, and they create two surgical sites that are prone to injury, infection, and significant patient discomfort [7]. Synthetic scaffolds have emerged in recent decades as promising alternatives to bone grafting because they address some of these shortcomings.

Three-dimensional (3D) printing of scaffolds for bone tissue engineering (BTE) is a leading method to replace bone grafts [7] and is under significant investigation in pre-clinical settings [8]. Successful BTE scaffolds should be biocompatible, with surface characteristics that promote cell adhesion (osteoconductivity), proliferation (osteoinductivity) and mineralization (osteointegration). To meet these requirements, synthetic scaffolds have been produced in countless materials from metals such as titanium and ceramics such as calcium-phosphate-based materials to composites such as bioglass and polymeric blends [9]. Among these options, calcium phosphate-based materials, such as hydroxyapatite (HAp) and tricalcium phosphate (TCP), are popular for BTE due to their biocompatibility, high levels of bioactivity (osteoconductivity, osteoinductivity and osteointegration), compositional similarities to human bone mineral, non-immunogenicity, tunable degradation rates, and promising drug delivery capabilities [10]–[14]. 3D printing of ceramics has shown great potential, but the fabrication and design methodologies used in 3D printing remain limited in their ability to produce large-sized scaffolds for load bearing cases [15]–[17]. More research is needed into ceramic scaffold structure and fabrication.

To improve ceramic scaffolds, their complex requirements of porosity, interconnectivity, and strength to remediate large bone defects must be understood. BTE scaffolds attempt to replicate the properties of bone tissue surrounding a defect to encourage the body's natural healing process. Scaffolds should have a high porosity to mimic natural trabecular bone, which has a honeycomb-like internal structure with a porosity range of 50–90%, depending on the anatomical location [18]. The porous interior of BTE scaffolds should form a continuous network to accelerate the mass transport of nutrients, gases, and waste, thus augmenting the bone remodeling process [19]. Scaffolds lack the vasculature of autologous bone, making them solely dependent on diffusion for mass transport. This emphasizes the need for high levels of permeability [20], which is used as a

functional representation of porosity, pore size, pore shape, tortuosity, and interconnectivity [21]. Lastly, scaffolds require structural integrity as regeneration processes develop new bone. However, the pore size, volume fraction, and porosity ranges required for ideal bioactivity are also associated with fairly poor mechanical properties [19], [22]–[24]. Consequently, BTE scaffolds must balance mechanical properties (compression, stiffness and elasticity) against interconnectivity, porosity, and pore size to optimize for each application and the associated load bearing requirement [25], [26]. Considerable progress has been made using ceramic and polymer/ceramic composite BTE scaffolds in critical defect healing, as demonstrated by recent *in vivo* studies [27]–[30]. But the challenge of complete bridging, integration and union remains for human-scale load-bearing cases.

Structural innovations such as triply periodic minimal surfaces (TPMS) are enabling the production of scaffolds that are stiffer and stronger than traditional rectilinear topologies [31]–[35]. TPMS are implicit functions with infinitely stackable 3D unit cells and relatively high porosity and strength per volume, which are proving to be ideal candidates for BTE due to their relatively high mechanical energy absorption and robustness, interconnected internal porous structure, scalable unit cell topology, and smooth internal surfaces with relatively high surface area per volume [31], [32], [36]. The TPMS function has zero mean curvature, which creates a continuous interior devoid of sharp corners and junctions within each unit cell. Additionally, the parameters can be adjusted to achieve specific porosities, pore sizes, shapes, permeability, and tortuosity that are favorable for BTE scaffolds [35], [37]–[43]. A depiction of popular TPMS unit cells in BTE are shown in Figure 1 [39].

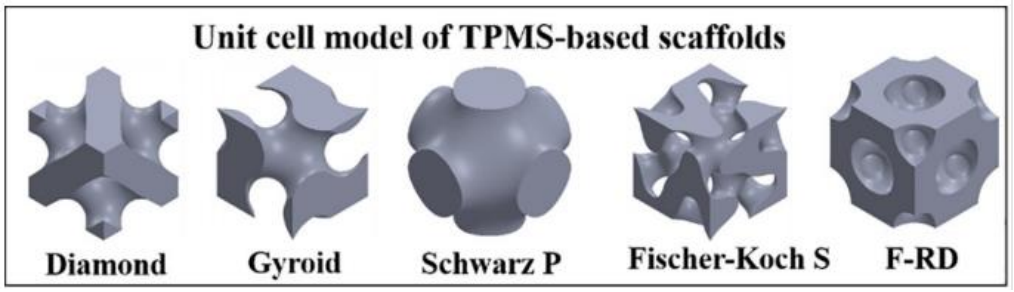

Figure 1. Visualization of popular TPMS scaffold unit cells [39].

Advanced fabrication techniques such as additive manufacturing (a.k.a. 3D printing) are ideally suited to precisely and accurately reproduce the geometric and topological design constraints of TPMS scaffolds for BTE [9], [14], [44]. Numerous researchers have 3D printed gyroid and other TPMS structures using powder-bed fusion (PBF). Abueidda et al. used PBF to 3D print gyroid scaffolds in nylon to study their mechanical properties [32]. Abou-Ali et al. fabricated four different types of TPMS structures, including gyroid and Fischer–Koch S (FKS), in nylon using PBF in order to study TPMS mechanical properties [45]. In other applications of PBF, Maskery et al. manufactured gyroids composed of aluminum alloys [46] and other TPMS, including gyroids but not FKS, from nylon [47], also to study the mechanical properties of these scaffolds. Castro et al. printed three types of TPMS structures, including gyroid but not FKS, using vat photopolymerization to confirm their finite element simulation with mechanical behavior [48]. Melchels et al. 3D printed gyroid structures using vat photopolymerization to study the effects of scaffold architecture on cell proliferation [49]. Santos et al. studies the effects of permeability and porosity on four different TPMS structures (not including FKS) that were 3D printed using material jetting of a commercial photopolymeric material. [50] Many researchers have 3D printed gyroid and other TPMS (not FKS) structures by melt extruding poly-lactic acid (PLA), acrylonitrile butadiene styrene (ABS), and other materials [33], [51], [52]. The majority of research with FKS

has been limited to computer simulation. Numerous researchers included FKS in their finite element analysis (FEA) and computational fluid dynamics (CFD) modeling of TPMS structures [35], [39], [53].

Work with ceramic materials using TPMS is comparatively limited. The Bose group used a binder jetting 3D-printing process to study pore size and pore volume effects on alumina and TCP gyroid scaffolds [23] and the mechanical and biological properties of HAp gyroid scaffolds [54]. In another study, Restrepo et al. used robocasting with an unspecified "conventional commercial ceramic paste" in their study of mechanical properties of three ceramic TPMS structures (not including FKS) [55]. The limited application of TPMS with ceramics results from challenges in production of these complex structures. Resources for creating printable gcode for FKS and other non-gyroid TPMS are non-existent, exclusive of proprietary software that is mostly bundled with expensive 3D printers, and which generally use proprietary cytotoxic materials. Conversely, gyroids are core infill patterns in popular 3D-printing slicers such as Ultimaker Cura (Ultimaker B.V., Utrecht, Netherlands), and embedded topologies in CAD platforms such as Creo (Parametric Technologies Corp., Boston, MA, USA) and topology optimization tools such as nTopology (nTopology Inc., New York, NY, USA).

Robocasting is a promising method for fabricating ceramic BTE scaffolds because it is very low cost, easy to use, can create high-precision objects, and requires small amounts of ceramic material. The method uses evaporative processes to remove liquified polymeric or aqueous materials, within which, powdered solid content is carried to form the object. High solid loading required for mechanical strength is challenged by significant shrinkage and cracking that result from evaporation of these liquid carriers. Moreover, large overhangs are difficult to fabricate due to longer "drying" times as the solvent carriers dissipate. Such overhangs usually require sacrificial

supports that cannot be removed within the scaffold structure, which limits the ability of robocasting to form complex 3D objects with good structural strength, topological complexity, and model fidelity, which also contain completely bridged overhangs (e.g., interconnected pores). Complex structures such as TPMS scaffolds require the ability to print slurries without supports, and the viscous extruded material must harden quickly with limited shape distortion. From these challenging requirements a new approach has emerged that combines photopolymerization with robocasting in which layers are cured layer-by-layer as they are printed, eliminating the need for support material, and enabling fabrication of highly complex, high precision structures. We refer to this method as "photocasting." Faes et al. was the first to use this approach to fabricate featureless slabs of yttrium-stabilized Zirconia [56]. Asif et al. [57] and Farahani et al. [58] produced basic structures consisting of a photopolymeric resin containing fumed silica particles. We used photocasting to print gyroids for BTE in earlier work [59], [60].

It has been suggested that some TMPS topologies might be better suited to particular applications. Lu et al. presented computer simulations comparing the properties of different TPMS topologies, including FKS [39]. Their finite-element analysis suggested the FKS topology may be better suited to remediate a cortical diaphyseal bone defect due to its isotropic behavior, even at high porosities [61]. Because cortical bone can be modeled as an isotropic tissue in certain defects, the specific properties of FKS might be better suited to this application than other TPMS, such as gyroid scaffolds. Similarly, they proposed that gyroid scaffolds might be better suited to procedures such as epiphyseal tibial tuberosity advancement, where the higher anisotropic properties of the gyroid may be preferable to match the anisotropic mechanical behaviors of cancellous bone [61]. Lu concludes that the FKS topology "may be the most favorable one in the scenarios where nutrient is not limiting, e.g., in the application of bone fusion." Yet, the characteristics of FKS ceramic

scaffolds have yet to be explored in the context of BTE, probably due in large part to the production issues mentioned above. To the best of our knowledge, no one has 3D printed FKS scaffolds in calcium phosphate-based materials. Abou-Ali [45] appears to be the only researcher to have actually 3D printed FKS, but not for a BTE application and using an expensive, commercial photopolymer printer and a material that is unlikely to be biocompatible.

This paper addresses clear roadblocks to producing FKS and other TPMS scaffolds by developing and utilizing open-source software on low-cost 3D printers to produce ceramic scaffolds with features in the requirement range for BTE. The purpose of our work is to enable experimentation and innovation with FKS and other TPMSs by more researchers, not the optimization of ceramic FKS scaffolds for BTE. We report on a software algorithm that we developed to create 3D printable scaffold models for TPMS such as FKS and gyroids and any continuous differentiable implicit function representation, also including spheres, ellipsoids, and conic sections. We contributed the software to the open-source community so that others can model and print these complex topologies, along with mixed and functionally graded topologies. We then used this algorithm to 3D print FKS scaffolds for BTE using photocasting. In addition, we evaluated the accuracy of our fabrication process in the context of BTE for dimensional control, porosity, pore size, and surface texture.

2.2 Materials and Methods

2.2.1 Creating a Flexible, Customizable 3D TPMS Model for BTE

To generate the Fisher–Koch S triply periodic minimal surface, the trigonometric approximation in Equation (1) was applied. This approximation is an implicit function where the surface is defined to exist when $fks(x, y, z) = 0$.

$$fks(x, y, z) = \cos(2x)\sin(y)\cos(z) + \cos(2y)\sin(z)\cos(x) + \cos(2z)\sin(x)\cos(y) \quad (1)$$

A mathematical surface has zero thickness and must be converted to a solid volume for realization. The sheet solid methodology was used where the surface was continuously expanded in opposing normal directions to create a uniform thickness centered on the curvature. To tune scaffold properties for BTE, a method was needed to create FKS objects with a variable thickness (k) divided into (m) number of material deposition paths because the ratio of k/m could be set to the extruder nozzle width for optimal slicing, and therefore optimal build quality. Furthermore, the material deposition paths must remain parallel for cohesive layers to form. However, offsetting an implicit surface by adding a constant k is insufficient for the trigonometric TPMS approximation functions, as the method does not offset the surface by a uniform distance. This results in filament deposition paths that both diverge and converge, leading to cavities and overlapping filament. Additionally, the offset surface is not centered around the desired distance k, causing the average filament line spacing to be incorrect for the desired line width. See Figure 2 for an illustration of these issues.

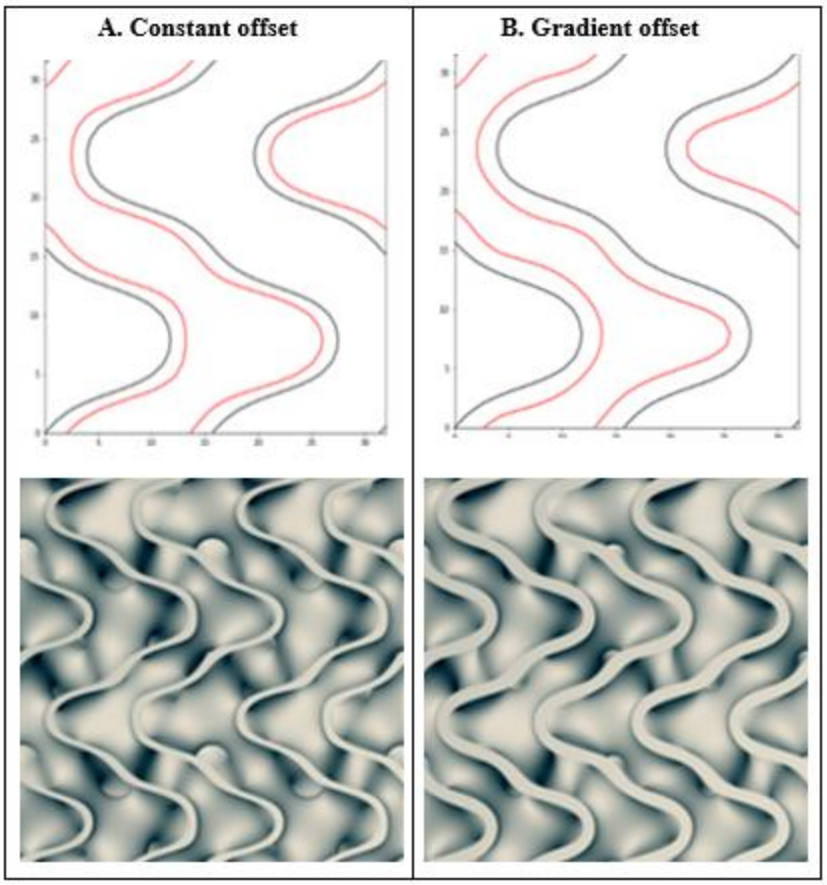

Figure 2. The top images show a two-dimensional slice of Fisher–Koch S at z = 0 and offsets k = 0.0 in black and k = 0.4 in red. The bottom images show a 3D rendering of FKS shelled using the respective methods. (A) The constant offset method with high variance in offset distance and incorrect line spacing. (B) Geier's gradient offset method with uniform offset distance and incorrect line spacing.

Geier et al. proposed a method of surface offsetting with significantly reduced line spacing variance by adding the magnitude of the gradient vector of the surface to the original implicit function [62]. This method works because the gradient is a proxy for the normal of a surface and it can be shown that the gradient and normal vectors are coaxial. While this first order approximation, as the offset k grows, is still prone to the same errors that are seen in the simple offset method previously mentioned, we found that the errors were significantly smaller with the Geier method, as visualized in Figure 2. For FKS, we added the gradient of Equation (2) and

multiplied it by k, as shown in Equation (3).

$$\nabla fks(x,y,z) = \left(\frac{\partial fks(x,y,z)}{\partial x}, \frac{\partial fks(x,y,z)}{\partial y}, \frac{\partial fks(x,y,z)}{\partial z}\right) \quad (2)$$

$$fks_{offset}(x,y,z,k) = fks(x,y,z) - k|\nabla fks(x,y,z)| \quad (3)$$

Using the FKS approximation and offset function, the surface was generated and discretized into a non-manifold triangulated mesh by a commonly used marching cubes iso-contouring algorithm. The algorithm works by first generating a level set of the function, finding the points that intersect the zero level at neighboring cells, and finally, triangulating the points of a cell using a lookup table. In order to modify the mesh for BTE scaffolds, an open-source python GUI application [63] that used the Vedo python library [64] was built for customization, visualization, and mesh processing. This exportable mesh was designed to leverage the 'Surface Mode' of the Ultimaker Cura slicing software to repair gaps and slice the object into universal gcode instructions for viscous extrusion by our 3D printer(s).

The GUI is demonstrated in Figure 3, which shows that users can select a TPMS topology and then adjust the dimensions, periodicity, road width, and road count to a custom porosity calculated according to Equation (4). The designed porosity of a TPMS scaffold (ϕ_d) can be estimated by dividing the estimated void volume, V_v, of the scaffold by the total volume of the scaffold, V_t. In our case, the total volume is the volume of the cube. We approximate the void volume by discretizing the domain into individual cells of volume, V_c, and then multiplying that volume by the number of cells, c , that exist outside the mesh, as shown in Equation (5). The cell size was decreased until the solution converged.

$$\phi_d\ \% = \frac{V_v}{V_t} * 100\% \quad (4)$$

$$V_v = c \cdot V_c \tag{5}$$

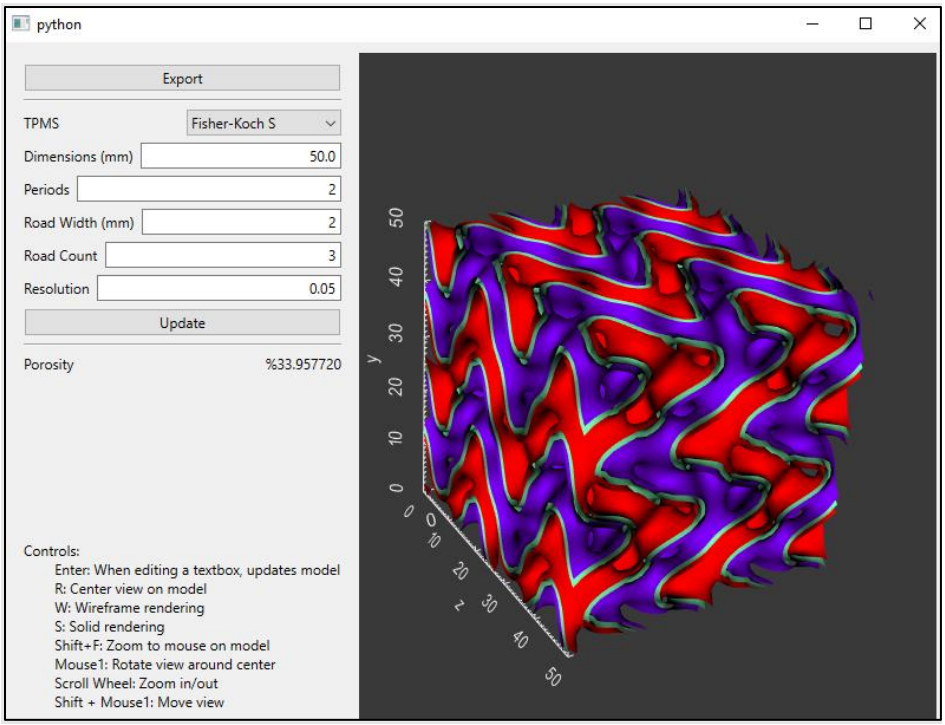

Figure 3. A GUI produced from the open-source code allows users to select TPMS topologies of FKS or Gyroid and adjust the properties for BTE scaffold cubes. The surface can then easily be exported as an STL file for further processing.

The pore size in the context of BTE was defined as the diameter of the most constricted region on a 2D slice (in the XY plane), which was measured on the model of the exported mesh. For FKS specifically, there are multiple such regions where interconnected pores constrict to a circular cross section. Within the GUI, pore size can be adjusted by varying periodicity and wall thickness, where wall thickness is defined as the product of the road width and road count.

2.2.2 Scaffold Fabrication

Using the FKS program described earlier, 1.4 periods of the FKS function were distributed over a 12 mm side length to result in cubic scaffolds with an as-designed porosity of 73.71%. This was selected to be in the middle of the approximate 50–90% range used in BTE. A single road

width of 0.413 mm, equal to the nozzle diameter, was used in the design. These properties are herein referred to as the "as-designed" characteristics. In prior work [60] the sintering process showed an isotropic shrinkage of approximately 21% for HAp gyroid scaffolds. This shrinkage is an expected part of the process and will be analyzed for FKS scaffolds. The expected shrinkage influenced the choice for a designed 12 mm cube, thus targeting final as-sintered dimensions of roughly 10 mm × 10 mm × 10 mm.

For ceramic photocasting, a viscous mixture, referred to in this report as a slurry, was prepared to suspend needle-like HAp particles (Macron Fine Chemicals, Avantor, Radnor, PA, USA) in 99% pure ethylene glycol dimethacrylate (EGDMA, Scientific Polymer Products, Inc., Ontario, NY, USA) to enable controlled viscous extrusion. A photoinitiator, diphenyl(2,4,6-trimethylbenzoyl)phosphine oxide(TPO, TCI America, Portland, OR, USA) was added to permit later photocuring, and a commercial anionic dispersant, Solplus D540 (Lubrizol Advanced Materials Inc., Wickliffe, OH, USA), was added to reduce viscosity by dispersing the HAp particles in the monomer. The slurry composed of EGDMA, TPO, and D540 was then mixed with agate milling media in Teflon® jars on a planetary ball mill (Across International, Davie, FL, USA) at 120–360 rpm, depending on process cycle, for several hours, while gradually adding additional HAp powder until a homogenous slurry with 41% volume HAp was achieved. The final slurry was then sealed in an airtight, opaque jar to avoid vaporization of EGDMA and premature photocuring until the 3D-printing process occurred.

FKS scaffolds were photocast using a Hyrel Hydra (Hyrel 3D, Norcross, GA, USA) 3D printer. The slurry was loaded into a syringe print head assembly (HyRel EMO-XT print head) with a 22-gauge (0.413 mm) tip under limited light exposure, and then transferred to the printer. The print bed was covered with painter's tape to improve bed adhesion and to prevent reflected

light from prematurely curing slurry in the nozzle. The FKS scaffold g-code was uploaded to the printer and a ring LED surrounding the print nozzle was activated at 405nm wavelength to produce an exposure of 0.91 mW/cm^2. The printer executed the machine code with continuous material deposition and layer-wise photopolymerization until the build was completed. Lastly, the scaffold was post-cured under LED for an additional 3 min before it was stored in darkness prior to subsequent sintering. The intermediate 3D-printed, but not yet sintered, scaffold is referred to as a "green body" and its dimensions are "as-printed."

Green body scaffolds were sintered to remove organic content and to densify the HAp within the scaffold struts. Scaffolds were heated in a muffle furnace (Barnstead/Thermolyne 47900, Ramsey, MN, USA) at a ramp rate of 5 °C/min up to 1200 °C, and then held for 3 h. Thermogravimetric analysis confirmed in prior work that all polymeric content was removed [60]. The furnace cooled to ambient temperature, and the scaffolds were transferred to a cool, dry location to await characterization. These "as-sintered" scaffolds are the final product that were then used in further experimentation.

2.2.3 Characterization of Manufactured Scaffold Structure

The "accuracy" of the 3D-printing process is defined as the fidelity of the 3D-printed model to the original 3D CAD model in the principal axes. Thirteen scaffold cubes were measured in three axes using calipers at the green body "as-printed" stage and at the final "as-sintered" stage to be compared against the as-designed (CAD) side length defined in the FKS software. The XY plane was denoted as the coordinate plane for each layer, and the Z axis described the vertical build direction.

Micro-computed tomographic (micro-CT) imaging using a Scanco 80 (Scanco Medical AG, Bruttisellen, Switzerland) measured global scaffold porosity, pore size, and wall thickness of three

sintered FKS scaffolds. In the Scanco 80 Visualizer, a pre-existing setting designed to scan porous, bone-like materials was used, and four key measurements were recorded from each scan: Total Volume (TV), Filled Volume (FV), Trabecular Thickness (Tb.Th), and Trabecular Spacing (Tb.Sp). The TV is manually selected as a region of interest and defines the nominal volume occupied by the scaffold under analysis. FV is the volume of ceramic component above a minimum density within the TV. TV and FV were used to determine sintered porosity (ϕ_s) using Equation (5).

$$\phi_s\ \% = \left(1 - \frac{TV}{FV}\right) * 100\% \tag{6}$$

Tb.Th is equivalent to the average wall thickness in 3D, and Tb.Sp describes the average spacing of those walls. Pore size was defined as the major and minor diameters of an ellipse that is compared with the most constricted pores in the XY plane. Measurements were taken using Image J [65] on 2D images from the scan data at six equally spaced slices in the Z direction per scaffold. The solid model generated from the scan data was further used to study the fidelity of the printed FKS topology and to view internal morphology.

Scanning Electron Microscopy (SEM) on a JEOL JSM-6500F field emission scanning electron microscope (JEOL, Peabody, MA, USA) was utilized to observe the printed surface microstructure and morphology and to visualize the interfacial boundary region between roads. Scaffold samples were coated with 10nm of gold using a Denton Vacuum Desk II Gold Sputter Coater (Denton Vacuum, Moorestown, NJ, USA) and imaged at 10 to 15kV.

2.3 Results

2.3.1 Scaffold Fabrication

Figure 4 graphically diagrams the complete workflow through selecting parameters in the GUI, exporting the STL, slicing in Ultimaker Cura, and lastly, 3D printing. This workflow resulted in consistent fabrication of FKS scaffolds, an example of which is shown in Figure 4E, that accurately represented the as-designed scaffolds, as reported below.

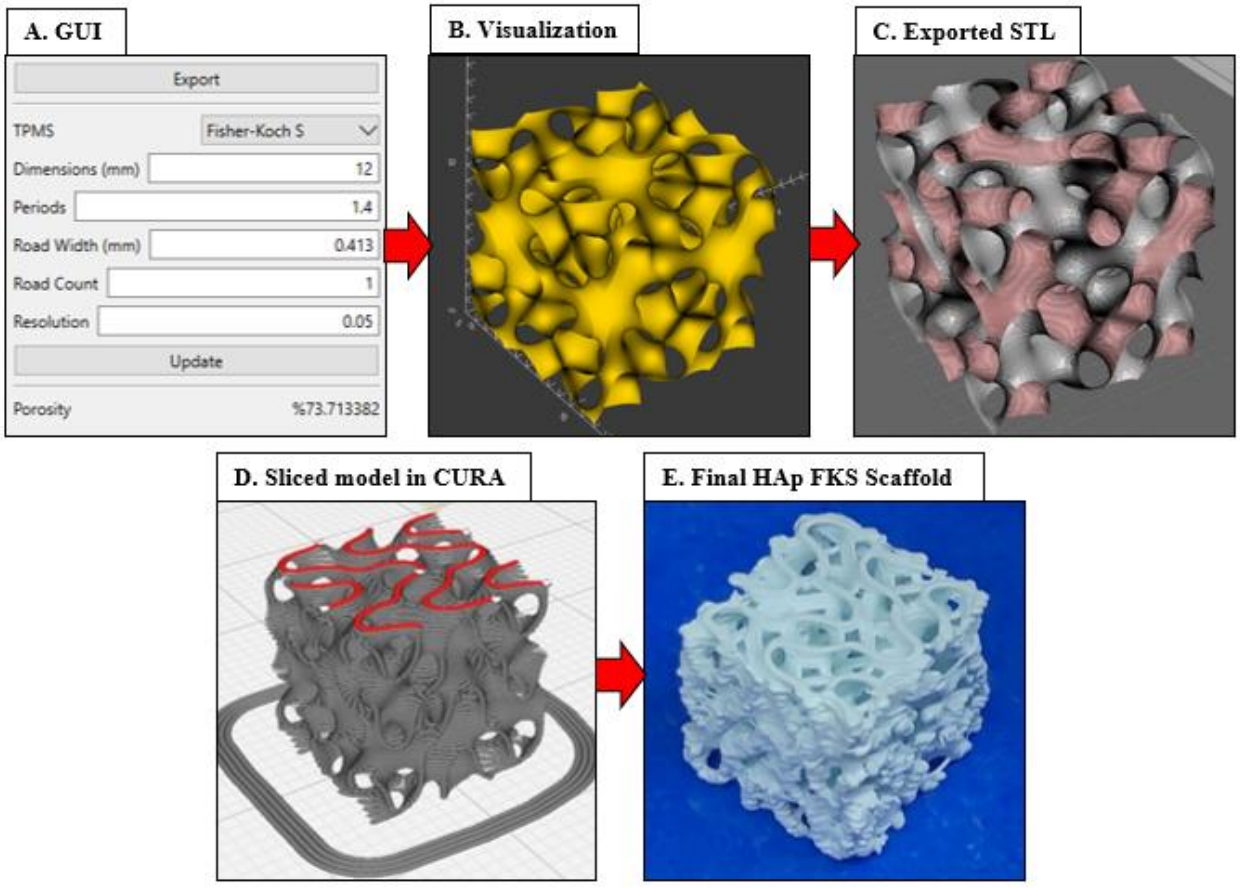

Figure 4. FKS scaffold fabrication workflow. The scaffold is designed for BTE (A,B), exported to an STL file (C), sliced in Ultimaker Cura (D), and photocast in Hap (E). Images by authors and Ultimaker Cura.

Representative printed scaffolds are shown in Figure 5. Surfaces printed uniformly and overhangs bridged without notable collapse. Extruded roads were well-formed, as defined by their consistent width, unbroken length, and smooth surface texture. Road width varied most near the ends of roads in the vertical sides (X–Z and Y–Z planes) of the scaffold, where excess slurry

extrusion, referred to as “ooze,” resulted in a melted appearance, as illustrated in the Z–Y plane of Figure 5A, B.

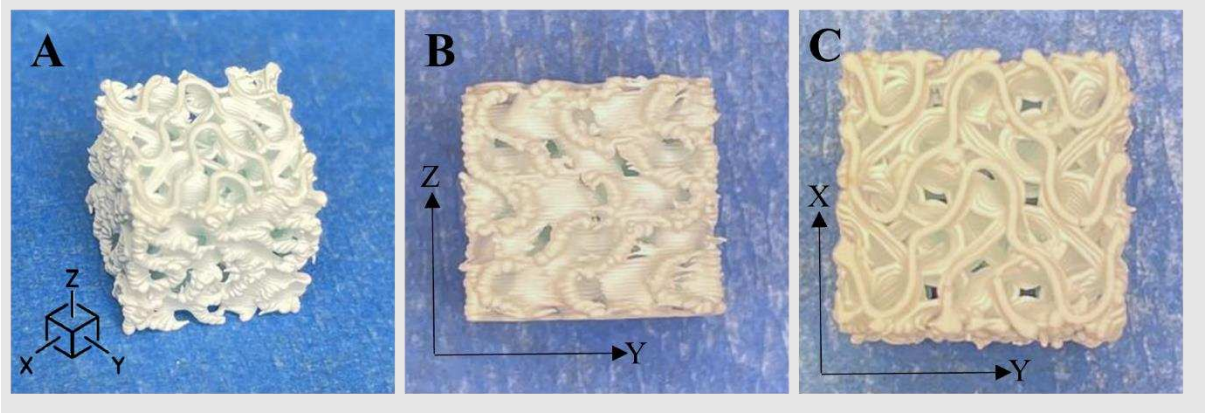

Figure 5. Representative images of HAp FKS scaffolds where the Z-axis is the build direction. From left to right: (A) isometric view, (B) side view, (C) top view.

In Figure 6A, red paths represent the sliced road extrusions, and the white regions denote extruder start/stop points in X–Z and Y–Z external faces. Figure 6B shows a heatmap produced from micro-CT which highlights areas where red regions are the thickest extrusion and green are the thinnest. Road endpoints (white regions in Figure 6A) coincide with the locations of excess extruded material in the heatmap shown in Figure 6B.

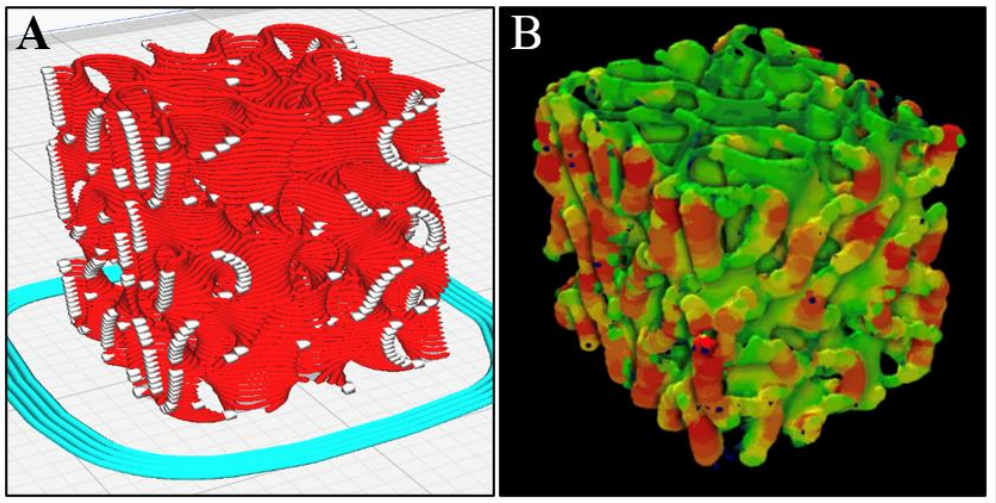

Figure 6. Toolpath start/stop points (white regions in (A)) coincide with excess extruded material shown in the micro-CT heatmap in (B), where red regions are thickest and green are thinnest.

2.3.2 Surface Morphology & Layer Cohesion

SEM evaluation revealed excellent as-sintered scaffold morphology. Inter-layer bonding appeared to be consistent, cohesive, and well-formed. Road stacking appeared to create unified walls, as shown in Figure 7, where no apparent interfacial boundary exists between roads. Layer adhesion could also be observed as a bulk quality, where the scaffolds showed sufficient durability to be handled and gripped without fracture.

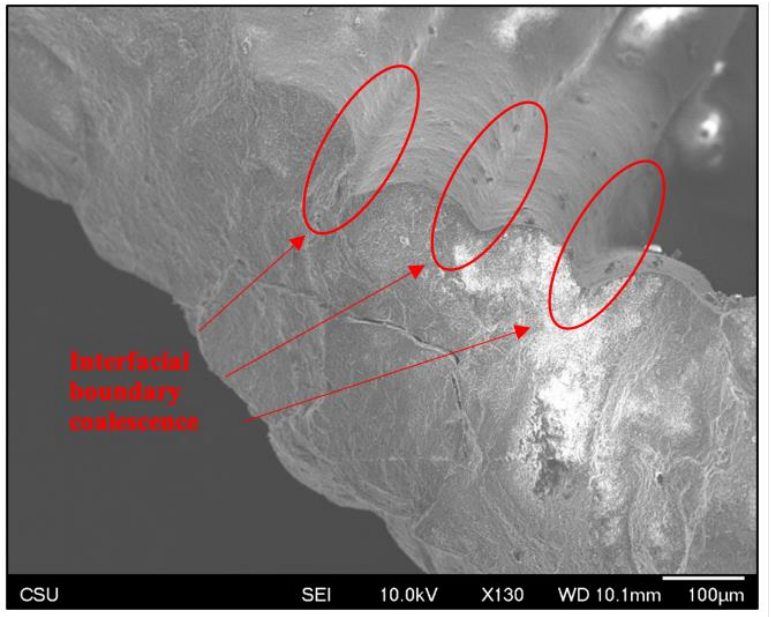

Figure 7. Representative SEM image of good layer cohesion and surface microstructure.

Roads are smooth and surfaces are consistently corrugated (Figures 7 and 8), as would be expected in material extrusion printing. Some gaps are apparent in as-sintered scaffolds (Figure 8), where a space in the as-designed surface cannot be filled with an exact number of roads at the given road diameter. In other words, the interpolated spacing cannot be filled with an integer number of roads. This is a result of the slicer calculations, not printing error.

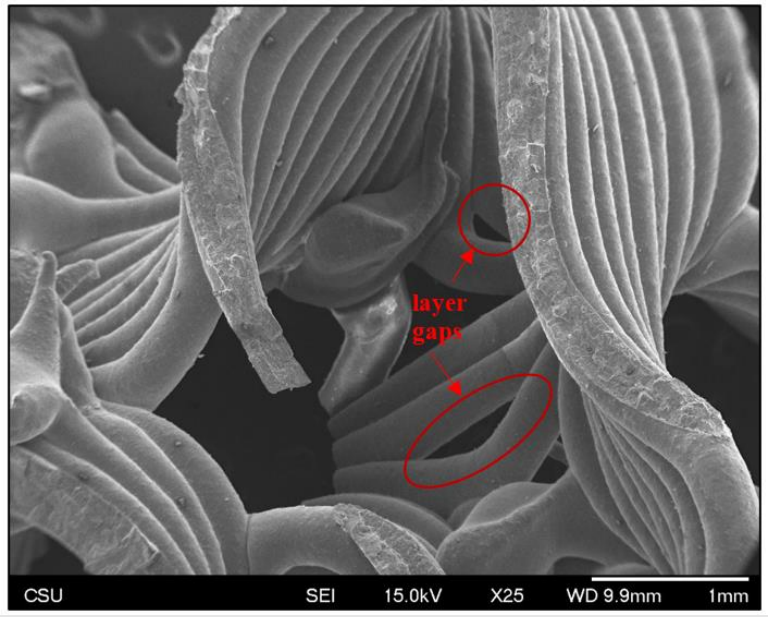

Figure 8. Representative SEM image showing surface microstructure and road alignment. Gaps between layers, as discussed above, can be seen in two highlighted areas.

2.3.3 Dimensional Accuracy

Figure 9 shows the dimensional accuracy of the printing and sintering process in the thirteen cubic test scaffolds compared to the as-designed side length. The printing process resulted in an increase in all dimensions and the sintering process caused a decrease (i.e., shrinkage) in all dimensions. The changes from as-designed to as-printed and from as-printed to as-sintered are expressed as percentages in Figure 10, along with the significance of these changes, where the null hypothesis assumes isotropic effects. No significant difference was observed between X and Y dimensions for printing and shrinkage, whereas Z was significantly different ($p < 0.001$) in all comparisons.

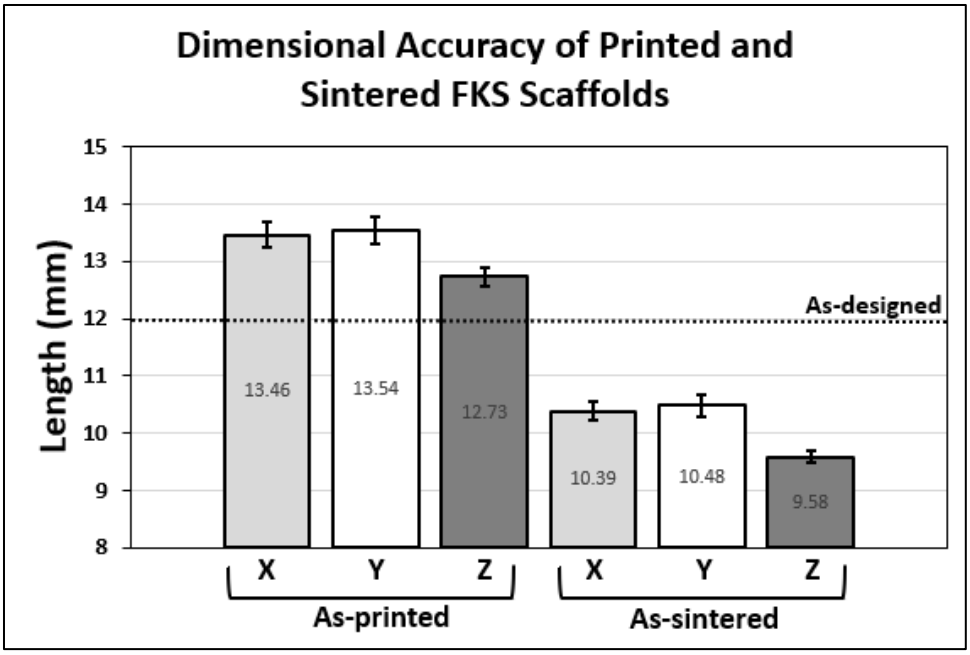

Figure 9. Comparing as-printed and as-sintered major scaffold dimensions with reference to the as-designed (CAD) scaffold side lengths.

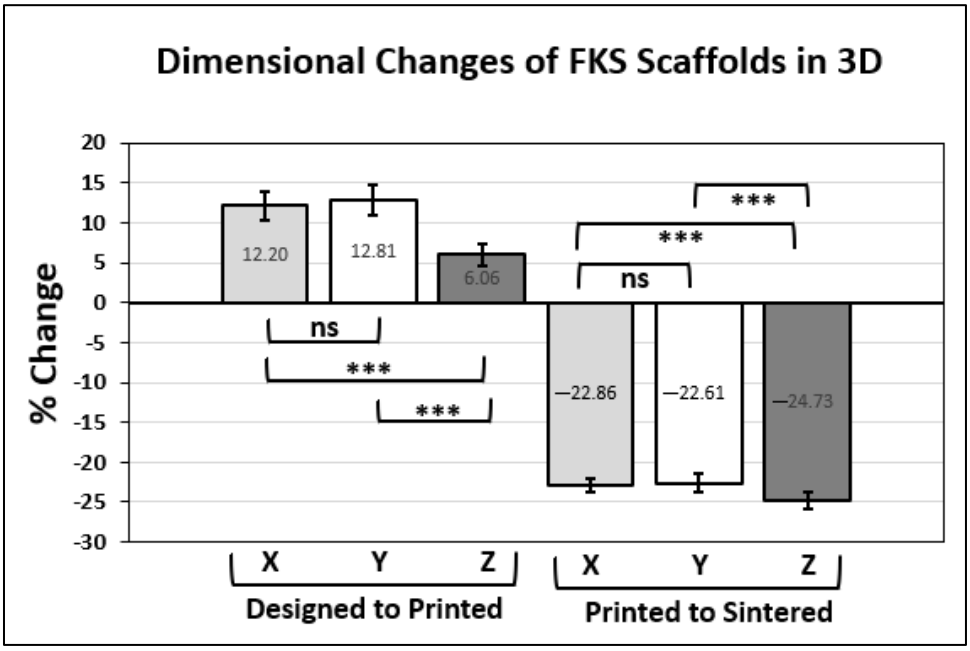

Figure 10. Percent change in scaffold side lengths between as-designed and as-printed is shown on the left. Percent shrinkage between as-printed and as-sintered is presented on the right. Significance comparisons (***, $P < 0.001$) are made between each major dimension, as denoted by brackets.

2.3.4 Scaffold Pore Size, Porosity & Wall Thickness

Micro-CT scans of three representative FKS scaffolds revealed three-dimensional characteristics relating to the pore size, porosity, and wall thickness of the finished scaffolds. The image produced by a typical scan is shown in Figure 11, and the resulting data are displayed in Table 1 below. The average as-sintered porosity of FKS scaffolds was 74.05 ± 0.38%, while the average wall thickness was 0.42 ± 0.15 mm. The pore size was evaluated as an elliptical cross section with average major and minor diameters of 2.11 ± 0.19 mm and 1.77 ± 0.14 mm, respectively.

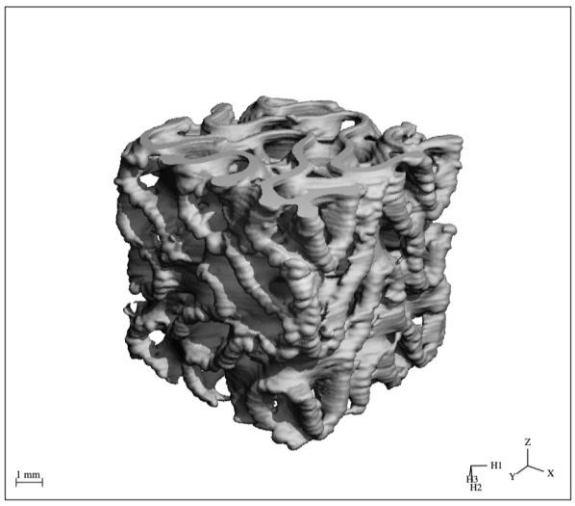

Figure 11. Representative μ-CT scan of a sintered HAp FKS scaffold.

Table 1. 3D Characteristics of micro-CT imaging for FKS cubes (N = 3).

	As-Designed (Exact)		As-Sintered (Mean ± SD)
Porosity (%)	73.713		74.05 ± 0.39
Wall Thickness (mm)	0.413		0.42 ± 0.15
Pore Diameter (mm) XY plane	2.423	Major:	2.11 ± 0.19
		Minor:	1.77 ± 0.14

2.4 Discussion

Scaffold breakage during the printing process posed a challenge while 3D printing FKS scaffolds. These events were the result of the nozzle colliding with previously extruded and cured roads. Therefore, a relatively high amount of operator monitoring was required throughout the course of printing FKS scaffolds, compared to gyroid scaffolds, for example. Oozing of slurry during interior road formation caused a higher (Z) road profile than expected by the program. These anomalies could be as large as a few millimeters in road length if they occurred. Consequently, if this anomaly was large enough, when the nozzle path returned to an anomalous section, it contacted a prior road and sometimes fractured the scaffold in that segment. This challenge was mitigated by very small, typically approximately 25 μm, manual adjustments to the Z-height to raise the nozzle during head movement. These adjustments were made at the operator's discretion and varied for each scaffold due to the small deviations in extrusion discussed above. Additionally, when small collisions occurred between the nozzle and a preceding road, slurry had to be manually cleared from the nozzle tip with tweezers to prevent additional localized fractures. These Z-height adjustments and nozzle monitoring operations were typically required a half-dozen times per build and proved effective at producing scaffolds with adequate quality for BTE, with only minor imperfections.

Variability will be addressed in future work by adjustments to slurry viscosity and management of residual back pressure to reduce excess slurry extrusion.

The aforementioned quality monitoring approach was also used when printing gyroid scaffolds [60], but intervention was more frequent when printing FKS scaffolds. One of the important differentiating characteristics of FKS topology compared to gyroid topology is that FKS has internal closed loop roads, which can be seen in Figure 12. Similar to excess slurry build-up on external start/stop locations at the ends of roads in each layer (described above), excess slurry also accumulated at the co-located start/stop points of circular roads in inner regions of the FKS cubes. Moreover, these loops are suspected to contribute to anisometric dimensional accuracy (shrinkage) of FKS scaffolds, as discussed below. In total, the number of starts/stops that take place are greater in printing FKS than gyroids and pose a challenge in viscous extrusion of ceramic FKS scaffolds.

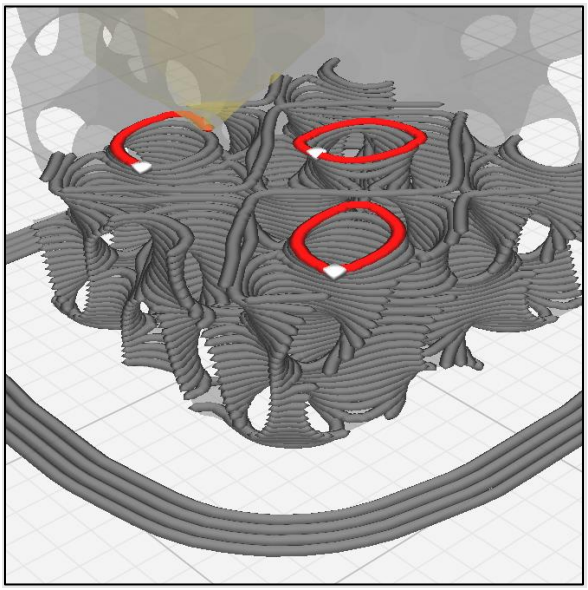

Figure 12. Circular extrusion paths with coincident start and stop points in the intermediate FKS layers were a common source of build errors. Image by Cura.

A representative heatmap image from micro-CT imagery in Figure 13 shows a slice of the internal structure of a typical scaffold, where orange regions represent relatively thicker material, much as the color maps of the external faces shown in Figure 6b. The primarily green regions visible on the top of the scaffold shown in Figure 6b and throughout Figure 13 confirmed the consistent, continuous motion of extruder. However, there were small amounts of ooze in all layers, to varying degrees, usually found localized in or adjacent to the internal closed loops. In BTE applications, imperfections in the periphery of X–Z and Y–Z planes would not impede flow through the interconnected pores of the scaffolds, rendering such defects unimportant in this context. Internal pore constriction that affects BTE scaffold function will be quantified in a subsequent section.

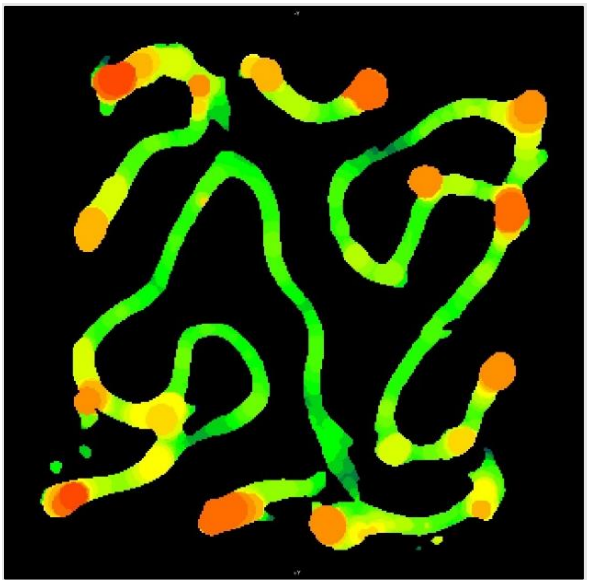

Figure 13. Representative micro-CT image of a cross-sectional slice in the X–Y plane of a ceramic FKS scaffold where red regions are thickest and green are thinnest.

The viscosity of the slurry is critical for build quality in viscous extrusion. The slurry needs some amount of shear-thinning behavior to extrude consistently for the entire build without clogging, but at the same time, it must be viscous enough to hold its shape and position as it bridges

over the open, interconnected pores of a BTE scaffold. A less-viscous slurry exhibited greater oozing and poorer bridging than a more-viscous slurry, but a highly viscous slurry ran the risk of clogging the needle, leading to a full restart of the build. To add further complexity, slurries were observed to change viscosity over time, which we postulate is caused by a combination of the evaporation of powder-suspending agents and the exposure of resin to very small and variable amounts of light during handling. To reduce these effects, slurry was used quickly after production and exposure to ambient light was minimized. As a result, the most printable slurries favored lower viscosity at a small cost to resolution. These FKS scaffolds are sufficiently good quality for future work in BTE.

The percentage change from the as-designed to as-printed dimensions showed an increase in X, Y, and Z side lengths. This general increase likely resulted from the expansion of the slurry due to the pressure gradient from the relatively high pressures inside the nozzle chamber to the lower ambient pressures of the environment. The comparison of the X and Y expansions showed no statistically significant difference and together averaged +12.51%. We do not expect variation in X–Y because the print direction varies within each layer. The percent change in the Z direction was +6.06% and was very significantly different ($p < 0.00001$) from the X–Y data. The X–Y dimension enlarged more than Z due to ooze on the vertical (external) faces of the scaffold, as described in Figure 6. Furthermore, road flattening upon deposition, which is typical of extrusion-based 3D printing [66], reduces the Z height while simultaneously expanding in the X–Y plane, both of which contribute to these dimensional variations. The standard deviation in Z dimension change was lower than that of both X and Y, leading to the conclusion that micro-adjustments in the positive Z direction that were made by operators (discussed above) did not appear to have a significant effect on scaffold height or its variability.

The shrinkage of major dimensions between as-printed and as-sintered scaffolds occurred due to the densification of ceramic particles under heat, and it was expected from our prior work that green body dimensions would decrease by approximately 21% [60]. Again, no significant difference was seen between the effects on the X and Y dimensions, which together averaged a change of −22.74%. The Z direction showed a greater reduction at −24.73%, which was significantly different from both X and Y ($p < 0.0001$). It is postulated that the Z height shrinks the most because there is more variability in as-printed layers in Z than in X or Y due to extrusion pressure and ooze effects, as discussed above. Some dimensional variation results from the shear-thinning behavior of the slurry as it is being extruded through the nozzle, which leads to variations in flow behavior. Moreover, small amounts of material are over-extruded due to residual back pressure in the print nozzle while the print head is moving between print locations. The helical extruder that drives the viscous extrusion was backed off slightly during non-printing head movements in order to mitigate this residual backpressure, but it was not completely eliminated.

For a rectilinear scaffold, pores are consistent in shape between layers and are trivial to measure. Within a TPMS scaffold, the continuous curvature in three dimensions makes the shape and area of each pore's cross section different on each slice as one traverses any axis. This makes pore size difficult to compare between topologies and to compare to other research. Pore size in the context of BTE seeks to quantify an interconnected channel that is conducive to the mass transport of nutrients to promote healthy bone cell activity and subsequent bone regeneration. In this context, pore size was measured as the diameter of the most-constricted inlet with the assumption that flow would occur in the Z direction. As-designed pores in the X–Y plane of FKS scaffolds are circular with a diameter of 2.42 mm. However, as-sintered pores were elliptical with average major and minor diameters of 2.11 ± 0.19 mm and 1.77 ± 0.14 mm, respectively. Shrinkage

of pores occurred as a result of the sintering process and should be factored into any scaffold design, as discussed above. The percent change between as-designed to as-sintered diameters was 13.08% in the major axis and 27.10% in the minor axis. This differed from the side length shrinkage in the X–Y plane of 22.74%, which is surprising considering that material ooze would have reduced pore size further. This can be explained on the basis of the relative contributions of decreased pore size and increased wall thickness (due to settling) to the overall side length dimension. Moreover, the diameters in the major axis were aligned with the road directions, which formed the pores on each layer (Figure 14), indicating that the decrease in pore size can be attributed to layer flattening and ooze when viewed in the X–Y plane. Figure 14 illustrates the anisotropic constriction of a pore compared to the road direction overlaid on the micro-CT model of a sintered scaffold.

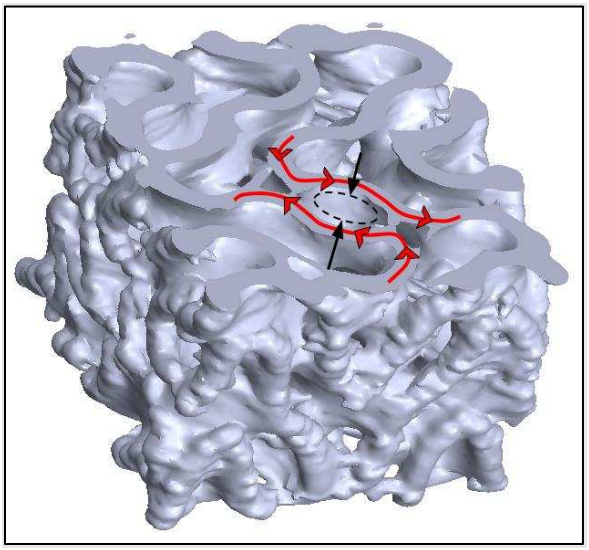

Figure 14. A section view in the X–Y plane of an as-sintered scaffold taken from micro-CT imagery. The construction of a pore denoted by the black arrows is perpendicular to the printed road direction denoted by the red arrows.

The as-sintered porosity of 74.05 ± 0.39% was within one standard deviation of the as-designed value of 73.71%. The porosity was open and interconnected, which is highly desirable

for BTE [49], [67]. This similarity results from a combination of two counter-opposing factors: the aforementioned expansion in wall thickness due to ooze, which results in decreased porosity, concurrent with the increased porosity that results from densification in sintering. The small variability in as-sintered porosity can be attributed to material ooze, which added excess material (decreasing porosity), and to minor fractures that resulted in loss of material, thereby increasing porosity. Furthermore, some porosity variation is caused by the micro-CT image processing method, which filters small variations in density differently. The average wall thickness was greater than expected and the average pore size was smaller than expected. The leads to the conclusion that as-sintered porosity would be less than as-designed porosity. The as-sintered porosity was likely inflated by the method micro-CT uses to measure it. Because a total volume cube is manually drawn in micro-CT to encompass the entire scaffold, small regions of void space are created on the perimeter of the scaffold where the greatest amounts ooze are found. This empty space would not be considered part of the enclosed void but is measured by the method, thereby increasing the measured porosity.

The as-sintered scaffolds had an average wall thickness of 0.42 mm with a standard deviation of ±0.15 mm. This wall thickness was greater than the designed value of 0.413 mm as a result of the flattening of layers and ooze that occurred during deposition, as previously described. Upon review of planar slices throughout the micro-CT images, wall thickness appeared to be bimodal, with thinner walls on the scaffold interior, and thicker walls on the exterior, agreeing with the conclusions from the color maps in Figure 6. This bimodality explains the high standard deviation of nearly ±35%, highlighting the capability of ceramic photocasting technology to produce consistent interior roads in complex topologies, which has promising implications for BTE. Future work is needed to reduce ooze at road endpoints, although it is considered less important than consistent internal morphology.

2.5 Conclusions

This study presented the development of a software algorithm for creating TPMS scaffolds suitable for 3D printing. This algorithm was then used to create scaffolds with FKS topology, which were subsequently fabricated in a ceramic commonly used in BTE. The scaffolds exhibited a porosity of 74.05%, which is considered in the ideal range of porosity for BTE [49], [67]. Idiosyncrasies between printing the more common gyroid topology and the FKS topology were presented, some of which resulted in unique challenges when printing FKS scaffolds. Most of these issues were not unique to FKS but are common in any viscous extrusion 3D printing. To the best of our knowledge, this paper presents the first 3D printing of ceramic FKS scaffolds for bone tissue engineering. The software used to design cubic scaffolds in this report is available to the open-source community [63] to enable and accelerate research on TPMS, such as FKS and gyroids, and any continuous differentiable implicit function representation, also including spheres, ellipsoids, and conic sections.

The critical advantages of 3D-printed scaffolds are their tunable properties for application-specific design, their customizable shapes for patient-specific design, and their relatively rapid manufacturing rates. Results demonstrated that ceramic scaffolds with complex topologies could be 3D printed with accuracy and quality suitable for BTE. Control of porosity, pore size, and interconnectivity are particularly important, and was demonstrated in this study. The dimensional accuracy showed error, but with further research in slurry optimization and process control, reductions in ooze and improved understanding of shrinkage could enable custom ceramic FKS scaffolds for patients. And lastly, with the methods developed in this report, the entire process can occur on low-cost 3D printers in under 24 h. Future work will also include a functional grading of TPMS scaffolds along with analysis of ceramic scaffolds in the context of BTE, including the study of mechanical properties, failure modes, permeability, and *in vitro* osteogenic response.

References

[1] B.-N. B. Nguyen, H. Ko, R. A. Moriarty, J. M. Etheridge, and J. P. Fisher, "Dynamic Bioreactor Culture of High Volume Engineered Bone Tissue," *Tissue Engineering Part A*, vol. 22, no. 3–4, pp. 263–271, Feb. 2016, doi: 10.1089/ten.tea.2015.0395.

[2] R. Burge, B. Dawson-Hughes, D. H. Solomon, J. B. Wong, A. King, and A. Tosteson, "Incidence and economic burden of osteoporosis-related fractures in the United States, 2005-2025," *J Bone Miner Res*, vol. 22, no. 3, pp. 465–475, Mar. 2007, doi: 10.1359/jbmr.061113.

[3] M. Bonafede, D. Espindle, and A. G. Bower, "The direct and indirect costs of long bone fractures in a working age US population," *Journal of Medical Economics*, vol. 16, no. 1, pp. 169–178, Feb. 2013, doi: 10.3111/13696998.2012.737391.

[4] S. Amin, S. J. Achenbach, E. J. Atkinson, S. Khosla, and L. J. Melton, "Trends in Fracture Incidence: A Population-Based Study Over 20 Years," *J Bone Miner Res*, vol. 29, no. 3, pp. 581–589, Mar. 2014, doi: 10.1002/jbmr.2072.

[5] M. Wagels, D. Rowe, S. Senewiratne, T. Read, and D. R. Theile, "Soft tissue reconstruction after compound tibial fracture: 235 cases over 12 years," *Journal of Plastic, Reconstructive & Aesthetic Surgery*, vol. 68, no. 9, pp. 1276–1285, Sep. 2015, doi: 10.1016/j.bjps.2015.05.017.

[6] D. Chang and K. Weber, "Use of a vascularized fibula bone flap and intercalary allograft for diaphyseal reconstruction after resection of primary extremity bone sarcomas," *Plast Reconstr Surg*, vol. 116, pp. 1918–1925, 2005.

[7] L. Vidal, C. Kampleitner, M. Á. Brennan, A. Hoornaert, and P. Layrolle, "Reconstruction of Large Skeletal Defects: Current Clinical Therapeutic Strategies and Future Directions Using 3D Printing," *Front. Bioeng. Biotechnol.*, vol. 8, p. 61, Feb. 2020, doi: 10.3389/fbioe.2020.00061.

[8] A. Roffi, G. S. Krishnakumar, N. Gostynska, E. Kon, C. Candrian, and G. Filardo, "The Role of Three-Dimensional Scaffolds in Treating Long Bone Defects: Evidence from Preclinical and Clinical Literature-A Systematic Review," *Biomed Res Int*, vol. 2017, p. 8074178, 2017, doi: 10.1155/2017/8074178.

[9] S. Bose, D. Ke, H. Sahasrabudhe, and A. Bandyopadhyay, "Additive manufacturing of biomaterials," *Progress in Materials Science*, vol. 93, pp. 45–111, Apr. 2018, doi: 10.1016/j.pmatsci.2017.08.003.

[10] B. C. Gross, J. L. Erkal, S. Y. Lockwood, C. Chen, and D. M. Spence, "Evaluation of 3D Printing and Its Potential Impact on Biotechnology and the Chemical Sciences," *Anal. Chem.*, vol. 86, no. 7, pp. 3240–3253, Apr. 2014, doi: 10.1021/ac403397r.

[11] S. Tarafder, V. K. Balla, N. M. Davies, A. Bandyopadhyay, and S. Bose, "Microwave-sintered 3D printed tricalcium phosphate scaffolds for bone tissue engineering," *Journal of Tissue Engineering and Regenerative Medicine*, vol. 7, no. 8, pp. 631–641, 2013, doi: 10.1002/term.555.

[12] J. L. Vondran, W. Sun, and C. L. Schauer, "Crosslinked, electrospun chitosan–poly (ethylene oxide) nanofiber mats," *Journal of Applied Polymer Science*, vol. 109, pp. 968–975, 2008.

[13] S. J. Hollister, "Porous scaffold design for tissue engineering," *Nature Materials*, vol. 4, no. 7, pp. 518–524, Jul. 2005, doi: 10.1038/nmat1421.

[14] S. Bose, S. Vahabzadeh, and A. Bandyopadhyay, "Bone tissue engineering using 3D printing," *Materials Today*, vol. 16, no. 12, pp. 496–504, Dec. 2013, doi: 10.1016/j.mattod.2013.11.017.

[15] K. Lin, R. Sheikh, S. Romanazzo, and I. Roohani, "3D Printing of Bioceramic Scaffolds—Barriers to the Clinical Translation: From Promise to Reality, and Future Perspectives," *Materials (Basel)*, vol. 12, no. 17, p. 2660, Aug. 2019, doi: 10.3390/ma12172660.

[16] M. J. Zafar, D. Zhu, and Z. Zhang, "3D Printing of Bioceramics for Bone Tissue Engineering.," *Materials (Basel)*, vol. 12, no. 20, p. E3361, Oct. 2019, doi: 10.3390/ma12203361.

[17] M. Ly, S. Spinelli, S. Hays, and D. Zhu, "3D Printing of Ceramic Biomaterials," *Engineered Regeneration*, vol. 3, no. 1, pp. 41–52, Mar. 2022, doi: 10.1016/j.engreg.2022.01.006.

[18] K. A. Athanasiou, C.-F. Zhu, D. R. Lanctot, C. M. Agrawal, and X. Wang, "Fundamentals of Biomechanics in Tissue Engineering of Bone," *Tissue Engineering*, vol. 6, no. 4, pp. 361–381, Aug. 2000, doi: 10.1089/107632700418083.

[19] V. Karageorgiou and D. Kaplan, "Porosity of 3D biomaterial scaffolds and osteogenesis," *Biomaterials*, vol. 26, no. 27, pp. 5474–5491, Sep. 2005, doi: 10.1016/j.biomaterials.2005.02.002.

[20] Karande, Ong and Agrawal, "Diffusion in Musculoskeletal Tissue Engineering Scaffolds-Design Issues Related to Porosity, Permeability, Architecture, and Nutrient Mixing," *Annals of Biomedical Engineering*, vol. 32, no. 12, pp. 1728–1743, Dec. 2004.

[21] M. R. Dias, P. R. Fernandes, J. M. Guedes, and S. J. Hollister, "Permeability analysis of scaffolds for bone tissue engineering," *Journal of Biomechanics*, vol. 45, no. 6, pp. 938–944, Apr. 2012, doi: 10.1016/j.jbiomech.2012.01.019.

[22] S. Tarafder, W. S. Dernell, A. Bandyopadhyay, and S. Bose, "SrO- and MgO-doped microwave sintered 3D printed tricalcium phosphate scaffolds: Mechanical properties and *in vivo* osteogenesis in a rabbit model," *J. Biomed. Mater. Res.*, vol. 103, no. 3, pp. 679–690, Apr. 2015, doi: 10.1002/jbm.b.33239.

[23] S. Bose, J. Darsell, M. Kintner, H. Hosick, and A. Bandyopadhyay, "Pore size and pore volume effects on alumina and TCP ceramic scaffolds," *Materials Science and Engineering: C*, vol. 23, no. 4, pp. 479–486, Jun. 2003, doi: 10.1016/S0928-4931(02)00129-7.

[24] S. Wu, X. Liu, K. W. K. Yeung, C. Liu, and X. Yang, "Biomimetic porous scaffolds for bone tissue engineering," *Materials Science and Engineering: R: Reports*, vol. 80, pp. 1–36, Jun. 2014, doi: 10.1016/j.mser.2014.04.001.

[25] S. Sturm, S. Zhou, Y.-W. Mai, and Q. Li, "On stiffness of scaffolds for bone tissue engineering—a numerical study," *Journal of Biomechanics*, vol. 43, no. 9, pp. 1738–1744, Jun. 2010, doi: 10.1016/j.jbiomech.2010.02.020.

[26] R. F. Pereira and P. J. Bártolo, "3D Photo-Fabrication for Tissue Engineering and Drug Delivery," *Engineering*, vol. 1, no. 1, pp. 090–112, Mar. 2015, doi: 10.15302/J-ENG-2015015.

[27] S. Choi, Y.-I. Oh, K.-H. Park, J.-S. Lee, J.-H. Shim, and B.-J. Kang, "New clinical application of three-dimensional-printed polycaprolactone/β-tricalcium phosphate scaffold as an alternative to allograft bone for limb-sparing surgery in a dog with distal radial osteosarcoma," *The Journal of Veterinary Medical Science*, vol. 81, no. 3, pp. 434–439, 2019, doi: 10.1292/jvms.18-0158.

[28] J. Franch, A. Barba, K. Rappe, Y. Maazouz, and M. Ginebra, "Use of three-dimensionally printed β-tricalcium phosphate synthetic bone graft combined with recombinant human bone morphogenic protein-2 to treat a severe radial atrophic nonunion in a Yorkshire terrier," *Veterinary Surgery*, p. vsu.13476, Jul. 2020, doi: 10.1111/vsu.13476.

[29] J. Henkel *et al.*, "Scaffold-guided bone regeneration in large volume tibial segmental defects," *Bone*, vol. 153, p. 116163, Dec. 2021, doi: 10.1016/j.bone.2021.116163.

[30] Y. P. Yang *et al.*, "Osteoinductive 3D printed scaffold healed 5 cm segmental bone defects in the ovine metatarsus," *Sci Rep*, vol. 11, no. 1, p. 6704, Dec. 2021, doi: 10.1038/s41598-021-86210-5.

[31] L. Yuan, S. Ding, and C. Wen, "Additive manufacturing technology for porous metal implant applications and triple minimal surface structures: A review," *Bioactive Materials*, vol. 4, no. 1, pp. 56–70, Mar. 2019, doi: 10.1016/j.bioactmat.2018.12.003.

[32] D. W. Abueidda, M. Elhebeary, C.-S. (Andrew) Shiang, S. Pang, R. K. Abu Al-Rub, and I. M. Jasiuk, "Mechanical properties of 3D printed polymeric Gyroid cellular structures: Experimental and finite element study," *Materials & Design*, vol. 165, p. 107597, Mar. 2019, doi: 10.1016/j.matdes.2019.107597.

[33] L. Germain, C. A. Fuentes, A. W. van Vuure, A. des Rieux, and C. Dupont-Gillain, "3D-printed biodegradable gyroid scaffolds for tissue engineering applications," *Materials and Design*, p. 10, 2018, doi: https://doi.org/10.1016/j.matdes.2018.04.037.

[34] K. C. R. Kolan, A. Thomas, M. C. Leu, and G. Hilmas, "In vitro assessment of laser sintered bioactive glass scaffolds with different pore geometries," *Rapid Prototyping Journal*, vol. 21, no. 2, pp. 152–158, Mar. 2015, doi: 10.1108/RPJ-12-2014-0175.

[35] S. C. Kapfer, S. T. Hyde, K. Mecke, C. H. Arns, and G. E. Schröder-Turk, "Minimal surface scaffold designs for tissue engineering," *Biomaterials*, vol. 32, no. 29, pp. 6875–6882, Oct. 2011, doi: 10.1016/j.biomaterials.2011.06.012.

[36] M. Alizadeh-Osgouei, Y. Li, A. Vahid, A. Ataee, and C. Wen, "High strength porous PLA gyroid scaffolds manufactured via fused deposition modeling for tissue-engineering applications," *Smart Materials in Medicine*, vol. 2, pp. 15–25, Jan. 2021, doi: 10.1016/j.smaim.2020.10.003.

[37] A. Bigham, F. Foroughi, E. Rezvani Ghomi, M. Rafienia, R. E. Neisiany, and S. Ramakrishna, "The journey of multifunctional bone scaffolds fabricated from traditional

toward modern techniques," *Bio-des. Manuf.*, vol. 3, no. 4, pp. 281–306, Dec. 2020, doi: 10.1007/s42242-020-00094-4.

[38] H. Jia *et al.*, "An experimental and numerical investigation of compressive response of designed Schwarz Primitive triply periodic minimal surface with non-uniform shell thickness," *Extreme Mechanics Letters*, vol. 37, p. 100671, May 2020, doi: 10.1016/j.eml.2020.100671.

[39] Y. Lu, L. Cheng, Z. Yang, J. Li, and H. Zhu, "Relationship between the morphological, mechanical and permeability properties of porous bone scaffolds and the underlying microstructure," *PLoS ONE*, vol. 15, no. 9, p. e0238471, Sep. 2020, doi: 10.1371/journal.pone.0238471.

[40] S. Ma, Q. Tang, Q. Feng, J. Song, X. Han, and F. Guo, "Mechanical behaviours and mass transport properties of bone-mimicking scaffolds consisted of gyroid structures manufactured using selective laser melting," *Journal of the Mechanical Behavior of Biomedical Materials*, vol. 93, pp. 158–169, May 2019, doi: 10.1016/j.jmbbm.2019.01.023.

[41] I. Maskery *et al.*, "Insights into the mechanical properties of several triply periodic minimal surface lattice structures made by polymer additive manufacturing," *Polymer*, vol. 152, pp. 62–71, Sep. 2018, doi: 10.1016/j.polymer.2017.11.049.

[42] J. Wieding, A. Wolf, and R. Bader, "Numerical optimization of open-porous bone scaffold structures to match the elastic properties of human cortical bone," *Journal of the Mechanical Behavior of Biomedical Materials*, vol. 37, pp. 56–68, Sep. 2014, doi: 10.1016/j.jmbbm.2014.05.002.

[43] J. Feng, J. Fu, X. Yao, and Y. He, "Triply periodic minimal surface (TPMS) porous structures: from multi-scale design, precise additive manufacturing to multidisciplinary applications," *Int. J. Extrem. Manuf.*, vol. 4, no. 2, p. 022001, Mar. 2022, doi: 10.1088/2631-7990/ac5be6.

[44] F. P. W. Melchels, M. A. N. Domingos, T. J. Klein, J. Malda, P. J. Bartolo, and D. W. Hutmacher, "Additive manufacturing of tissues and organs," *Progress in Polymer Science*, vol. 37, no. 8, pp. 1079–1104, Aug. 2012, doi: 10.1016/j.progpolymsci.2011.11.007.

[45] A. M. Abou-Ali, O. Al-Ketan, R. Rowshan, and R. Abu Al-Rub, "Mechanical Response of 3D Printed Bending-Dominated Ligament-Based Triply Periodic Cellular Polymeric Solids," *J. of Materi Eng and Perform*, vol. 28, no. 4, pp. 2316–2326, Apr. 2019, doi: 10.1007/s11665-019-03982-8.

[46] I. Maskery, N. T. Aboulkhair, A. O. Aremu, C. J. Tuck, and I. A. Ashcroft, "Compressive failure modes and energy absorption in additively manufactured double gyroid lattices," *Additive Manufacturing*, vol. 16, pp. 24–29, Aug. 2017, doi: 10.1016/j.addma.2017.04.003.

[47] I. Maskery *et al.*, "Insights into the mechanical properties of several triply periodic minimal surface lattice structures made by polymer additive manufacturing," *Polymer*, vol. 152, pp. 62–71, Sep. 2018, doi: 10.1016/j.polymer.2017.11.049.

[48] A. P. G. Castro, J. Santos, T. Pires, and P. R. Fernandes, "Micromechanical Behavior of TPMS Scaffolds for Bone Tissue Engineering," *Macromol. Mater. Eng.*, vol. 305, no. 12, p. 2000487, Dec. 2020, doi: 10.1002/mame.202000487.

[49] F. P. W. Melchels, A. M. C. Barradas, C. A. van Blitterswijk, J. de Boer, J. Feijen, and D. W. Grijpma, "Effects of the architecture of tissue engineering scaffolds on cell seeding and culturing," *Acta Biomaterialia*, vol. 6, no. 11, pp. 4208–4217, Nov. 2010, doi: 10.1016/j.actbio.2010.06.012.

[50] J. Santos, T. Pires, B. P. Gouveia, A. P. G. Castro, and P. R. Fernandes, "On the permeability of TPMS scaffolds," *Journal of the Mechanical Behavior of Biomedical Materials*, vol. 110, p. 103932, Oct. 2020, doi: 10.1016/j.jmbbm.2020.103932.

[51] A. Diez-Escudero, H. Harlin, P. Isaksson, and C. Persson, "Porous polylactic acid scaffolds for bone regeneration: A study of additively manufactured triply periodic minimal surfaces and their osteogenic potential," *J Tissue Eng*, vol. 11, p. 204173142095654, Jan. 2020, doi: 10.1177/2041731420956541.

[52] T. Maconachie *et al.*, "The compressive behaviour of ABS gyroid lattice structures manufactured by fused deposition modelling," *Int J Adv Manuf Technol*, vol. 107, no. 11–12, pp. 4449–4467, Apr. 2020, doi: 10.1007/s00170-020-05239-4.

[53] A. Karakoc, "RegionTPMS — Region based triply periodic minimal surfaces (TPMS) for 3-D printed multiphase bone scaffolds with exact porosity values," *SoftwareX*, vol. 16, p. 100835, Dec. 2021, doi: 10.1016/j.softx.2021.100835.

[54] S. Bose, A. Banerjee, S. Dasgupta, and A. Bandyopadhyay, "Synthesis, Processing, Mechanical, and Biological Property Characterization of Hydroxyapatite Whisker-Reinforced Hydroxyapatite Composites," *Journal of the American Ceramic Society*, vol. 92, no. 2, pp. 323–330, 2009, doi: 10.1111/j.1551-2916.2008.02881.x.

[55] S. Restrepo, S. Ocampo, J. A. Ramírez, C. Paucar, and C. García, "Mechanical properties of ceramic structures based on Triply Periodic Minimal Surface (TPMS) processed by 3D printing," *J. Phys.: Conf. Ser.*, vol. 935, no. 1, p. 012036, Dec. 2017, doi: 10.1088/1742-6596/935/1/012036.

[56] M. Faes, H. Valkenaers, F. Vogeler, J. Vleugels, and E. Ferraris, "Extrusion-based 3D Printing of Ceramic Components," *Procedia CIRP*, vol. 28, pp. 76–81, 2015, doi: 10.1016/j.procir.2015.04.028.

[57] M. Asif *et al.*, "A new photopolymer extrusion 5-axis 3D printer," *Additive Manufacturing*, vol. 23, pp. 355–361, Oct. 2018, doi: 10.1016/j.addma.2018.08.026.

[58] R. D. Farahani, L. L. Lebel, and D. Therriault, "Processing parameters investigation for the fabrication of self-supported and freeform polymeric microstructures using ultraviolet-assisted three-dimensional printing," *J. Micromech. Microeng.*, vol. 24, no. 5, p. 055020, 2014, doi: 10.1088/0960-1317/24/5/055020.

[59] Lopez Ambrosio, Katherine V., "HYDROXYAPATITE STRUCTURES CREATED BY ADDITIVE MANUFACTURING WITH EXTRUDED PHOTOPOLYMER," Master's Thesis, Colorado State University, Ft. Collins, CO, 2019.

[60] N. Isaacson *et al.*, “Compressive properties and failure behavior of photocast hydroxyapatite gyroid scaffolds vary with porosity,” *J Biomater Appl*, p. 088532822110739, Mar. 2022, doi: 10.1177/08853282211073904.

[61] Y. Lu, W. Zhao, Z. Cui, H. Zhu, and C. Wu, “The anisotropic elastic behavior of the widely-used triply-periodic minimal surface based scaffolds,” *Journal of the Mechanical Behavior of Biomedical Materials*, vol. 99, pp. 56–65, Nov. 2019, doi: 10.1016/j.jmbbm.2019.07.012.

[62] M. Geier and H. Alihussein, “Computation of Implicit Representation of Volumetric Shells with Predefined Thickness,” *Algorithms*, vol. 14, no. 4, p. 125, Apr. 2021, doi: 10.3390/a14040125.

[63] E. Gunn, “Non-manifold meshes for Gyroid and Fisher-Koch S triply periodic minimal surfaces.,” Available online: https://github.com/IkonOne/tpmsModeller. Accessed: Jan. 02, 2023. [Online]. Available: https://github.com/IkonOne/tpmsModeller

[64] M. et. al. Musy, “Vedo, a python module for scientific analysis and visualization of 3D objects and point clouds,” Available online: https://zenodo.org/record/7222019#.Y1GySnbMLD4. Accessed: Oct. 18, 2022. [Online]. Available: https://zenodo.org/record/7222019#.Y1GySnbMLD4

[65] M. Abràmoff, “Image Processing with ImageJ,” *Biophotonics International*, vol. 11, no. 7, pp. 36–42, Jul. 2004.

[66] B. Turner, R. Strong, and S. A. Gold, “A review of melt extrusion additive manufacturing processes: I. Process design and modeling,” *Rapid Prototyping Journal*, vol. 20, no. 3, pp. 192–204, Apr. 2014, doi: 10.1108/RPJ-01-2013-0012.

[67] H. Montazerian, E. Davoodi, M. Asadi-Eydivand, J. Kadkhodapour, and M. Solati-Hashjin, “Porous scaffold internal architecture design based on minimal surfaces: A compromise between permeability and elastic properties,” *Materials & Design*, vol. 126, pp. 98–114, Jul. 2017, doi: 10.1016/j.matdes.2017.04.009.

CHAPTER 2: COMPARING FISHER-KOCH-S AND GYROID HYDROXYAPATITE SCAFFOLDS FOR TREATING LARGE BONE DEFECTS

3.1 Introduction

Highly porous tissue engineered scaffolds are widely used in bone regeneration [1-3] to mitigate well-publicized limitations of bone grafting methods, particularly in large bone defects, including recurring failures with non-union rates as high as 21% [4] and complication rates of 50% due to delayed or non-union, 30% from allograft fracture, and 15% from infection [5]. Synthetic bone tissue engineering (BTE) scaffolds attempt to accelerate the body's natural healing process. To accomplish this, BTE scaffolds must be designed to accommodate several interrelated factors including biocompatibility, structural durability and permeability while providing a favorable environment for bone healing[6-8]. Scaffolds lack the vasculature of autologous bone, emphasizing the importance of high levels of permeability [9], which considers porosity, tortuosity, pore size, shape, distribution, and interconnectivity [10-11], which are key factors contributing to new bone development, particularly in large defects [7]. Highly interconnected, high porosity structures, within a range of 50–90% depending on the anatomical location [12], are required to enable adequate mass transport of nutrients, gases and waste products during rapid bone development [9,13]. This exchange supports greater cell migration and proliferation through the three-dimensional scaffold, while playing a crucial role in angiogenesis [9,14].

Calcium phosphate-based materials, such as hydroxyapatite (HAp) and tricalcium phosphate (TCP), are popular for BTE due to their biocompatibility, high levels of bioactivity (osteoconductivity, osteoinductivity and osteointegration), similarities to human bone composition, non-immunogenicity and tunable degradation rates [15-17]. However, these apatite

scaffolds exhibit relatively low toughness due to their brittleness [18], limiting their functional usefulness in load-bearing cases, especially as high porosity structures.

The structural integrity of BTE scaffolds can be enhanced with innovative topologies like triply periodic minimal surfaces (TPMS)[19-22]. TPMS are biomimetic structures with properties that make them well-suited for bone development. These surfaces have properties that closely mimic trabecular bone structure[23]. Furthermore, they exhibit relatively high mechanical energy absorption and robustness[19, 21, 24], an interconnected internal porous structure, and a high surface area to volume ratio for an optimal cell attachment environment[25]. Additionally, structural parameters can be adjusted to achieve specific porosities, pore sizes and shapes, permeability, and tortuosity for different applications in BTE [26-28]. TPMS have natural analogs in crustacean skeletons, insect shells and butterfly wing scales [29-31] and are particularly well suited for bone healing because they provide an interconnected pore structure that is believed to facilitate cell migration along with relatively high structural stiffness[22].

3D printing enables high-precision fabrication of complex bone regeneration scaffolds with controllable physical properties like porosity and mechanical strength that make it possible to mimic the biomechanical properties of natural bone [32-33]. TPMS have been 3D printed in nearly every major 3D printing process. Material extrusion with a thermal build process (a.k.a. “FDM”) is most often used due to its low cost and high flexibility[20, 24, 34]. Robocasting is also very popular for biomimetic, ceramic scaffolds due to its very low cost and non-thermal processing method [35-39]. Powder bed fusion has been used to print numerous types of TPMS scaffolds[40-42], including Gyroids, in metals like titanium [33]. Binder jetting has been used to print numerous types of apatite scaffolds[43-46]. TPMS scaffolds were also printed using vat photopolymerization[47-49] and in hydroxyapatite- and TCP-photopolymeric slurry using digital

light processing[50-51]. Recent excellent reviews discuss the advantages and disadvantages of various 3D printing processes in a wide array of materials, topologies and applications [19, 52-54].

Among the many TPMS topologies, Gyroid and Fischer-Koch S (FKS) are particularly well suited for bone regeneration scaffolds [22,55]. Computational simulations have led to hypotheses that some topologies may be better suited than others in particular applications. For example, finite-element analysis of different TPMS topologies[22] suggest that FKS topology may be better suited to remediate a cortical diaphyseal bone defect because its high strength, low permeability, and isotropic behavior[56] better mimics dense cortical bone than other TPMS, such as Gyroids. It was similarly proposed that Gyroid scaffolds might be better suited to procedures where high anisotropy and permeability are preferable to better match the properties of cancellous bone. Gyroid TPMS have been widely studied in many forms[21, 35, 52, 54]. FKS, on the other hand, is relatively unexplored beyond computer simulations. Tools for creating G-code for printing FKS and other non-Gyroid TPMS are emerging[38], but most are proprietary software that is bundled with expensive 3D printers. To the best of our knowledge, no one has directly evaluated the properties of highly porous ceramic FKS scaffolds. In this paper, we design and 3D print ceramic FKS scaffolds for enhance bone regeneration in large defects and compare its properties to an equivalent gyroid scaffold in the context of BTE.

3.2 Materials and Methods

3.2.1 Fabrication of Ceramic Scaffolds

A photopolymeric resin containing 41 vol% HAp (89nm, Macron Fine Chemicals, Avantor, Radnor, PA, USA) was created for viscous extrusion using a previously described method[57]. Briefly, ethylene glycol dimethacrylate (EGDMA, Scientific Polymer Products, Inc., Ontario, NY, USA) was mixed with a photoinitiator (Diphenyl (2,4,6, trimethyl benzoyl) phosphine oxide, TCI

America, Portland, OR, USA), a polyanionic dispersant (Solplus D540, Lubrizol Advanced Materials Inc., Wickliffe, OH, USA), and agate milling media in a planetary ball mill (Across International, Davie, FL, USA) until a homogenous slurry resulted. Scaffolds were 3D printed on a Hyrel Engine SR 3D printer (Hyrel 3D, Norcross GA, USA) using a viscous extrusion process with simultaneous layer-wise photocuring, as previously described[38], [58]. The slurry was dispensed by a stainless-steel print head with a 0.413 mm Luer tip which was cured by an array of LED lights (405nm wavelength) at an exposure of 0.91 mW/cm^2. Scaffolds were removed from the build plate and sintered in a muffle furnace (Barnstead/Thermolyne 47900, Ramsey, MN, USA) at 1200°C for 3 hours. These finished scaffolds are referred to herein as the "as-sintered" state.

3.2.2 Scaffold Design

3D-printable Gyroid and FKS scaffold models were developed using a previously described method[38]. The trigonometric approximations for FKS and Gyroid topologies, shown in equations 7 and 8 respectively, were used to generate a 3D non-manifold mesh using a custom open-source algorithm. Then, the surfaces were exported to Ultimaker Cura slicing software (Ultimaker B.V., Utrecht, Netherlands) to create continuous layer-wise toolpaths. Twelve millimeter cubic scaffolds were generated to target final porosities of approximately 70%. A single road width of 0.413 mm, equal to the nozzle diameter, was used in the design which equates to the wall thickness. These properties are herein referred to as the "as-designed" characteristics. This process resulted in 3D-printable G-code for fabrication.

$$fks(x,y,z) = \cos(2x)\sin(y)\cos(z) + \cos(2y)\sin(z)\cos(x) + \cos(2z)\sin(x)\cos(y) = 0 \quad (7)$$

$$gyroid(x,y,z) = \sin(y)\cos(x) + \sin(z)\cos(y) + \sin(x)\cos(z) = 0 \quad (8)$$

3.2.3 Structure and Surface Characterization

Micro-computed tomography (micro-CT) measured the porosity, wall thickness, material spacing, and surface area of as-sintered FKS and Gyroid topologies. Images were taken on a Scanco 80 (Scanco Medical AG, Bruttisellen, Switzerland) and evaluated using Scanco software. The software measured the total volume (TV) of the region of interest which was fit to the scaffold perimeter across various slices, and then calculated the bone volume (BV) and bone surface (BS) of scaffold material in the space that had a density of 903 mg HAp/cm^3 or greater. Trabecular thickness (Tb.Th) and trabecular spacing (Tb.Sp) within the scaffolds were calculated by software that is intended for analyzing bone. In the context of our study, Tb.Th refers to average wall thickness, and Tb.Sp represents the average spacing of the walls, which can be compared to average pore size. Relative porosity (φ) was determined using TV and BV as shown in equation 9.

$$\varphi = (1 - \frac{BV}{TV}) * 100\% \quad (9)$$

Surface texture, micro-porosity, and fracture properties were evaluated on a field emission scanning electron microscope (SEM) (JOEL JSM 6500F, Peabody, MA, USA). Internal morphology was imaged from broken sections of scaffolds that were randomly selected after compression testing. Fragments were placed on the loading platform, coated with 10nm of gold, and imaged at 10-15 kV. Fracture behavior was identified through visual examination of cracks and failure points in reference to the loading direction as indicated by the road orientation.

3.2.3 Mechanical Testing

Mechanical properties of scaffolds were studied through compression tests. FKS and Gyroid cubic scaffolds were each compressed in two orientations to create four sample groups with fifteen samples per group. “Normal” referred to compression in the build direction (Z-axis), whereas “transverse” referred to compression orthogonal to the build direction (in the X-Y plane). Scaffold faces were smoothed with 1200 grit sandpaper to remove protrusions which improved flush contact

with the platens. Compressive stress-strain curves were obtained for each sample using a H1K-S UTM Benchtop Tester (Tinius Olsen, Horsham, PA, USA) equipped with a 1kN load cell. Samples were placed on an aluminum crosshead and preloaded to 5N before loading in normal and transverse directions at 0.1mm/min crosshead speed until the applied load decreased to 25% of the peak load. Compressive testing data was imported to MATLAB (MathWorks, Inc. MATLAB R2023a) for analysis and plotting.

3.2.4 Permeability Evaluation

Permeability was assessed by correlating the fluid velocity through a cubic scaffold to a pressure gradient. If the Reynold's number (Re) of the system is less than 1, then a Darcian flow regime[59] is valid which allows for calculation of the permeability coefficient, k , according to equations 10 and 11:

$$Re = \frac{\rho v D}{\mu} < 1 \tag{10}$$

$$k = \frac{v \mu L}{\Delta P A} \tag{11}$$

where ρ is the fluid density, v is the fluid velocity, D is the mean scaffold wall spacing, μ is the dynamic viscosity, L is the scaffold length, ΔP is the pressure drop, and A is the cross-sectional scaffold area. Using an adaptation of the experimental setup from Santos et. al.[59], a horizontal apparatus was developed wherein a hydraulic pressure gradient was induced by flow of water through a 10 mm cubic scaffold enclosed in a 3D printed test chamber. A constant flow rate was created with a 100 mL glass syringe driven by a syringe pump (Genie Plus, Kent Scientific, Torrington, CT, USA). Flow rates of 1 to 5 mL/min were selected based on flows that induce wall shear stresses for optimal osteoblastic differentiation in porous scaffolds in perfusion bioreactors[60]. Components were connected with 4 mm (ID) clear Tygon® tubing along with

push-to-connect valves and connectors. Within the chamber, scaffolds were surrounded by an elastomeric sleeve that prevented bypass of fluid around the scaffold. A pressure transducer (Validyne Engineering, P17-16-N-1) measured the pressure differential. Based on this system design, the maximum Reynold's number of 0.89 validated Darcian assumptions and resulted in a measurable permeability range of 1.9×10^{-13} – 6.66×10^{-6} m^2, a range well suited for porous bone[61].

The permeabilities of 5 Gyroid and 5 FKS scaffolds were calculated at flow rates of 1, 2, 3,4, and 5 mL/min with each measurement performed in triplicate. After loading a scaffold, the circuit was purged and stabilized, then a zero-pressure reading was collected for stagnant fluid. Pressure drops in each trial were collected over a 40-second period of steady flow, and permeability was calculated using MATLAB.

3.2.5 Statistical Analysis

Average values with standard deviations are displayed in figures unless otherwise noted. Significance was determined by two sample t-test and was denoted by (*, $P < 0.05$), (**, $P < 0.01$), (***, $P < 0.001$). Mechanical comparisons between test groups featured a population of 15 samples per group resulting in 28 degrees of freedom. Darcian permeability comparisons were made between the two scaffold groups with 5 unique samples per group evaluated at 5 independently tested flowrates resulting in 48 degrees of freedom.

3.3 Results

3.3.1 Structural Characterization

Representative scaffold photos and micro-CT images are shown in figure 15. Both topologies printed with comparable layer bonding, bridging, and corrugated surfaces (figure 15 A&D). 3D heatmaps from micro-CT (figure 15 B&E) highlight relative wall thickness where red areas are the thickest and green areas are the thinnest. This heatmap reveals an uneven wall thickness

distribution in both structures where thicker regions can be found on the exterior vertical walls (ZY and ZX planes). FKS and Gyroid were both prone to gaps between as-printed roads (figure 15 C&F). Micro-CT analysis captured the as-sintered porosity, wall thickness, and wall spacing of FKS and Gyroid scaffolds. Average as-designed porosity (70%) of FKS scaffolds increased to 74.00 $\pm$ 0.31% as-sintered. Gyroids showed an opposite trend, decreasing to 68.49 $\pm$ 1.18 %. At similar porosities, FKS scaffolds tended to have thicker walls that were spaced further apart. The average wall thickness for Gyroid scaffolds matched the extruder width of 0.413 $\pm$ 0.112 mm, where the FKS scaffolds increased to 0.424 $\pm$ 0.148 mm. Wall spacings for FKS and Gyroid were 1.212 $\pm$ 0.295 and 1.039 $\pm$ 0.200 mm, respectively. Lastly, the mean surface area to volume ratio (i.e. specific surface area) was calculated for FKS at 5.796 ± 0.042 mm^{-1} and for gyroid at 5.514 ± 0.175 mm^{-1}.

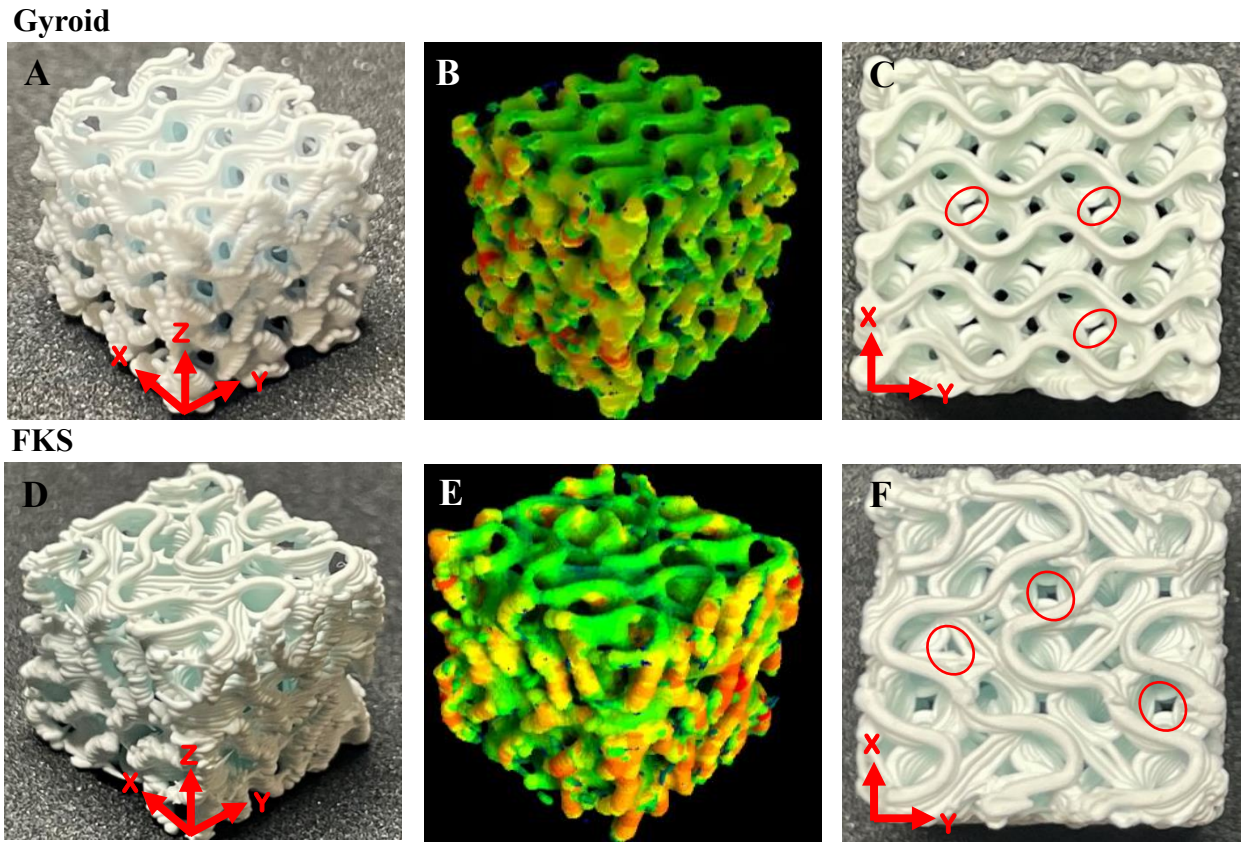

Figure 15. Representative images and micro-CT scans of 3D printed and sintered cubic scaffolds. The first column (A&D) of each row (Gyroid A-C, FKS D-F) compares an isometric view of each topology. The second column (B&E) displays 3D relative thickness "heatmaps" " of each topology from micro-CT data - red is thickest, green is thinnest. The last column (C&F) are top views of the x-y plane where examples of layer gaps are circled.

3.3.2 Mechanical Behavior

Stress-strain curves from compressive testing exhibited diverse behaviors which were classified into four categories: linear; exponential; reinforcing; or non-catastrophic (figure 16). Linear samples increased monotonically to a peak stress and then catastrophically failed. In these cases, initial and ultimate moduli were similar. Exponential behavior showed an increasing slope to the peak stress where the initial modulus was significantly lower than the ultimate modulus. Reinforcing samples were noted when local maxima occurred before the peak stress which was then followed by swift failure. Samples classified as non-catastrophic resisted complete failure and

maintained at least 25% of the maximum load after the peak stress had been reached. Across all topologies and testing orientations, 45% were classified as linear(A), 11% as exponential(B), 28% as reinforcing(C), and 16% as non-catastrophic(D). Regardless of classification, initial moduli were calculated from 0 to 0.5% strain, ultimate moduli were linearly fit from the start point to peak stress, and failure points were set at 75% of the peak load. Energy absorbed was the area under the curve between start and failure. Local maxima were indicated if a sudden decrease of 0.03 MPa or greater was observed. The four types of curves did not correlate with topology. Of all samples, 45% had local maxima, and transversely tested samples were 1.5 times more likely to have them. The average peak stress and energy absorbed were lower for samples that had local maxima when tested in the normal orientation. Of the samples showing non-catastrophic behavior, 89% were compressed in the transverse orientation.

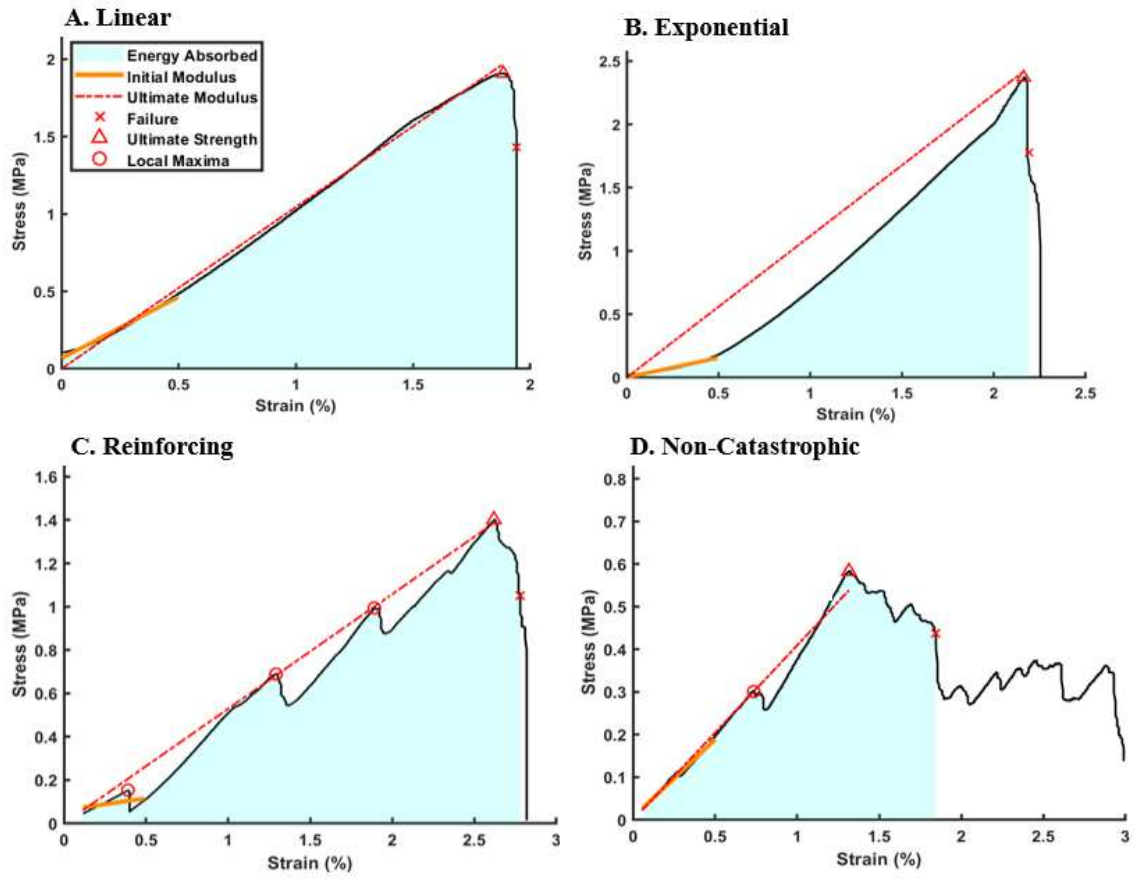

Figure 16. Classification of stress-strain curves from compressive testing. Stress-strain curves showing representative classification of linear (A), exponential (B), reinforcing(C), and non-catastrophic(D).

From the stress-strain curves, mechanical properties were calculated to quantify scaffold performance limits. Four sample groups are abbreviated FKS-N, FKS-T, GYR-N, and GYR-T, where "FKS" and "GYR" refer to the topology, and "N" and "T" refer to the normal and transverse direction of compression, respectively. Compressive strength and energy absorption analysis (figure 17) revealed that FKS scaffolds were significantly stronger and absorbed more energy than Gyroids in both testing orientations. FKS-N was 32% stronger than GYR-N with compressive strengths of 1.83 ± 0.72 MPa and 1.39 ± 0.35 MPa , respectively. Transverse strength was significantly weaker than normal strength for both topologies with 1.02 ± 0.28 MPa for FKS-T

and 0.63 ± 0.10 MPa for GYR-T. Energy absorption followed the same trend where FKS-N withstood 265 ± 145 J/m^3, a 49% increase over GYR-N, which absorbed 178 ± 56 J/m^3. Scaffolds tested transversely were again less robust than their normal counterparts showing absorptions of 152 ± 66 J/m^3 for FKS-T and 64 ± 13 J/m^3 for GYR-T, which indicated that both of these scaffolds were anisotropic.

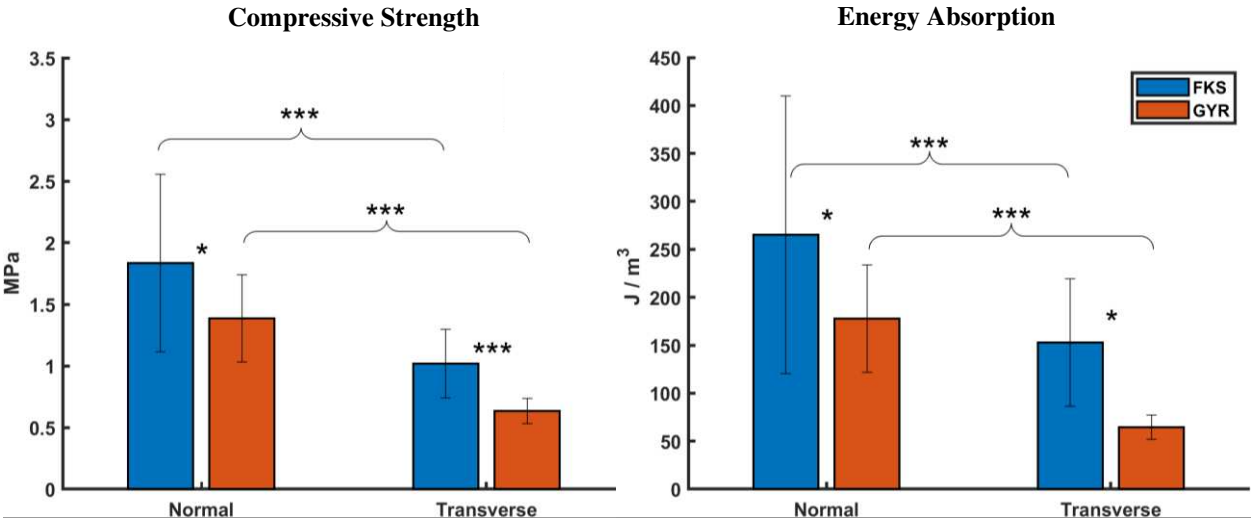

Figure 17. FKS scaffolds were stronger and absorbed more energy than Gyroids. Trends were similar for compressive strength and energy absorption where FKS scaffolds significantly outperformed Gyroids, and normal properties significantly exceeded transverse transverse properties. Sample size was n=15 for each test group. Statistical significance denoted by (*, P < 0.05), (**, P < 0.01), (***, P < 0.001).

Moduli were calculated using two methodologies to characterize scaffold stiffness at small strains (initial) and large strains (ultimate). No significant differences were observed between FKS and Gyroid in their initial or ultimate moduli (figure 18). The initial strains of FKS scaffolds were notably stiffer in the normal direction (49.6 ± 20.2 MPa) than the transverse direction (28.7 ± 16.0 MPa). Initial moduli of Gyroids did not significantly vary between normal and transverse

testing which resulted in values of 41.8 ± 23.9 MPa and 40.7 ± 21.0 MPa, respectively. Ultimate moduli differed significantly between testing orientations for both topologies where FKS-N (71.7 ± 23.3 MPa) was stiffer than FKS-T (40.9 ± 15.4 MPa) and GYR-N (67.6 ± 21.9 MPa) was stiffer than GYR-T (49.0 ± 20.6 MPa).

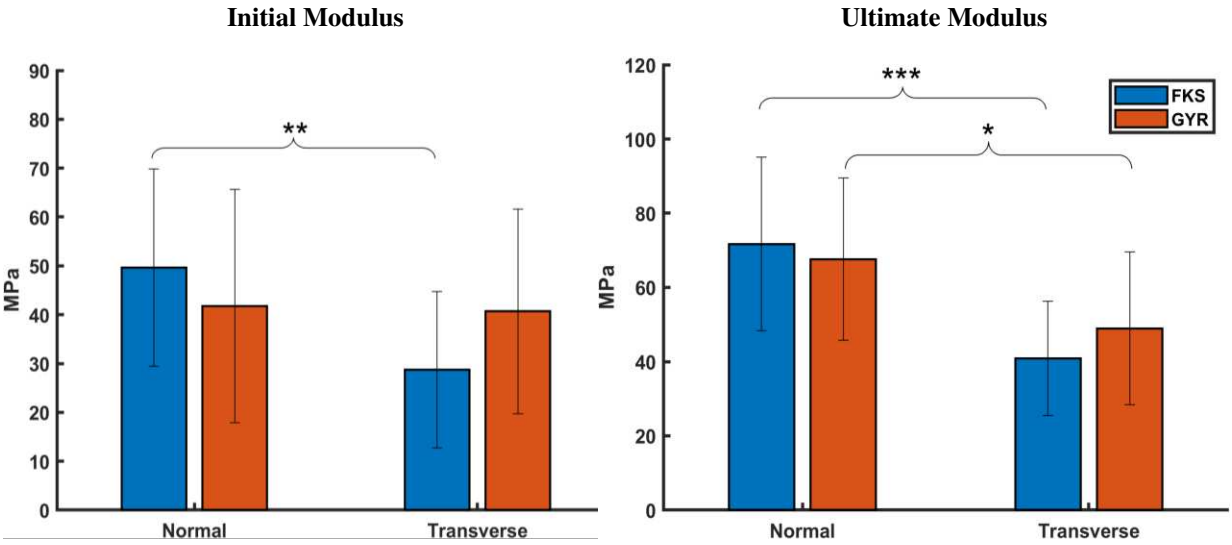

Figure 18. Scaffold stiffness varied by testing orientation, but not by structure. No significant difference could be found between the initial or ultimate moduli between FKS and Gyroid. Scaffolds tended to be stiffer in the normal orientation than the transverse orientation except for in the initial region of Gyroids. Sample size was n=15 for each test group. Statistical significance denoted by: (*, P < 0.05), (**, P < 0.01), (***, P < 0.001).

3.3.3 Permeability

The average Darcian permeability of FKS ($1.13 \pm 0.06 * 10^{-9}\, m^2$) was 11% lower than Gyroid ($1.27 \pm 0.20 * 10^{-9}\, m^2$) when tested in the normal direction (figure 19).

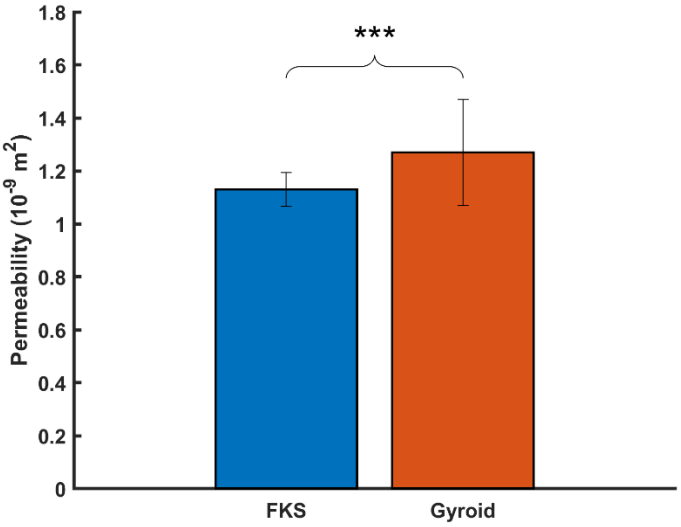

Figure 19. Gyroid scaffolds were more permeable than FKS scaffolds. Averages are displayed from a range of flow rates (1-5 ml/min) with five samples per flow rate per group. Statistical significance denoted by: (*, P < 0.05), (**, P < 0.01), (***, P < 0.001).

3.3.4 Surface Morphology and Fracture Behavior

Surface texture was consistent and densely consolidated in both FKS and Gyroid scaffolds. Roads were smooth and surfaces were corrugated due to the stacking of layers. Minor surface defects were observed in both topologies, mainly initiating at road boundaries and penetrating into the scaffold (figure 20). Little to no evidence of elastic deformation was seen. Outer regions of road cross-sections appeared to be denser than inner regions (figure 20B) in both topologies. In both normal and transverse loading, both scaffold types cracked internally along shear planes near the support points of suspended sections of scaffold pores (figure 21A). Cracks propagated in the direction of load (figure 21B), with occasional small deflections apparent at road boundaries (21B - 2, 3, 4).

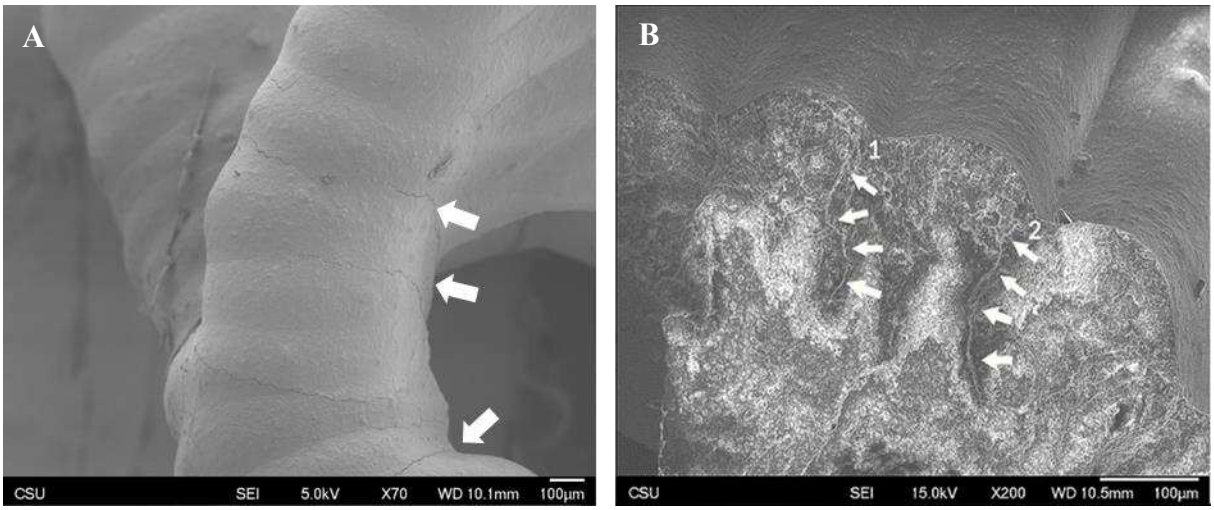

Figure 20. Surface texture and crack propagation. Representative images of Gyroid (A) and FKS (B) show that scaffold struts in both scaffold topologies are densely consolidated with smooth surface texture. Cracks propagated along road boundaries on the surfaces and penetrated into strut along road boundaries (B1) and (B2) in both topologies.

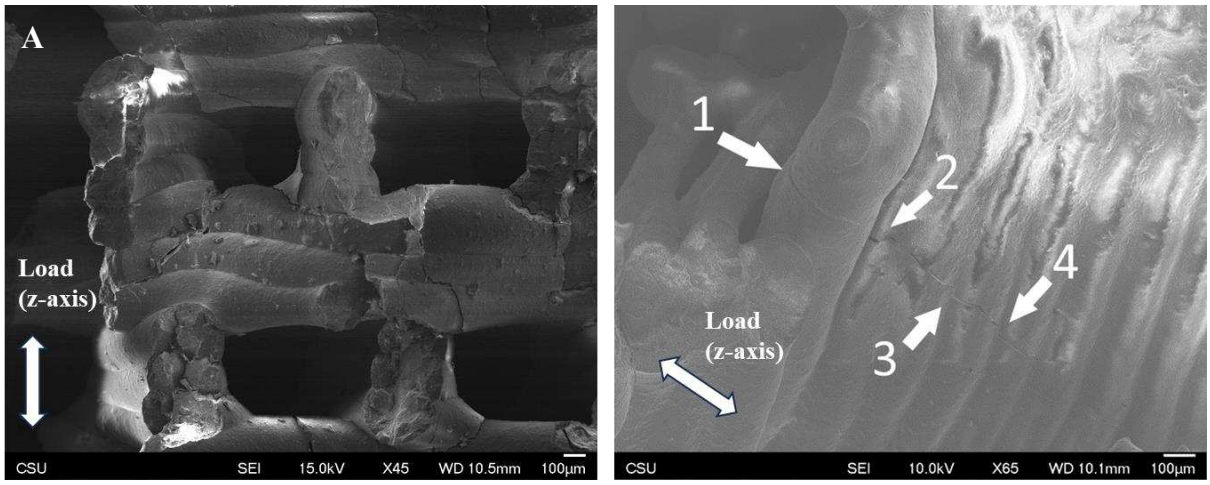

Figure 21. Shear failure in the direction of load. Representative SEM images of tested Gyroid (A) and FKS fragments (B) both fractured in the direction of compressive load. Image A shows shear-induced cracks at edges of open pores, and image (B) shows a crack that propagated through several roads, with occasional small deflections at road boundaries (B - 2, 3, 4).

3.4 Discussion

Structural characterization of each topology confirmed that robocasting could produce TPMS HAp scaffolds optimized for healing large bone defects. In terms of scaffold optimization, the critical

need to balance mechanical and osteogenic properties is dependent on the material and application. In 2021, Blazquez-Carmona et al. optimized HAp scaffolds specifically for regenerating load bearing defects and provided the key insight that since these *in vivo* procedures are stabilized by metal fixation, like intramedullary nails or fixation plates, the mechanical loads required by the scaffolds significantly change[62]. Mechanical testing of critical defect repairs in cadaveric canine limbs has shown that the bending stiffness of the bone stabilized by an external plate did not significantly change when the scaffold was removed[63]. This implies that metal fixation in large, load-bearing bone defects transfer much of the load around the defect which reduces the mechanical requirements of the scaffold, enabling a design shift in favor of maximizing osteogenesis. In terms of bone growth, there are demonstrated advantages of higher porosity scaffold[13], therefore, the highest porosity structure that meets the minimum mechanical and surface area requirements and mimics the stiffness of the targeted tissue is most desirable[64]. Pore size, which heavily influences cell behavior[13], has a generally accepted minimum of 300 µm for cell proliferation[6]. Pores ranging from 300-1200 µm have shown no significant differences in a study of bone formation [7]. Larger pores tend to harbor greater cell densities, and cells tend not to enter pores less than 5 – 10 times their diameter, thus justifying pore sizes at the upper end of the aforementioned range for an osteoblast [48], [65]. Another study by Klenke at al. showed that the volume of deposited bone increased as pore size increased[14]. The optimization by Blazquez-Carmona et al. recommended parameters of 59.3% porosity, 5.768 mm-1 specific surface area, and 360 µm pore size for their rectilinear HAp scaffolds in a large defect. Optimizations are difficult to compare due to variations in topology[66], so the TPMS scaffolds in this report were designed at the highest porosity (~70%) and pore size (~1mm) that were predicted to maintain the low end of trabecular bone strength based on previous studies[67]. The specific

surface area of 5.768 mm-1 was used as a nominal design goal. The as-sintered scaffold porosity, pore size and specific surface area values varied by topology in this report (74.00%, 1.212 mm, and 5.796 mm-1 for FKS and 68.49%, 1.039mm, and 5.514 mm-1 for Gyroid), but they were considered good fidelity for direct comparison due to their small variations. Furthermore, a comparison of a single high porosity design for each topology is valid because trends in scaffold strength and permeability are dominated by differences in topology, not porosity[22]. Some manufacturing defects did occur, such as ooze on the exterior faces and layer gaps (figure 15), which are believed to have caused the deviations from the as-designed 70% porosity. Furthermore, resolution in robocasting is limited by nozzle diameter which was set the smallest size (0.413mm) that permitted consistent viscous extrusion. Since the nozzle size was fixed, and therefore the wall thickness was fixed, the FKS and Gyroid could not be reliably produced with precisely the same structural parameters because porosity, pore size, and surface area are highly interrelated. Further difficulties in robocasting TPMS ceramics have been elaborated on in prior work[38].

The comparative properties of FKS and Gyroid scaffolds were in good agreement with current literature, and the performance of both of these topologies mimicked trabecular long bones. FKS scaffolds were shown to be significantly stronger and absorb more energy than Gyroid scaffolds in both normal and transverse compression, but no significant differences could be found between their moduli. In flow testing, FKS scaffolds were shown to be significantly less permeable than Gyroids scaffolds in the Darcian regime. Ravichander et. al. showed that FKS scaffolds with a linear porosity gradient manufactured using metal powder bed fusion (PBF) had higher compressive strength, Young's modulus, and energy absorption than Gyroids[68]. Zou et al. manufactured TPMS scaffolds using titanium PBF to show that FKS had a stiffer elastic modulus, greater compressive strength, and lower permeability than Gyroid. Lu et. al. demonstrated that

FKS and Gyroid had similar compressive moduli when simulated using FEA and tested using titanium PBF across a range of porosities[22]. In the same report, CFD calculations using both Darcy's law and Kozeny-Carman's relation revealed that FKS had the lowest permeability of all structures tested (including Gyroid), leading them to the conclusion that FKS may be the most favorable in scenarios where nutrient is not limiting, e.g., in bone fusion. Kapfer et. al. predicted using FEA that Gyroids have a larger Young's Modulus, but that FKS is more isotropic[69]. Asbai-Ghoudan et al. showed that FKS had lower permeability than Gyroid across a range of pore sizes and porosities[70]. Lu and their team also predicted FKS to be more isotropic than Gyroid using FEA, and consequently, they proposed that FKS might be better for compact bone scaffolds, while Gyroid might be better for trabecular bone scaffolds [56]. Our ceramic results are in good agreement with the trends seen between FKS and Gyroid in simulations and metal-based experiments. This current study demonstrates that the compressive strength of robocast FKS and Gyroid scaffolds (1-2 MPa) were in the low range of human cancellous bone in uniaxial compression (0.898 – 29.20 MPa)[71], and that their permeabilities (1.01 x 10-9 m2 to 2.18 x 10-9 m2) were similar to trabecular bone (0.4 – 11 x 10-9 m2) and to other scaffold literature[7], [72]. These findings confirm that Gyroid and FKS HAp scaffolds are well suited for use in large bone defects. FKS scaffolds show the most promise in mimicking natural trabecular bone strength in a high porosity ceramic. In designing BTE scaffolds, FKS scaffolds may indeed be better suited to applications of dense bone than Gyroids where strength is prioritized over permeability, as suggested by Lu [56].

In addition to strength and permeability, the ability of scaffolds to match the anisotropy and modulus of surrounding tissues is important for bone growth[73], but the variability of samples in this report was too high to draw significant conclusions. Standard deviations in the moduli of all

samples were greater than 30% which were likely attributed to manufacturing defects and the likelihood of brittle fracture. Unlike compressive strength, the stiffness of scaffolds in this report (40-70 MPa) failed to compare to the elastic modulus range for trabecular bone (105 – 1310 MPa)[71]. In order to improve the performance and reliability of robocast TPMS scaffolds, it was necessary to define a more robust method for analyzing cellular ceramics which, to the best of our knowledge, is absent in the literature. Different stress-strain curve types (figure 16) warranted a customized approach to quantify performance because linear regions and fracture modes differed. Traditional methods, such as the ASTM standard for advanced dense ceramics[74], describe a model for "isotropic, homogeneous, and continuous behavior" which does not describe the porous HAp scaffolds tested. Unlike typical elastic modulus analysis, stiffness calculations in this study were non-trivial because more than half of samples showed non-monotonic or second order behavior. Meille et. al. found that above a critical porosity (~50%) the compressive behavior of gelcast alumina scaffolds tended to shift from brittle to a more cellular-like fracture mode[75]. They explained that this was because high porosity ceramics fail by the bending or buckling of walls rather than the propagation of cracks between isolated pores. Interestingly, FKS and Gyroid scaffolds in the current study exhibited some key characteristics of both brittle and cellular fracture, suggesting that a "critical" inflection point at a porosity of 70% may exist for this fabrication method. "Linear" cases (figure 16A) showed high stiffness, swift failure, and a high standard deviation, as seen in brittle ceramic foams[75], while "Reinforcing" and "Non-catastrophic" cases (figures 16C and 16D) appeared to prevent crack propagation by isolating failures to struts on a weaker layer, as seen in cellular solids[76]. Regarding "Exponential" cases (figure 16B), Morgan et al. showed that moduli varied significantly based on the strain range chosen and that non-linear behavior existed even at small strains[77]. They recommended that a

second order polynomial fit be used in the region from 0 - 0.2% strain for a more robust stiffness definition, but the addition of this parameter makes comparison with scaffold literature and different behavior types more difficult. To capture the diverse scaffold behavior in the current study, a linear fit from 0 – 0.5% strain was selected for the initial modulus because it generally showed the lowest standard deviation across all sample groups. Limiting the linear fit region to an excessively small range results in high variation due to local failures, which can create a non-sensical approximation, such as seen in figure 16C. These early local failures could have resulted from protrusions on outer scaffold surfaces due to improper sanding, but they could not be differentiated from internal local failures which are implicit in the scaffold fabrication process. As a result, no outliers were rejected, and the same rule for initial modulus was applied to all samples. It is important to note that this initial modulus does not represent the overall load-bearing capacity of the cellular scaffold due to failures and possible self-reinforcement[67] of internal struts, which result in multiple linear regions on the stress-strain curve before ultimate compressive strength is reached (figure 16C). For this reason, “ultimate” modulus was defined to represent the pre-failure stiffness of the scaffold in order to better characterize the functional performance of the construct in a large bone defect. Innovations in fabricating high porosity TPMS ceramics are needed to reduce variability, shrink the gap between initial and ultimate moduli, and mitigate local failures for higher performance. Despite these shortcomings, this report shows that robocast ceramics are still suitable for use in large bone defect repair.

To better understand the behavior of cellular ceramics, it is critical to examine their failure modes. SEM imagery showed (unsurprisingly) that most cracks initiated at the interfacial boundary of roads. It is hypothesized that the layer-wise photocuring process prevented homogeneity among roads due to variance in parameters like wall thickness. Corrugated walls resulting from the

viscous extrusion process [38] created thinner walls between roads and therefore stress concentrations. Not only are these road boundaries thinner, but it is predicted that the curing varied as well. Ideally, a photocast road is mostly cured during deposition, enough to bridge open pores, and is then continuously cured by subsequent exposure passes. This can result in inconsistent curing between upper and lower regions of a road and between successive roads, which was not part of this study. It is hypothesized that this resulted in interfacial defects during sintering because stresses caused by thermal gradients and variance in shrinkage dissipated through these discontinuities. Cracks tended to propagate along grains rather than through them as they follow natural crack propagation pathways. From the relatively small size of HAp grains (87 nm), there was little fracture resistance, and SEM images did not reveal significant crack deviation. Such crack propagation behavior leads to a hypothesis that initial localized failure should immediately lead to overall failure of the scaffold, but this is not always the case. The scaffolds generally failed along shear planes near the support points of suspended sections of the scaffold (figure 20A). Due to the lattice-like nature of FKS and Gyroid structures, opportunities for self-reinforcement arose where cracks extended through the entirety of a scaffold section yet the section remained in contact with the previously connected structure (figure 20B). similar to behavior observed in prior work [67]. As these sections of roads fail and are shifted in the direction of the load force, they can become lodged against still-intact sections of the scaffold, thereby reinforcing the strut's integrity. It follows from these observations that all scaffolds of both topologies were weaker transversally due to the alignment of road boundaries and direction of applied loads. It is evident that anisotropy primarily resulted from layer-wise fabrication which made topological effects insignificant. The more irregular cross sections of FKS scaffolds[38] may have contributed to their increased strength in a ceramic because cracks required more deflection to become catastrophic, and opportunities

for self-reinforcement were greater. Previous work in our lab has shown similar self-reinforcing behavior in Gyroid HAp scaffolds at various porosities [67]. One key observation in both studies is a negative correlation between compressive strength and the propensity for self-reinforcement. Generally speaking, stronger scaffolds failed catastrophically (A and B in figure 16) whereas comparatively weaker scaffolds either showed early self-reinforcing or failed non-catastrophically (C and D in figure 16). This makes intuitive sense; self-reinforcing specifically requires failure to occur first. Preventing the formation of the microcracks that cause early failure has been discussed for quite some time [78]. While methods developed to model this failure in comparatively geometrically simple scaffolds have previously been investigated [79], [80], modeling of more complex TPMS ceramic structures is limited. In addition to limiting manufacturing defects that lead to microcracks, the erratic failure behavior inherent of ceramics further leads to a non-intuitive conclusion regarding potential scaffold strengthening mechanisms, that scaffolds with larger roads trend towards a decrease in overall strength. Limiting local material volume in ceramics has been discussed for decades [81], though due to the comparatively young age of additive manufacturing, empirical evaluation centered on road size of ceramic scaffolds has only relatively recently begun [82], [83].

3.5 Conclusions

In this study, FKS and Gyroid scaffolds were photocast in HAp to compare experimental properties. Bone regeneration scaffolds face a critical design compromise between strength and permeability which is fundamentally controlled by structure and porosity. Results indicated that both topologies could achieve the lower performance ranges of human trabecular bone for use in load-bearing defects stabilized by metal fixation, but FKS showed significant gains in strength at only a small penalty to permeability when compared to Gyroid scaffolds. As bone tissue

engineering progresses for high porosity ceramics, FKS again shows promising results among the TPMS options.

References

[1] L. Vidal, C. Kampleitner, M. Á. Brennan, A. Hoornaert, and P. Layrolle, "Reconstruction of Large Skeletal Defects: Current Clinical Therapeutic Strategies and Future Directions Using 3D Printing," Front. Bioeng. Biotechnol., vol. 8, p. 61, Feb. 2020, doi: 10.3389/fbioe.2020.00061.

[2] J. Franch, A. Barba, K. Rappe, Y. Maazouz, and M. Ginebra, "Use of three-dimensionally printed β-tricalcium phosphate synthetic bone graft combined with recombinant human bone morphogenic protein-2 to treat a severe radial atrophic nonunion in a Yorkshire terrier," Vet. Surg., p. vsu.13476, Jul. 2020, doi: 10.1111/vsu.13476.

[3] A. Roffi, G. S. Krishnakumar, N. Gostynska, E. Kon, C. Candrian, and G. Filardo, "The Role of Three-Dimensional Scaffolds in Treating Long Bone Defects: Evidence from Preclinical and Clinical Literature-A Systematic Review," BioMed Res. Int., vol. 2017, p. 8074178, 2017, doi: 10.1155/2017/8074178.

[4] M. Wagels, D. Rowe, S. Senewiratne, and D. R. Theile, "History of lower limb reconstruction after trauma: History of lower limb reconstruction after trauma," ANZ J. Surg., vol. 83, no. 5, pp. 348–353, May 2013, doi: 10.1111/j.1445-2197.2012.06271.x.

[5] D. Chang and K. Weber, "Use of a vascularized fibula bone flap and intercalary allograft for diaphyseal reconstruction after resection of primary extremity bone sarcomas," Plast Reconstr Surg, vol. 116, pp. 1918–1925, 2005.

[6] A. A. Zadpoor, "Bone tissue regeneration: the role of scaffold geometry," Biomater. Sci., vol. 3, no. 2, pp. 231–245, 2015, doi: 10.1039/C4BM00291A.

[7] H. Montazerian, E. Davoodi, M. Asadi-Eydivand, J. Kadkhodapour, and M. Solati-Hashjin, "Porous scaffold internal architecture design based on minimal surfaces: A compromise between permeability and elastic properties," Mater. Des., vol. 126, pp. 98–114, Jul. 2017, doi: 10.1016/j.matdes.2017.04.009.

[8] H. Montazerian, M. Zhianmanesh, E. Davoodi, A. S. Milani, and M. Hoorfar, "Longitudinal and radial permeability analysis of additively manufactured porous scaffolds: Effect of pore shape and porosity," Mater. Des., vol. 122, pp. 146–156, May 2017, doi: 10.1016/j.matdes.2017.03.006.

[9] Karande, Ong and Agrawal, "Diffusion in Musculoskeletal Tissue Engineering Scaffolds-Design Issues Related to Porosity, Permeability, Architecture, and Nutrient Mixing," Ann. Biomed. Eng., vol. 32, no. 12, pp. 1728–1743, Dec. 2004.

[10] M. R. Dias, P. R. Fernandes, J. M. Guedes, and S. J. Hollister, "Permeability analysis of scaffolds for bone tissue engineering," J. Biomech., vol. 45, no. 6, pp. 938–944, Apr. 2012, doi: 10.1016/j.jbiomech.2012.01.019.

[11] J. M. Kemppainen and S. J. Hollister, "Differential effects of designed scaffold permeability on chondrogenesis by chondrocytes and bone marrow stromal cells," Biomaterials, vol. 31, no. 2, pp. 279–287, Jan. 2010, doi: 10.1016/j.biomaterials.2009.09.041.

[12] K. A. Athanasiou, C.-F. Zhu, D. R. Lanctot, C. M. Agrawal, and X. Wang, “Fundamentals of Biomechanics in Tissue Engineering of Bone,” Tissue Eng., vol. 6, no. 4, pp. 361–381, Aug. 2000, doi: 10.1089/107632700418083.

[13] V. Karageorgiou and D. Kaplan, “Porosity of 3D biomaterial scaffolds and osteogenesis,” Biomaterials, vol. 26, no. 27, pp. 5474–5491, Sep. 2005, doi: 10.1016/j.biomaterials.2005.02.002.

[14] F. M. Klenke, Y. Liu, H. Yuan, E. B. Hunziker, K. A. Siebenrock, and W. Hofstetter, “Impact of pore size on the vascularization and osseointegration of ceramic bone substitutesin vivo,” J. Biomed. Mater. Res. A, vol. 85A, no. 3, pp. 777–786, Jun. 2008, doi: 10.1002/jbm.a.31559.

[15] S. Tarafder, V. K. Balla, N. M. Davies, A. Bandyopadhyay, and S. Bose, “Microwave-sintered 3D printed tricalcium phosphate scaffolds for bone tissue engineering,” J. Tissue Eng. Regen. Med., vol. 7, no. 8, pp. 631–641, 2013, doi: 10.1002/term.555.

[16] J. L. Vondran, W. Sun, and C. L. Schauer, “Crosslinked, electrospun chitosan–poly (ethylene oxide) nanofiber mats,” J. Appl. Polym. Sci., vol. 109, pp. 968–975, 2008.

[17] S. J. Hollister, “Porous scaffold design for tissue engineering,” Nat. Mater., vol. 4, no. 7, pp. 518–524, Jul. 2005, doi: 10.1038/nmat1421.

[18] S. Wu, X. Liu, K. W. K. Yeung, C. Liu, and X. Yang, “Biomimetic porous scaffolds for bone tissue engineering,” Mater. Sci. Eng. R Rep., vol. 80, pp. 1–36, Jun. 2014, doi: 10.1016/j.mser.2014.04.001.

[19] L. Yuan, S. Ding, and C. Wen, “Additive manufacturing technology for porous metal implant applications and triple minimal surface structures: A review,” Bioact. Mater., vol. 4, no. 1, pp. 56–70, Mar. 2019, doi: 10.1016/j.bioactmat.2018.12.003.

[20] L. Germain, C. A. Fuentes, A. W. van Vuure, A. des Rieux, and C. Dupont-Gillain, “3D-printed biodegradable gyroid scaffolds for tissue engineering applications,” Mater. Des., p. 10, 2018, doi: https://doi.org/10.1016/j.matdes.2018.04.037.

[21] D. W. Abueidda, M. Elhebeary, C.-S. (Andrew) Shiang, S. Pang, R. K. Abu Al-Rub, and I. M. Jasiuk, “Mechanical properties of 3D printed polymeric Gyroid cellular structures: Experimental and finite element study,” Mater. Des., vol. 165, p. 107597, Mar. 2019, doi: 10.1016/j.matdes.2019.107597.

[22] Y. Lu, L. Cheng, Z. Yang, J. Li, and H. Zhu, “Relationship between the morphological, mechanical and permeability properties of porous bone scaffolds and the underlying microstructure,” PLOS ONE, vol. 15, no. 9, p. e0238471, Sep. 2020, doi: 10.1371/journal.pone.0238471.

[23] A. Karakoc, “RegionTPMS — Region based triply periodic minimal surfaces (TPMS) for 3-D printed multiphase bone scaffolds with exact porosity values,” SoftwareX, vol. 16, p. 100835, Dec. 2021, doi: 10.1016/j.softx.2021.100835.

[24] M. Alizadeh-Osgouei, Y. Li, A. Vahid, A. Ataee, and C. Wen, “High strength porous PLA gyroid scaffolds manufactured via fused deposition modeling for tissue-engineering applications,” Smart Mater. Med., vol. 2, pp. 15–25, 2021, doi: 10.1016/j.smaim.2020.10.003.

[25] D.-J. Yoo, “Advanced porous scaffold design using multi-void triply periodic minimal surface models with high surface area to volume ratios,” Int. J. Precis. Eng. Manuf., vol. 15, no. 8, pp. 1657–1666, Aug. 2014, doi: 10.1007/s12541-014-0516-5.

[26] A. Bigham, F. Foroughi, E. Rezvani Ghomi, M. Rafienia, R. E. Neisiany, and S. Ramakrishna, “The journey of multifunctional bone scaffolds fabricated from traditional toward modern techniques,” Bio-Des. Manuf., vol. 3, no. 4, pp. 281–306, Dec. 2020, doi: 10.1007/s42242-020-00094-4.

[27] S. Ma, Q. Tang, Q. Feng, J. Song, X. Han, and F. Guo, “Mechanical behaviours and mass transport properties of bone-mimicking scaffolds consisted of gyroid structures manufactured using selective laser melting,” J. Mech. Behav. Biomed. Mater., vol. 93, pp. 158–169, May 2019, doi: 10.1016/j.jmbbm.2019.01.023.

[28] I. Maskery et al., “Insights into the mechanical properties of several triply periodic minimal surface lattice structures made by polymer additive manufacturing,” Polymer, vol. 152, pp. 62–71, Sep. 2018, doi: 10.1016/j.polymer.2017.11.049.

[29] G. E. Schröder-Turk et al., “The chiral structure of porous chitin within the wing-scales of Callophrys rubi,” J. Struct. Biol., vol. 174, no. 2, pp. 290–295, May 2011, doi: 10.1016/j.jsb.2011.01.004.

[30] H.-U. Nissen, “Crystal Orientation and Plate Structure in Echinoid Skeletal Units,” Science, vol. 166, no. 3909, pp. 1150–1152, Nov. 1969, doi: 10.1126/science.166.3909.1150.

[31] J. W. Galusha, L. R. Richey, J. S. Gardner, J. N. Cha, and M. H. Bartl, “Discovery of a diamond-based photonic crystal structure in beetle scales.,” Phys. Rev., vol. 77, no. 5 Pt 1.

[32] J. Shi, L. Zhu, L. Li, Z. Li, J. Yang, and X. Wang, “A TPMS-based method for modeling porous scaffolds for bionic bone tissue engineering,” Sci. Rep., vol. 8, no. 1, p. 7395, May 2018, doi: 10.1038/s41598-018-25750-9.

[33] C. Yan, L. Hao, A. Hussein, and P. Young, “Ti–6Al–4V triply periodic minimal surface structures for bone implants fabricated via selective laser melting,” J. Mech. Behav. Biomed. Mater., vol. 51, pp. 61–73, Nov. 2015, doi: 10.1016/j.jmbbm.2015.06.024.

[34] A. Bruyas et al., “Systematic characterization of 3D-printed PCL/b-TCP scaffolds for biomedical devices and bone tissue engineering: Influence of composition and porosity,” J Mater Res, vol. 33, no. 14, pp. 1948–1959, Jul. 2018.

[35] S. Restrepo, S. Ocampo, J. A. Ramírez, C. Paucar, and C. García, “Mechanical properties of ceramic structures based on Triply Periodic Minimal Surface (TPMS) processed by 3D printing,” J. Phys. Conf. Ser., vol. 935, no. 1, p. 012036, Dec. 2017, doi: 10.1088/1742-6596/935/1/012036.

[36] X. Peng et al., “Elastic Response of Anisotropic Gyroid Cellular Structures under Compression: Parametric Analysis,” Mater. Des., p. 109706, Apr. 2021, doi: 10.1016/j.matdes.2021.109706.

[37] S. Eqtesadi, A. Motealleh, A. Pajares, F. Guiberteau, and P. Miranda, “Improving mechanical properties of 13–93 bioactive glass robocast scaffold by poly (lactic acid) and poly (ε-

caprolactone) melt infiltration," J. Non-Cryst. Solids, vol. 432, pp. 111–119, Jan. 2016, doi: 10.1016/j.jnoncrysol.2015.02.025.

[38] V. Baumer, E. Gunn, V. Riegle, C. Bailey, C. Shonkwiler, and D. Prawel, "Robocasting of Ceramic Fischer–Koch S Scaffolds for Bone Tissue Engineering," J. Funct. Biomater., vol. 14, no. 5, p. 251, Apr. 2023, doi: 10.3390/jfb14050251.

[39] U. K. Roopavath, S. Malferrari, A. Van Haver, F. Verstreken, S. N. Rath, and D. M. Kalaskar, "Optimization of extrusion based ceramic 3D printing process for complex bony designs," Mater. Des., vol. 162, pp. 263–270, Jan. 2019, doi: 10.1016/j.matdes.2018.11.054.

[40] M. Tilton, A. Borjali, J. C. Griffis, K. M. Varadarajan, and G. P. Manogharan, "Fatigue properties of Ti-6Al-4V TPMS scaffolds fabricated via laser powder bed fusion," Manuf. Lett., vol. 37, pp. 32–38, Sep. 2023, doi: 10.1016/j.mfglet.2023.06.005.

[41] M. Jin et al., "Investigation on the mechanical properties of TPMS porous structures fabricated by laser powder bed fusion," J. Manuf. Process., vol. 76, pp. 559–574, Apr. 2022, doi: 10.1016/j.jmapro.2022.02.035.

[42] A. Mulhi, S. Dehgahi, P. Waghmare, and A. Qureshi, "Dimensional assessment of uniformly periodic porosity primitive TPMS lattices using additive manufacturing laser powder bed fusion technique," Int. J. Adv. Manuf. Technol., vol. 124, no. 7, pp. 2127–2148, Feb. 2023, doi: 10.1007/s00170-022-10578-5.

[43] X. Lv, F. Ye, L. Cheng, S. Fan, and Y. Liu, "Binder jetting of ceramics: Powders, binders, printing parameters, equipment, and post-treatment," Ceram. Int., vol. 45, no. 10, pp. 12609–12624, Jul. 2019, doi: 10.1016/j.ceramint.2019.04.012.

[44] A. Butscher, M. Bohner, S. Hofmann, L. Gauckler, and R. Müller, "Structural and material approaches to bone tissue engineering in powder-based three-dimensional printing," Acta Biomater., vol. 7, no. 3, pp. 907–920, Mar. 2011, doi: 10.1016/j.actbio.2010.09.039.

[45] G. A. Fielding, A. Bandyopadhyay, and S. Bose, "Effects of silica and zinc oxide doping on mechanical and biological properties of 3D printed tricalcium phosphate tissue engineering scaffolds," Dent. Mater., vol. 28, no. 2, pp. 113–122, Feb. 2012, doi: 10.1016/j.dental.2011.09.010.

[46] S. K. Nandi, G. Fielding, D. Banerjee, A. Bandyopadhyay, and S. Bose, "3D-printed β-TCP bone tissue engineering scaffolds: Effects of chemistry on in vivo biological properties in a rabbit tibia model," J. Mater. Res., vol. 33, no. 14, pp. 1939–1947, Jul. 2018, doi: 10.1557/jmr.2018.233.

[47] M. Schwentenwein and J. Homa, "Additive Manufacturing of Dense Alumina Ceramics," Int. J. Appl. Ceram. Technol., vol. 12, no. 1, pp. 1–7, Jan. 2015, doi: 10.1111/ijac.12319.

[48] F. P. W. Melchels, A. M. C. Barradas, C. A. van Blitterswijk, J. de Boer, J. Feijen, and D. W. Grijpma, "Effects of the architecture of tissue engineering scaffolds on cell seeding and culturing," Acta Biomater., vol. 6, no. 11, pp. 4208–4217, Nov. 2010, doi: 10.1016/j.actbio.2010.06.012.

[49] J.-W. Lee, Y.-H. Lee, H. Lee, Y.-H. Koh, and H.-E. Kim, "Improving mechanical properties of porous calcium phosphate scaffolds by constructing elongated gyroid structures using

digital light processing," Ceram. Int., vol. 47, no. 3, Art. no. 3, Feb. 2021, doi: 10.1016/j.ceramint.2020.09.164.

[50] Y. Zeng et al., "3D printing of hydroxyapatite scaffolds withgood mechanical and biocompatible properties by digital light processing," J. Mater. Sci., vol. 53, no. 9, pp. 6291–6301, May 2018, doi: 10.1007/s10853-018-1992-2.

[51] C. Schmidleithner, S. Malferrari, R. Palgrave, D. Bomze, M. Schwentenwein, and D. M. Kalaskar, "Application of high resolution DLP stereolithography for fabrication of tricalcium phosphate scaffolds for bone regeneration," Biomed. Mater., vol. 14, no. 4, p. 045018, Jun. 2019, doi: 10.1088/1748-605X/ab279d.

[52] S. Bose, D. Ke, H. Sahasrabudhe, and A. Bandyopadhyay, "Additive manufacturing of biomaterials," Prog. Mater. Sci., vol. 93, pp. 45–111, Apr. 2018, doi: 10.1016/j.pmatsci.2017.08.003.

[53] N. Travitzky et al., "Additive Manufacturing of Ceramic-Based Materials: Additive Manufacturing of Ceramic-Based Materials," Adv. Eng. Mater., vol. 16, no. 6, pp. 729–754, Jun. 2014, doi: 10.1002/adem.201400097.

[54] E. Peng, D. Zhang, and J. Ding, "Ceramic Robocasting: Recent Achievements, Potential, and Future Developments," Adv. Mater., vol. 30, no. 47, p. 1802404, Nov. 2018, doi: 10.1002/adma.201802404.

[55] A. M. Abou-Ali, O. Al-Ketan, R. Rowshan, and R. Abu Al-Rub, "Mechanical Response of 3D Printed Bending-Dominated Ligament-Based Triply Periodic Cellular Polymeric Solids," J. Mater. Eng. Perform., vol. 28, no. 4, pp. 2316–2326, Apr. 2019, doi: 10.1007/s11665-019-03982-8.

[56] Y. Lu, W. Zhao, Z. Cui, H. Zhu, and C. Wu, "The anisotropic elastic behavior of the widely-used triply-periodic minimal surface based scaffolds," J. Mech. Behav. Biomed. Mater., vol. 99, pp. 56–65, Nov. 2019, doi: 10.1016/j.jmbbm.2019.07.012.

[57] Lopez Ambrosio, Katherine V., "HYDROXYAPATITE STRUCTURES CREATED BY ADDITIVE MANUFACTURING WITH EXTRUDED PHOTOPOLYMER," Master's Thesis, Colorado State University, Ft. Collins, CO, 2019.

[58] "Isaacson et al. - 2022 - Compressive properties and failure behavior of pho.pdf."

[59] J. Santos, T. Pires, B. P. Gouveia, A. P. G. Castro, and P. R. Fernandes, "On the permeability of TPMS scaffolds," J. Mech. Behav. Biomed. Mater., vol. 110, p. 103932, Oct. 2020, doi: 10.1016/j.jmbbm.2020.103932.

[60] F. Zhao, B. Van Rietbergen, K. Ito, and S. Hofmann, "Flow rates in perfusion bioreactors to maximise mineralisation in bone tissue engineering in vitro," J. Biomech., vol. 79, pp. 232–237, Oct. 2018, doi: 10.1016/j.jbiomech.2018.08.004.

[61] G. Baroud, R. Falk, M. Crookshank, S. Sponagel, and T. Steffen, "Experimental and theoretical investigation of directional permeability of human vertebral cancellous bone for cement infiltration," J. Biomech., vol. 37, no. 2, Art. no. 2, Feb. 2004, doi: 10.1016/S0021-9290(03)00246-X.

[62] P. Blázquez-Carmona, J. A. Sanz-Herrera, F. J. Martínez-Vázquez, J. Domínguez, and E. Reina-Romo, "Structural optimization of 3D-printed patient-specific ceramic scaffolds for in vivo bone regeneration in load-bearing defects," J. Mech. Behav. Biomed. Mater., vol. 121, p. 104613, 2021, doi: https://doi.org/10.1016/j.jmbbm.2021.104613.

[63] Schneiderhan, Adam, "A NOVEL APPROACH FOR CRITICAL BONE DEFECT REPAIR," Master's Thesis, Colorado State University, Ft. Collins, CO, 2022.

[64] S. Sturm, S. Zhou, Y.-W. Mai, and Q. Li, "On stiffness of scaffolds for bone tissue engineering—a numerical study," J. Biomech., vol. 43, no. 9, pp. 1738–1744, Jun. 2010, doi: 10.1016/j.jbiomech.2010.02.020.

[65] F. P. W. Melchels et al., "The influence of the scaffold design on the distribution of adhering cells after perfusion cell seeding," Biomaterials, vol. 32, no. 11, pp. 2878–2884, Apr. 2011, doi: 10.1016/j.biomaterials.2011.01.023.

[66] M. Bahraminasab, "Challenges on optimization of 3D-printed bone scaffolds," Biomed. Eng. OnLine, vol. 19, no. 1, p. 69, Dec. 2020, doi: 10.1186/s12938-020-00810-2.

[67] N. Isaacson et al., "Compressive properties and failure behavior of photocast hydroxyapatite gyroid scaffolds vary with porosity," J. Biomater. Appl., p. 088532822110739, Mar. 2022, doi: 10.1177/08853282211073904.

[68] B. B. Ravichander, S. H. Jagdale, and G. Kumar, "Surface Morphology, Compressive Behavior, and Energy Absorption of Graded Triply Periodic Minimal Surface 316L Steel Cellular Structures Fabricated by Laser Powder Bed Fusion," Materials, vol. 15, no. 23, Art. no. 23, Jan. 2022, doi: 10.3390/ma15238294.

[69] S. C. Kapfer, S. T. Hyde, K. Mecke, C. H. Arns, and G. E. Schröder-Turk, "Minimal surface scaffold designs for tissue engineering," Biomaterials, vol. 32, no. 29, pp. 6875–6882, Oct. 2011, doi: 10.1016/j.biomaterials.2011.06.012.

[70] R. Asbai-Ghoudan, S. Ruiz de Galarreta, and N. Rodriguez-Florez, "Analytical model for the prediction of permeability of triply periodic minimal surfaces," J. Mech. Behav. Biomed. Mater., vol. 124, p. 104804, Dec. 2021, doi: 10.1016/j.jmbbm.2021.104804.

[71] L. Rincón-Kohli and P. K. Zysset, "Multi-axial mechanical properties of human trabecular bone," Biomech. Model. Mechanobiol., vol. 8, no. 3, pp. 195–208, Jun. 2009, doi: 10.1007/s10237-008-0128-z.

[72] M. J. Grimm and J. L. Williams, "Measurements of permeability in human calcaneal trabecular bone," J. Biomech., vol. 30, no. 7, Art. no. 7, Jul. 1997, doi: 10.1016/S0021-9290(97)00016-X.

[73] J. Henkel et al., "Bone Regeneration Based on Tissue Engineering Conceptions — A 21st Century Perspective," Bone Res., vol. 1, no. 3, pp. 216–248, Sep. 2013, doi: 10.4248/BR201303002.

[74] ASTM C28 Committee, "C1424-15 Test Method for Monotonic Compressive Strength of Advanced Ceramics at Ambient Temperature," ASTM International. doi: 10.1520/C1424-15.

[75] S. Meille, M. Lombardi, J. Chevalier, and L. Montanaro, “Mechanical properties of porous ceramics in compression: On the transition between elastic, brittle, and cellular behavior,” J. Eur. Ceram. Soc., vol. 32, no. 15, pp. 3959–3967, Nov. 2012, doi: 10.1016/j.jeurceramsoc.2012.05.006.

[76] L. J. Gibson and M. F. Ashby, Cellular Solids: Structure and Properties, 2nd ed. in Cambridge Solid State Science Series. Cambridge: Cambridge University Press, 1997. doi: 10.1017/CBO9781139878326.

[77] E. F. Morgan and T. M. Keaveny, “Dependence of yield strain of human trabecular bone on anatomic site,” J. Biomech., vol. 34, no. 5, pp. 569–577, May 2001, doi: 10.1016/S0021-9290(01)00011-2.

[78] J. Lankford, W. W. Predebon, J. M. Staehler, G. Subhash, B. J. Pletka, and C. E. Anderson, “The role of plasticity as a limiting factor in the compressive failure of high strength ceramics,” Mech. Mater., vol. 29, no. 3–4, pp. 205–218, Aug. 1998, doi: 10.1016/S0167-6636(98)00023-4.

[79] M. Genet, M. Houmard, S. Eslava, E. Saiz, and A. P. Tomsia, “A two-scale Weibull approach to the failure of porous ceramic structures made by robocasting: Possibilities and limits,” J. Eur. Ceram. Soc., vol. 33, no. 4, pp. 679–688, Apr. 2013, doi: 10.1016/j.jeurceramsoc.2012.11.001.

[80] A. Gross, P. Pantidis, K. Bertoldi, and S. Gerasimidis, “Correlation between topology and elastic properties of imperfect truss-lattice materials,” J. Mech. Phys. Solids, vol. 124, pp. 577–598, Mar. 2019, doi: 10.1016/j.jmps.2018.11.007.

[81] B. Bergman, “On the estimation of the Weibull modulus,” J. Mater. Sci. Lett., vol. 3, no. 8, pp. 689–692, Aug. 1984, doi: 10.1007/BF00719924.

[82] I. Sabree, J. E. Gough, and B. Derby, “Mechanical properties of porous ceramic scaffolds: Influence of internal dimensions,” Ceram. Int., vol. 41, no. 7, pp. 8425–8432, Aug. 2015, doi: 10.1016/j.ceramint.2015.03.044.

[83] R. Thiraux, A. D. Dupuy, T. Lei, T. J. Rupert, A. Mohraz, and L. Valdevit, “Damage tolerance in additively manufactured ceramic architected materials,” J. Eur. Ceram. Soc., vol. 42, no. 13, pp. 5893–5903, Oct. 2022, doi: 10.1016/j.jeurceramsoc.2022.05.059.

CHAPTER 3: METHODS FOR A MULTI-CHANNEL PERFUSION BIOREACTOR SYSTEM FOR MINERALIZING 3D SCAFFOLDS IN BONE TISSUE ENGINEERING

4.1 Introduction

Synthetic bone tissue scaffolds are a promising alternative to current clinical techniques for treating large bone defects [1-2]. Scaffolds provide a three-dimensional (3D) environment that mimics the properties of natural bone to accelerate osteogenesis. Optimal scaffolds should match the mechanical properties of the implantation site, feature a highly porous network of interconnected channels to facilitate mass transport, and exhibit surface properties for the attachment, proliferation, and differentiation of bone cell lineages[1]. 3D printing has enabled the manufacture of complex scaffold topologies that meet these requirements in a variety of biomaterials which has led to rapidly expanding research [3-9]. Such expansion has led to the need for more efficient bioreactors that provide reproducible conditions for comparing the *in vitro* cell growth on these biomimetic constructs.

Perfusion bioreactors are a leading method for creating a reproducible environment for *in vitro* osteogenesis, and they have been shown to produce clinically relevant volumes of bone [10-14]. Perfusion bioreactors overcome the limitations of static cultures, spinner flasks, and rotating wall vessels by providing superior nutrient mass transport, waste removal, and mechanical stimulation through fluid flow[15]. Perfusion systems are widely reported to enhance mineralized matrix deposition and increase osteoblastic signal expression by means of their fluid-induced shear stresses and efficient nutrient delivery[16-18]. The permeability of scaffolds is an important consideration because it measures the combined effect of the most critical structural parameters (porosity, pore size, pore shape, orientation, tortuosity, and interconnectivity) on fluid conductance, and therefore, on cell growth [19]. Moreover, the permeability of a scaffold under constant flow determines the magnitude of the induced pressures and shear stresses[17]. In some

cases, a highly permeable scaffold may be most favorable because mass transport would incur less resistance. Conversely, a scaffold with higher tortuosity, and likely lower permeability, may better distribute cells and shear stresses for more homogeneous growth[20]. Perfusion bioreactor systems are essential in evaluating the effects of scaffold structure and permeability on cell growth in a controlled environment.

Comparisons between perfusion studies are difficult due to the wide array of parameters that affect cell growth. Changes in cell type, seeding density, bioreactor layout, scaffold design, flow rate, oxygen monitoring, and analytical methods significantly affect the outcomes, and essential variables for reproducibly are often underreported [21], [22]. For these reasons, an "optimal" design struggles to emerge because each system is built for a unique function. Additionally, sample sizes are often limited in perfusion studies due to the high cost of multi-channel peristaltic pumps, limited incubator space, terminal assays, and long culture times. There is a need for more efficient bioreactors to culture higher sample numbers in a compact space, as well as a need for designs that can scale to operate many bioreactors simultaneously for use in robust comparison studies. In this report, we design and validate a 4-channel axisymmetric bioreactor, based on layout from Schmid et al.[23], for repeatably testing the effects of perfusion on scaffolds in higher sample volumes than single channel designs, from a single pump. The system design is presented in depth for repeatability and reproducibility, and it is validated through computation fluid dynamics (CFD) and *in vitro* testing to show that osteogenic effects are consistent between bioreactors and significant compared to static controls.

4.2 Materials and Methods

4.2.1 Scaffold Design

Additive manufacturing of synthetic bone scaffolds enables excellent control of implant design. The outer shape can be matched to medical scans for a patient-specific fit, and the internal structure can be designed in different topologies tuned to various sizes to elicit specific properties[2]. In bone tissue engineering, triply periodic minimal surfaces (TPMS) are an attractive infill method due to their ability to mimic bone through their smoothly interconnected porous structure[6]. Furthermore, their scalable unit cell topology allows for more customized features like functionally graded surfaces[24]. Among these surfaces, the gyroid has been popularized because of its relatively high surface area, energy absorption, mechanical strength, stiffness, and permeability at high porosities[25]. While the gyroid has been extensively studied mechanically through computational studies, many fewer studies have investigated its potential for cell growth making it a preferred choice for this study.

Scaffolds can be 3D printed from a countless number of biomaterials such as metals like titanium and ceramics like hydroxyapatite, natural polymers like collagen or synthetic polymers like polylactic acid, or composites like bioglass [26]. These material choices are important to consider in a bioreactor design because they have effects on parameters like cell seeding, sterilization, analytical approaches, and scaffold handling. Surface properties influence scaffold seeding times and densities, autoclavable materials offer advantages to prevent contamination, and brittle materials may prove difficult to assemble and disassemble non-destructively. Calcium-phosphate based ceramics are well established in bone tissue engineering because of their compositional similarities to native bone, which is 65% hydroxyapatite by dry weight[1], which exhibits biomimicry through similar protein attachment and mechanical behavior[26], [27]. Beta tricalcium phosphate (β-TCP) was selected for this study because of its demonstrated bioactivity

among the calcium appetite options[28], [29]. This brittle material creates several challenges which are discussed below in bioreactor design and workflow.

Once scaffold structural and material choices are made, porosity and pore size are the next most important factors of scaffold design. With respect to bone growth, there are no demonstrated advantages of lower scaffold porosity, therefore, the highest porosity structure that meets the minimum mechanical and surface area requirements while mimicking the stiffness of the targeted tissue is most desirable[30], [31]. Pore size, which heavily influences cell behavior, and in this case controls the surface area at a given porosity, has a generally accepted minimum of 300 um for cell proliferation[32]. Pores ranging from 300-1200 um showed no significant differences in a study of bone formation [33]. Larger pores tend to harbor greater cell densities, and cells tend not to enter pores less than 5 – 10 times their diameter, thus justifying pore sizes at the upper end of the aforementioned range[34], [35]. Another study by Klenke at al. showed that the volume of deposited bone increased as pore size increased[36]. Human trabecular long bones have an ultimate compressive strength range of 0.90 – 29.20 MPa and an elastic modulus range of 105 – 1310 MPa [37]. To meet the low end of the mechanical requirements, a β -TCP scaffold with a nominal 70% porous gyroid infill and a 1000 um average pore size was fabricated through photocasting based on previous work[38], [39] and literature values[40], [41]. The scaffold shape was standardized to a 1 cm cube to match testing standards.

4.2.2 Bioreactor Design

The purpose of this design was to culture multiple scaffolds on a single fluid line to increase the efficiency of sample numbers from a given pump whilst maintaining the basic principles of a perfusion system. Bancroft et al. describes the essential functions as: 1) delivering flow through the scaffolds with minimal escaping or “non-perfusing flow” around them 2) providing a repeatable, consistent, and homogenous flow distribution to the constructs, and 3) creating and

maintaining a sterile and biocompatible environment [10]. The first requirement posed a challenge for ceramic scaffolds because a tight seal on a brittle scaffold can lead to fractures. Adapting a solution from Schmid et al., an elastomeric sleeve was 3D printed from a clear biocompatible photopolymer (Biomed Elastic, Shore 50A Hardness) on a Form Labs 3B+ printer to tightly fit both the scaffold and chamber[23] without damaging the scaffold. An additional benefit of this design is that this sleeve enabled handling of the scaffolds without affecting cultured surfaces. Meeting the second requirement took several iterations of the design. The first attempts simply took four single channel bioreactors like those seen in the literature and connected them in parallel with tubing to be powered by one pump. However, at the nominally low flow rates for perfusion (~1 ml/min), small twists and deviations in the tubing were observed to trap air bubbles and divert flow to the path of least resistance. From this, it was hypothesized that smaller divergence between paths would decrease variability and create a more compact design. Because most subsequent analyses (e.g. cell studies, mechanical testing, computed tomography, etc.) require at least three samples for statistical significance and given that human error can easily damage samples, it was decided that grouping four scaffolds into one bioreactor assembly would be most efficient. Because perfusion studies typically feature multiple timepoints over several weeks, this compact design offered the advantage of only removing a single connection at a time which reduced contamination risks and clutter in the incubator. To maintain consistent flow to all four scaffolds, an axisymmetric design with smoothly interconnected channels was modeled in Solidworks (Dassault Systèmes, 2022) as shown in Figure 22A. A biocompatible and autoclavable resin was chosen from Form Labs (Surgical Guide) and used to 3D print the bioreactor body at a resolution of 100 microns as shown in the assembly image of Figure 22B. This design is herein referred to as the BR4.

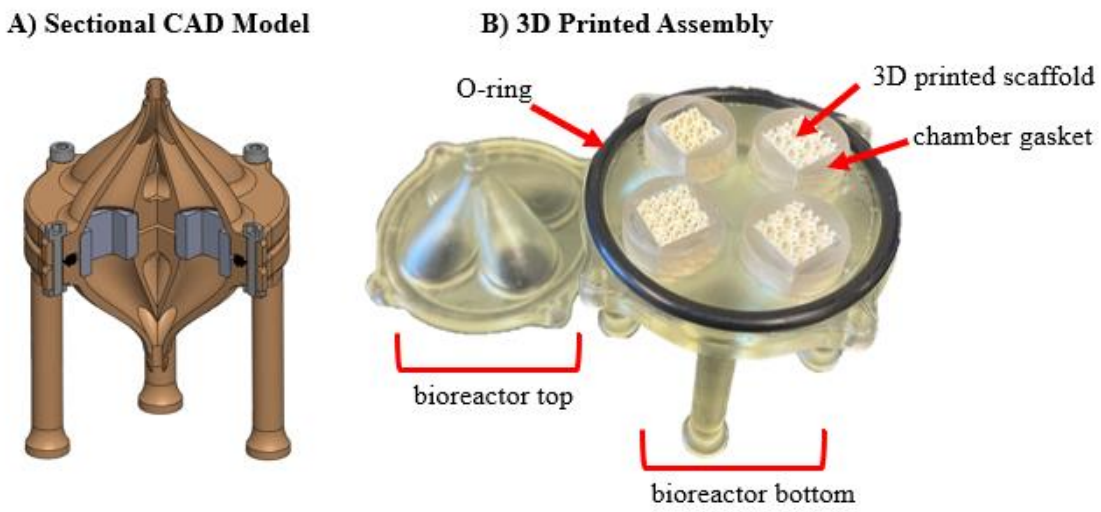

Figure 22. The axisymmetric 4-channel bioreactor design (BR4) is shown as a sectional CAD model (A) to view the interior, and an image is provided of the 3D printed assembly (B).

The design was divided into symmetric top and bottom halves to enable bi-directional flow. Four hex head bolts compressed the two halves onto an o-ring providing a face seal from the exterior. Each scaffold was placed into the elastomeric sleeve which fit tightly into a round chamber in each half. The central inlet was lofted to each chamber for a smooth transition, and the flow path circumscribed the entire rectangular scaffold face to ensure all corners were exposed to perfusion. The bottom half featured legs for easy scaffold loading and observation. The Surgical Guide resin was selected because it is biocompatible and autoclavable, which met the third and final design requirement. Additionally, the material is translucent which allowed monitoring of air bubbles and flow at the scaffold interface. Lastly, the BR4 was specifically designed with advanced mineralization studies in mind. The whole assembly can be sealed with live cells inside and fit into a micro-CT machine for tracking bone formation over time without ever handling the scaffolds.

4.2.3 Shear Stress, Flow Rate, and Velocity

It has been well demonstrated that fluid-induced shear stresses on scaffolds enhance osteoblastic activity and mineralization[16], [18], but optimal values are not well understood, and comparing values between studies is difficult due to variations in bioreactor design as described. It is generally understood that when shear stress is too low, it is insufficient to drive differentiation, and when it is too high, it can lead to cell death and detachment. Vetsch et al. in 2017 studied perfusion effects on silk fibrin scaffolds, reporting that shear stresses below 0.39 mPa only drove cell proliferation, not differentiation, and that a range of 0.55 – 24 mPa induced significant osteogenic effects[21]. Melchels et al. designed scaffolds for a nominal shear stress of around 30 mPa and reported that values greater than 1 Pa resulted in detachment[34]. Zermatten et al. reviewed a variety of perfusion studies across different scaffold materials and porosities which saw nominal shear stress values from 1 – 11 mPa[42]. Similarly, Zhao et al. reported that values below 0.11 mPa struggled to mineralize the extracellular matrix (ECM) while values greater than 60 mPa detached cells[43]. With values across several orders of magnitude in the literature, an optimal value has not emerged. Furthermore, shear stress values were not directly measured in any study, which adds further uncertainty. Studies rely heavily on correlations between CFD and *in vitro* measurements. Shear stress is clearly the critical driver of mechanotransduction, but in practice, it is a poor design variable because it cannot be directly monitored. For this reason, it is more practical to present the flow rate and scaffold inlet velocity for system designs and comparisons. Zhao et. al. studied the relationship between flow rates and shear stress on scaffolds with various geometries, pore sizes, and porosities to recommend a 10-fold range of 0.5 to 5 ml/min[43]. A recent study by Gabetti et al. showed that their range of 0.3 to 1 ml/min achieved target shear stress values and significant mineralization[44]. From this review, a nominal flow rate of 1 ml/min/scaffold with an average velocity of 0.1 mm/s entering the scaffold was selected for

this study. The resulting velocity distribution inside the BR4 chambers at this flow rate was then examined through simulations.

4.2.4 CFD

The homogeneity and magnitude of the velocity distribution, as well as the effects of scaffold permeability, were studied through CFD using ANSYS Fluent (ANSYS Inc., Canonsburg, PA. Flow rate directly determines the mass transport to the cells, but the bioreactor and scaffold geometry determine the flow characteristics. The BR4, along with all cited works herein, feature an expansion from the inlet to the scaffold cross section. Given incompressible fluid under continuity, the fluid velocity at the scaffold face will be slower than that of the inlet, and it is critical that its magnitude is reported for reproducibility. Calculations were performed within a quarter model representing a single fluid channel of the BR4. A final convergent mesh (~250,000 elements and ~100,000 nodes) with tetrahedral elements for the main body and prismatic elements for the scaffold was generated to represent the symmetrical fluid domain as shown in figure 23. A laminar, incompressible flow of water at 37°C was simulated at the inlet with a velocity of 2.104 mm/s to match the designed steady flow rate of 1 ml/min to a single scaffold. A no-slip condition was applied to the walls of the fluid domain, and the outlet boundary was fixed to atmospheric pressure. Scaffold geometry was not directly modeled due to the high computational expense, and the simulation of internal velocities and shear stresses was outside the scope of this report[42]. Instead, the scaffold was modeled as a porous zone with a permeability that was measured experimentally. The upstream velocity profile was simulated. The porous zone was modeled with a viscous resistance of 1.27e9 m^2 which represented the inverse of the average Darcian permeability determined from experimental testing. Quadratic loss coefficients and inertial resistances were not considered due to the highly laminar Darcian regime assumed by a Reynold's number of less than one[45]. This simplification of scaffold permeability enabled an iterative

analysis of permeability effects. After simulating the average permeability of our photocast gyroid scaffolds, the results were compared to scaffolds at the low end (1e-9 m^2) and high end (2.5e-9 m^2) of all tested scaffolds to view effects on the velocity profile. The resultant velocity profiles were determined in ANSYS which used a finite volume method to solve the 3D Navier-Stokes equations.

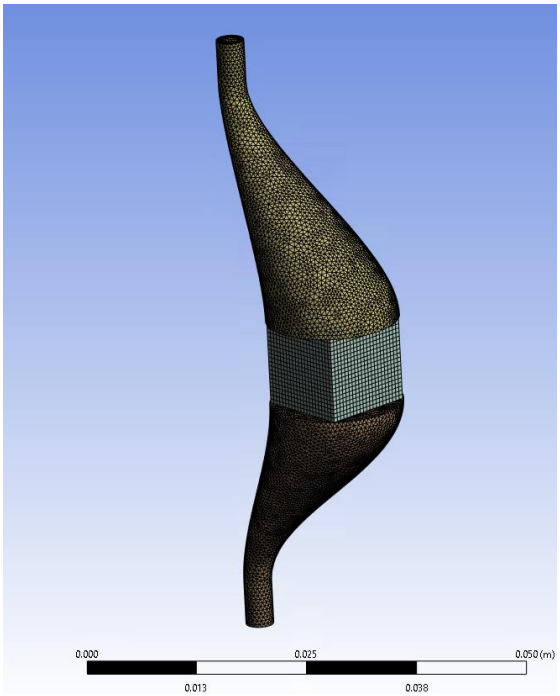

Figure 23. Final mesh of a single channel of the BR4 in ANSYS with ~250,000 elements and ~100,000 nodes.

4.3.5 Pump Selection

To deliver the desired flow rate, a non-pulsatile pump was used to limit fluctuations. Peristaltic pumps are essential for maintaining a sterile environment because they do not contact the fluid and operate within a closed system. Peristaltic pumps start as low as $10, such as those by Kamoer (Shanghai, China), but these simple DC pumps did not provide direct flow rate controls. The next price point was around $85 for dosing level pumps, such as those by Atlas Scientific (Long Island City, NY), which offered precise volume dispensing. However, they were

highly pulsatile (2-10 rpm) for flow rates in the range of 1 ml/min. For added complexity, perfusion studies operate in mammalian cell growth conditions, such as in relatively high temperature (37°C) and relative humidity (90%), which may affect the reliability of pumps. An ideal pump would operate in these conditions, provide precise flow rates, and feature low pulsation (>30 rpm). These requirements drove the price range to $2000 – 6000. Higher prices are generally associated with running more independent fluid channels, which emphasizes the need for a multi-channel bioreactor design. In this study, a Master Flex (Waltham, Massachusetts) two-channel peristaltic pump was selected for its low cost while meeting the design criteria.

4.2.6 Cell Culture and Seeding

NOTE: this work was performed by my colleagues in the lab. MC3T3-E1 cells (ATCC, USA) were precultured in preparation for cell seeding. The cells were plated in T-75cm^3 culture flasks (Nunc EasyFlask, Thermo Scientific, USA). Cells were cultured in HyClone MEM-α Modification medium (Cytiva Life Sciences, USA), supplemented with 10% fetal bovine serum and 1% penicillin/streptomycin (Gibco Life Technologies, USA). Cells were incubated in a 90% humified atmosphere, at 37°C and 5% CO_2. The medium was changed every 48-hours until the cells reached 80-90% confluency, at which point they were sub-passaged.

After achieving passage 3, the cells were detached from the culture flasks with 1X TrypLE Express Enzyme solution (Gibco Life Technologies, USA). Cell pellets were isolated and resuspended in fresh medium then stained using a 0.4% Trypan Blue solution and counted with a hematocytometer. Prior to cell seeding, 1cm^3 β-TCP scaffolds (n=4 per bioreactor) were sterilized in an autoclave on a standard gravity cycle at 121°C for 30-minutes. On seeding day, sterilized scaffolds were pre-wetted in 3mL of complete culture medium for 15-minutes, followed by aspiration, to promote cell adhesion. After pre-wetting, cells were seeded onto scaffolds at a concentration of 10,000 cells/cm3 (cells/scaffold). To achieve this, cells were resuspended in fresh

medium after centrifugation and isolation of cell pellet. Scaffolds were plated in a 24-well plate and a volume of 6uL was pipetted onto the "top" and "bottom" face of the 1cm^3 scaffolds (12uL total at a concentration of 10,000 cells/scaffold). Seeded scaffolds were then pre-incubated for 30-minutes followed by the addition of 1.8mL of culture medium per well. Scaffolds were then statically incubated for 3 days to allow for cell attachment. After a 3-day attachment period, seeded scaffolds were transferred to the bioreactors as day 0 of the experiment. The bioreactor system then ran for 7 days under perfusion until the scaffolds were extracted for analysis. A static bioreactor with no perfusion served as a control. This static bioreactor was filled with 30ml of media which was replaced on day 3. Three scaffolds chosen at random from each BR4 were used for osteogenic differentiation and cell proliferation assays described in the following. The fourth sample was fixed for imaging by scanning electron microscopy (SEM). The perfusion experiment was replicated for three independent trials of the BR4 design to test repeatability. In addition to the bioreactor experiments, six samples were assayed after seeding on day 0 to establish a baseline before entering the bioreactors.

4.2.7 Osteogenic Differentiation – ALP Activity

Alkaline phosphatase (ALP) activity was evaluated with the QuantiChrom Alkaline Phosphatase Assay Kit (DALP-250, BioAssay Systems, USA) to quantify early osteogenic differentiation and activity. After 7 days of perfusion culture, the system was stopped, and the bioreactors were removed from the incubator. The medium was purged from the bioreactor chamber and each scaffold was transferred to a 50mL centrifuge tube. The cell-laden scaffolds were submerged and lysed in 0.2% v/v Triton-X100 solution for 20 minutes in an ultrasonic bath. Intracellular ALP activity was measured according to the manufacturer's instructions. Briefly, a buffered working solution with p-nitrophenyl phosphate substrate was prepared so that 150uL was added to each well followed by the addition of 50uL sample lysate, in a 96-well plate. Four

replicates were performed for each scaffold sample. The well plates were incubated for 8-minutes in a humidified atmosphere, at 37°C and 5% CO2. Absorbance values were measured at 0 minutes and 8 minutes at a wavelength of 405nm in a microplate spectrophotometer. Final ALP activity was volume corrected to obtain the total ALP for the total lysate volume and normalized to total protein concentration to scale the effects by an approximation of the number of cells.

4.2.8 Total Protein Concentration – BCA Concentration

The bicinchoninic acid (BCA) assay method was used to quantify the total protein concentration via colorimetric detection with a Micro-BCA Protein Assay Kit. A standard curve was prepared, with three replicates, according to the manufacturer's instructions. Medium was purged from the bioreactor chamber and each scaffold was transferred to a 50mL centrifuge tube. The cell-laden scaffolds were lysed in 0.2% v/v Triton-X100 solution for 20 minutes in an ultrasonic bath. Working solution was prepared according to the manufacturer's instructions. Briefly, 150uL of buffered working solution was added to 150uL of sample lysate in a 96-well plate and incubated for 2 hours in a humidified atmosphere, at 37°C and 5% CO_2. Four replicates were prepared for each scaffold sample. After incubation, absorbance values were measured at a wavelength of 562nm in a microplate spectrophotometer. Total protein content was corrected to the lysate volume used for each sample.

4.2.9 Cell Morphology

Cell morphology on the scaffold exterior was evaluated using SEM. One scaffold was removed from each BR4 after 7 days of perfusion culture for imaging. The cell-laden scaffolds were fixed for 1-hour with 2% paraformaldehyde and 2.5% glutaraldehyde in a 0.1M sodium phosphate buffer (Karnovsky's Fixative Kit, Electron Microscopy Sciences, Fisher Scientific, USA). After fixation, the discs were washed with Phosphate-Buffered Saline (PBS, Fisher Bioreagents, USA) for 2-minutes and rinsed with sterile deionized water for 2-minutes. The PBS

wash and water rinse steps were repeated twice. The scaffolds were dehydrated using a standard graded ethanol series and stored in a vacuum desiccator until imaging. The scaffolds were sputter coated with 10nm of gold and SEM imaged at an accelerating voltage of 5 KeV, working distance of 10mm, and four different magnifications (x50, x500, x1000, and x2000).

4.2.10 System Layout and Workflow

The bioreactors, media reservoirs, stir plate, peristaltic pump, tubes, and dissolved oxygen probes were sterilized with Conflikt quaternary detergent disinfectant and 70% ethanol for 20 minutes and then assembled inside the incubator to create two independent flow loops as shown in Figures 24 and 25. Clear Tygon® tubing with an inner diameter of 3mm was cut to equal lengths in each flow loop to join the components with barbed quick-turn connectors. The loop begins with a tube end submerged in the 500ml media flask herein referred to as the reservoir. The reservoir, resting on the stir plate set to low speed, contains 150ml of media, a 2cm stir bar, and a dissolved oxygen probe. A gas permeable cap atop the reservoir blocks contaminants and holds the inlet tube and dissolved oxygen probe sufficiently below the media surface and away from the stir rod. Fluid is drawn from the reservoir through the pump and bioreactors before returning to the reservoir. The inlet and outlet tubes are both submerged in the media to permit bi-directional flow.

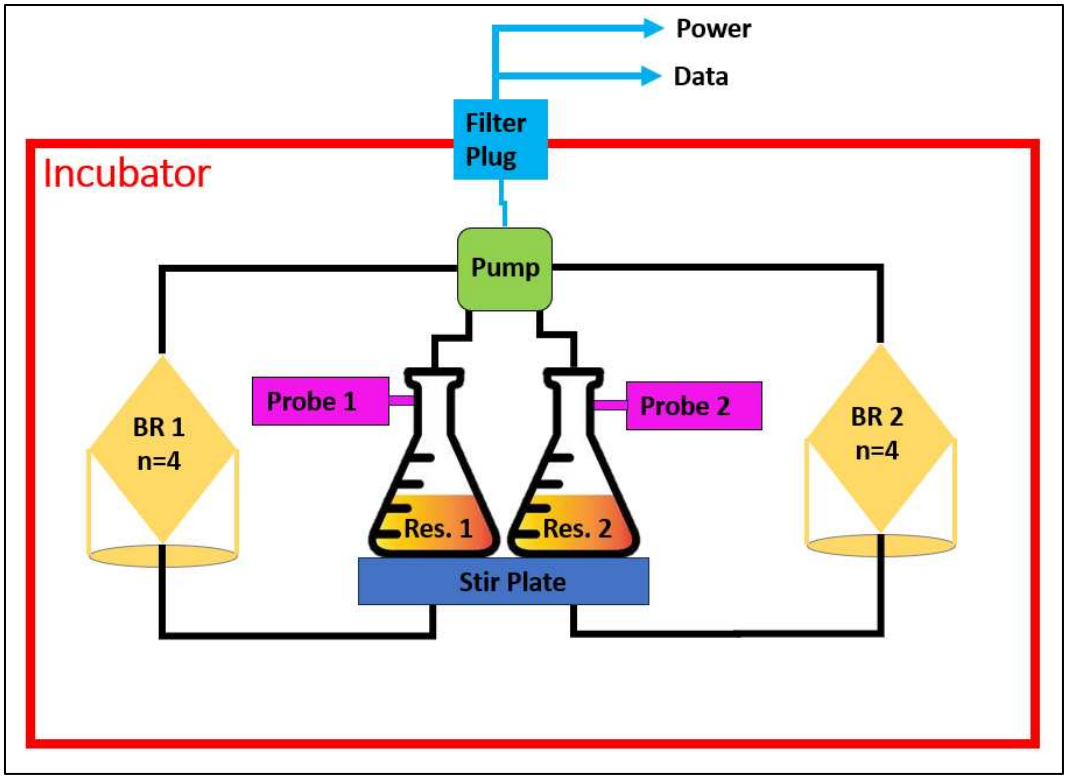

Figure 24. A schematic of the bioreactor system is shown for two independent flow loops inside an incubator. In each loop, cell media is drawn from the reservoir (Res.) through the peristaltic pump, which then passes through the bioreactor (BR) and back to the reservoir. A probe submerged in the reservoir measures dissolved oxygen concentrations. The reservoir sits on a stir plate which continuously mixes the media. A plug with a filter allows for data and power to be transferred externally without contaminating the incubator.

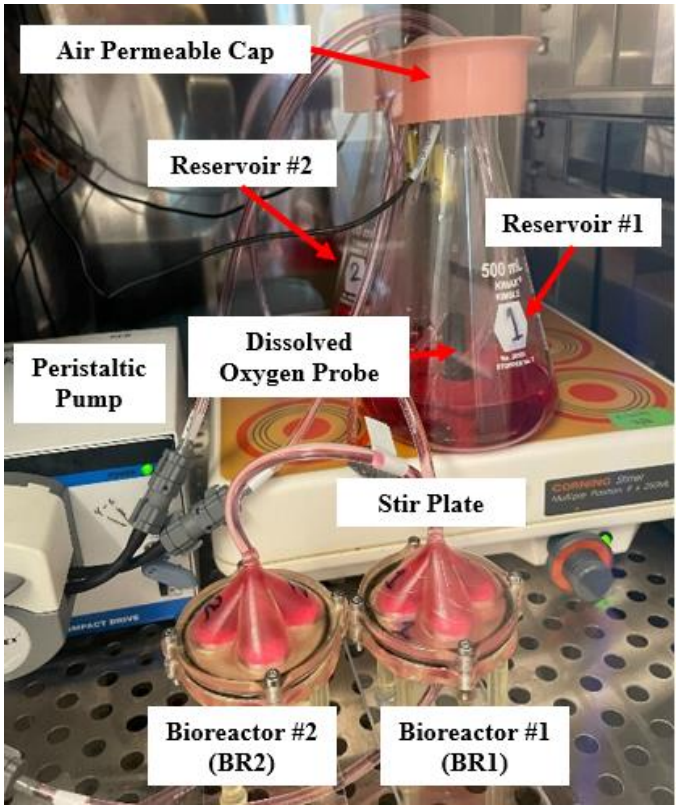

Figure 25. An image of the two-loop bioreactor system is shown with essential components labeled.

Operation of the pump, stir plate, and dissolved oxygen sensors inside the incubator required the design of a custom incubator plug as shown in Figure 26. The power and data cords were connected externally. The incubator plug was 3D printed in Elastic 50A resin from Form Labs to fit the four cords radially around the hole designed for a HEPA filter. This plug maintained a sterile environment while permitting continuous operation and data monitoring.

Figure 26. The custom incubator plug is installed into the access hole from the inside of the incubator. The four cords are sealed around the perimeter of the filter hole (filter not shown).

Once the system was set up, seeded scaffolds were loaded into chamber gaskets and sealed inside each BR4 in a biosafety cabinet. Quick-turn connectors with self-sealing tips attached to the top and bottom of each bioreactor allowed for sterile transport between the biosafety cabinet and the incubator. Once the BR4 was connected to the flow loop, the pump was set to the prescribed flow rate to begin filling the bioreactor from top to bottom to push out any air bubbles. After a few minutes, some air bubbles may become trapped on the upstream side of the scaffolds because the low flow rate did not provide enough force to push them through the pores. In these situations, the flow was reversed at the same speed and after a few minutes no air bubbles were found anywhere in the system. With the system primed, the flow was again set to run top to bottom through the bioreactors for the duration of the study. The system was checked daily for leaks, air bubbles, and flow to confirm the system was operating as expected. Quick connectors placed throughout the system enabled quick changes of reservoir media, which was replaced every 7 days by design, based on the total volume the flow loop. The quick connectors also permitted easy removal of the BR4 while holding media inside, enabling the BR4 to be transferred to a biosafety cabinet or a micro-CT machine for analysis without removing or exposing the scaffolds.

4.2.11 Dissolved Oxygen

Essential nutrients are provided to cells through the cell media which is circulated through scaffolds in a perfusion study. Pumps pull media from a reservoir that is exposed to incubated air to maintain cell homeostasis. Atmospheric conditions for mammalian culture are well established to mimic body temperature (37°C), prevent evaporation/dehydration (90% humidity), and buffer the pH of the culture (5% CO_2)[46]. Filtered air pulled into the incubator nominally contains 21% oxygen, but this does not represent the dissolved oxygen delivered to cells. In fact, oxygen diffusion depends on several factors including cell seeding, culture vessel, media volume, media depth, elevation, and mixing, many of which are routinely not reported[22]. Oxygenation significantly impacts cell growth, so methods and values must be presented for reproducibility. In this study, MC3T3-E1 pre-osteoblast cells were seeded at density of 10,000 cells per scaffold. Four of these scaffolds were supplied media at a constant flow rate of 1 ml/min/scaffold from a 500ml flask which contained 150ml of media, resulting in a fluid depth of ~2 cm. Flasks were covered with a permeable, non-cytoxic foam cap to keep out any debris and to hold the inlet and outlet tubes in position. Media was well mixed using a Corning multi-position stir plate. Studies were conducted in Fort Collins, Colorado at an elevation of 5,100 feet. Lastly, the resulting dissolved oxygen values were continuously monitored using an Atlas Scientific probe over each 7-day study.

4.3 Results and Discussion

The BR4 design and the bioreactor system operated as planned over the course of the experiments. The chamber gaskets fit tightly to the scaffolds without damage and facilitated handling in and out of the BR4. The BR4 sealed the media without leakage, and the quick connectors limited setup time with the incubator door open. With the addition of some silicon sealant, the incubator plug enabled a stable and sterile incubated environment without contamination through all three trials. The pump, stir plate, and dissolved oxygen probe operated

without issue and no signs of corrosion or contamination could be identified. Dissolved oxygen fluctuated in a range from 8.5 - 9.5 mg/L of oxygen for each trial, which aligned with literature values of similar mammalian cell cultures[47]. The priming step, which involved running the pump bi-directionally at the start of the study, removed air bubbles at the start of all trials. However, air bubbles reemerged on the upstream scaffold face on days 2 and 5 in trial 2. The prime step was repeated in these instances and the air bubbles were removed. Air could have re-entered the system through weak seals or disruptions to the inlet tube in the reservoir. If the inlet tube was moved during the daily system check, it could have pulled air into the system. These issues could be avoided by creating a more secure method for the inlet tube position at the bottom of the reservoir and by tightening all seals to a defined specification. The multi-channel design is more vulnerable to air bubbles than a single channel design but it is not a problem. Air in the system encounters resistance at the upstream scaffold face because the surface tension of the bubbles must be broken to force it through the pores of the scaffold. In a multi-channel setup at these relatively low flow rates, pressure could not build to force air bubbles through the scaffold because the remaining channels devoid of air offered a path of lower resistance. Increasing the flow rate would push the air bubbles through the scaffold in benchtop testing, but this could not be used in practice because the fluid induced shear stresses would be increased outside of designed values. Temporarily reversing the flow for a fixed period allowed for air bubbles to exit the system without forcing them through the scaffolds, and shear stresses were controlled and consistent between all bioreactors by following a defined procedure. The system operation behaved mostly as expected, but further investigation into eliminating air from the system is required to ensure that each channel of the BR4 receives more precisely the same mass transport and mechanical stimulation.

Fluid simulations revealed the velocity profile delivered to the scaffolds based on the BR4 geometry and enabled testing the effects of scaffold permeability. Not only is the flow rate critical to report for bioreactor study reproducibility, but the velocity profile is important as well because it is affected by bioreactor geometry. Given our symmetric reduction of the BR4 domain to a single channel, CFD predicted that an inlet flow rate of 1 ml/min would result in the velocity profile shown in Figure 27.

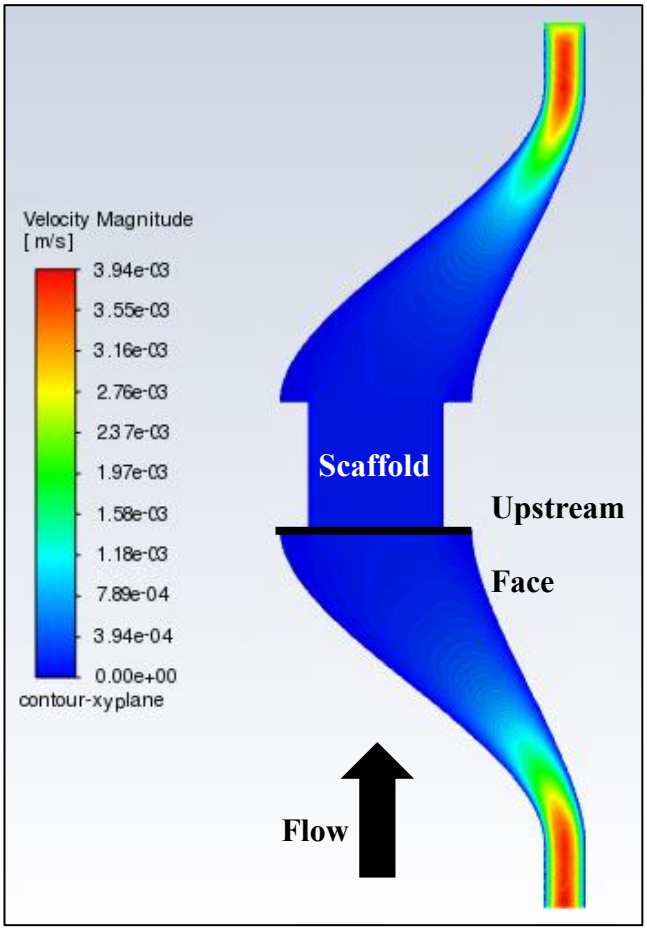

Figure 27. Velocity contour plot on the central cross section of a channel in the BR4.

The velocity contours shown on the central cross section in Figure 27 reveal a relative heatmap where the fastest velocities (shown in red) occur at the inlet and decrease by an order of

magnitude (shown in blue) by the time they hit the upstream face of the scaffold. No velocity is shown inside the scaffold because it was modeled as a black box with a given flow resistance as discussed earlier. These results indicate that reporting the inlet velocity is insufficent for reproducibility because the flow entering the scaffolds at the upstream face decreases significantly due to continuity laws at steady state. The velocity contours at the upstream scaffold face are shown in Figure 28 with local magnitude scaling.

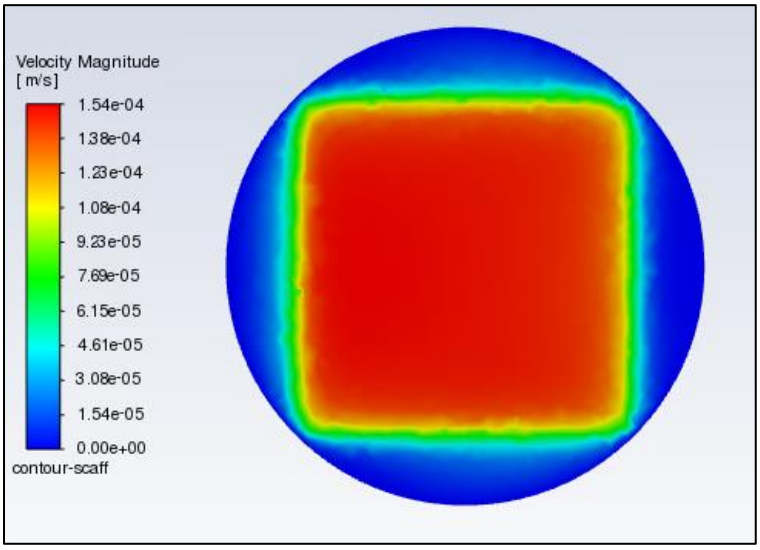

Figure 28. Velocity contour plot of the upstream scaffold face in the BR4 with local magnitude scaling.

CFD analysis at the upstream scaffold face predicts that the entrance flow rate of 1 ml/min will result in an average velocity of 0.154 mm/s entering the cubic scaffold. Some boundary effects of slower velocities can be observed in green at the scaffold perimeter, but these regions are unavoidable given a no-slip boundary condition. Overall, the flow hitting the scaffold face was uniform and laminar as intended for perfusion studies.

In these simulations, symmetry was a valid assumuption to reduce the fluid domain of the BR4 to a single channel because the resolution of the surgical guide material on the Form 3B+ printer was relatively high, with a layer thickness of 50 microns. Internal channels of the BR4 had no visible defects, and channels were smoothly printed and connected. However, the robocast ceramic scaffolds used in this study have much poorer resolution leading to differences in permeability which can range from 1 – 2.5e-9 m^2 . Variations in permeability between scaffolds in the BR4 could change the distibution of flow and therefore the velocity magnitude at the upstream scaffold face. To test this, the simulation was replicated with permeabilities at the low and high end of the stated range to compare with the results from the average value of 1.37e-9 m^2. Results showed less than a 0.06% difference in the average velocity at the upstream scaffold face when the worst case permeability was applied. This indicates that the effect on velocity of manufacturing variations in permeability are likely insignificant. In this simulation, the permeability had to be increased by an order of magnitude to create even a 2.6% difference in the upstream scaffold velocity. These results indicate that when using a multi-channel design, sample groups should be organized into different bioreactors to ensure consistent flows. In summation, CFD simulations predicted that the BR4 would deliver consistent flow to each of its channels which is essential in validating a multi-channel design.

After 7 days of perfusion culture, cell assays were collected to validate the bioreactor system design to determine if the design parameters induced significant osteogenic effects when compared to static controls, if the results were consistent between channels of the BR4, and if the outcomes were repeatable between experiments. Sample groups were organized in their respective bioreactors to ensure consistentcy. ALP concentration is a widely recognized biochemical marker

for osteoblast activity which measured the osteogenic effects of the experiment as shown in Figure 29.

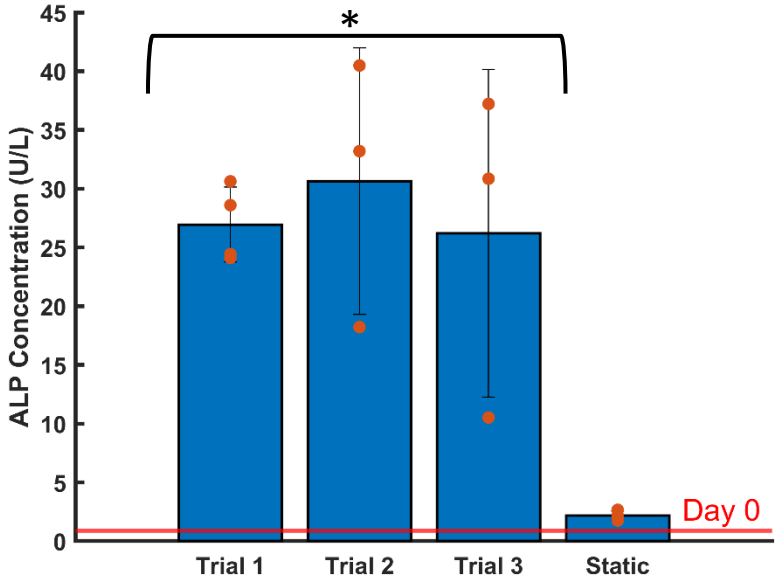

Figure 29. Osteogenic activity after 7 days perfused. Average values are shown as bars with standard deviation error bars. Individual data points for each experiment (n=3) are displayed as orange dots. Statistical significance to the static control denoted by: (*, P < 0.05), (**, P < 0.01), (***, P < 0.001).

All three replicates of the perfusion study showed significantly higher expression of ALP than the static control which indicates that the system can reliably induce an osteogenic environment. No significant differences (P<.05) could be found between any of the three trials which implied the results were repeatable. The total protein concentration was analyzed for each scaffold in the system to quantify the cell activity across each trial as shown in Figure 30 and to correct ALP results for cell population. Results indicated that trials 1 and 3 both had significantly lower protein concentrations than the static control which corresponds to reduced proliferation. Moreover, all three trials produced an average protein concentration that was lower than that of day 0 when they entered the bioreactors. No significant conclusion could be drawn for trial 2 due to the high variation. This variation was likely caused by the appearance of air bubbles observed

on days 2 and 5 of trial 2. Air bubbles trapped at the upstream scaffold face may have created a resistance in nutrient delivery to the two samples that expressed lower protein content. The high outlier in trial 2 may have experienced increased nutrient delivery due to this increased resistance on other channels.

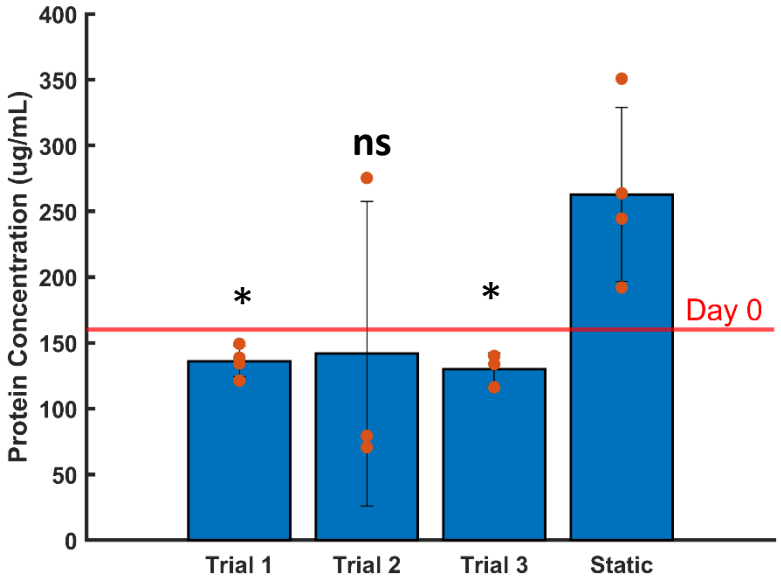

Figure 30. Total cell protein concentration after 7 days perfused. Average values are shown as bars with standard deviation error bars. Individual data points for each experiment are displayed as orange dots. Statistical significance to the static control denoted by: (*, $P < 0.05$), (**, $P < 0.01$), (***, $P < 0.001$), or (ns, no significance).

Lastly, ALP activity was normalized by the total protein concentration in Figure 31 to draw conclusions on cell fate in the bioreactor system. These outcomes support the idea that cells focus on a single task at a time based on their environment, in this case, cells either proliferated or differentiated[48]. Cells in static culture produced little ALP but saw large increases in total protein which implies they were proliferating in the absence of mechanical cues. On the other hand, all trials under perfusion demonstrated high levels of ALP expression and a lower total protein which implies that cellular activity was biased towards osteoblastic differentiation and subsequent

mineralization by fluid induced shear stresses. Decreases in total protein among the perfused samples were likely caused by insufficient cell attachments during the 3-day seeding process which may have been lost when transferring to the bioreactor.

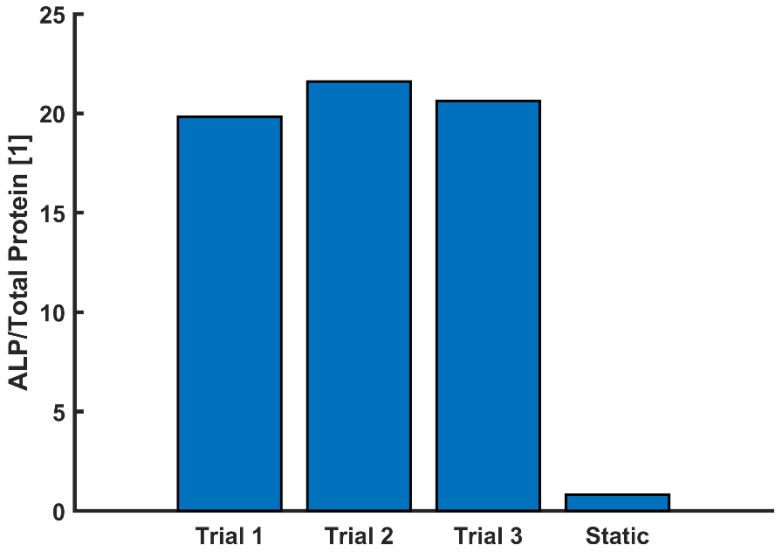

Figure 31. Osteogenic activity normalized by total protein concentration after 7 days of perfusion.

To further investigate cell growth in the BR4, one scaffold from each trial was imaged using SEM as shown in figure 32. This characteristic image of the scaffold exterior shows cell morphologies indicative of mature osteoblasts. Cells were abundant, intact and healthy in appearance, with relatively uniform distributions.

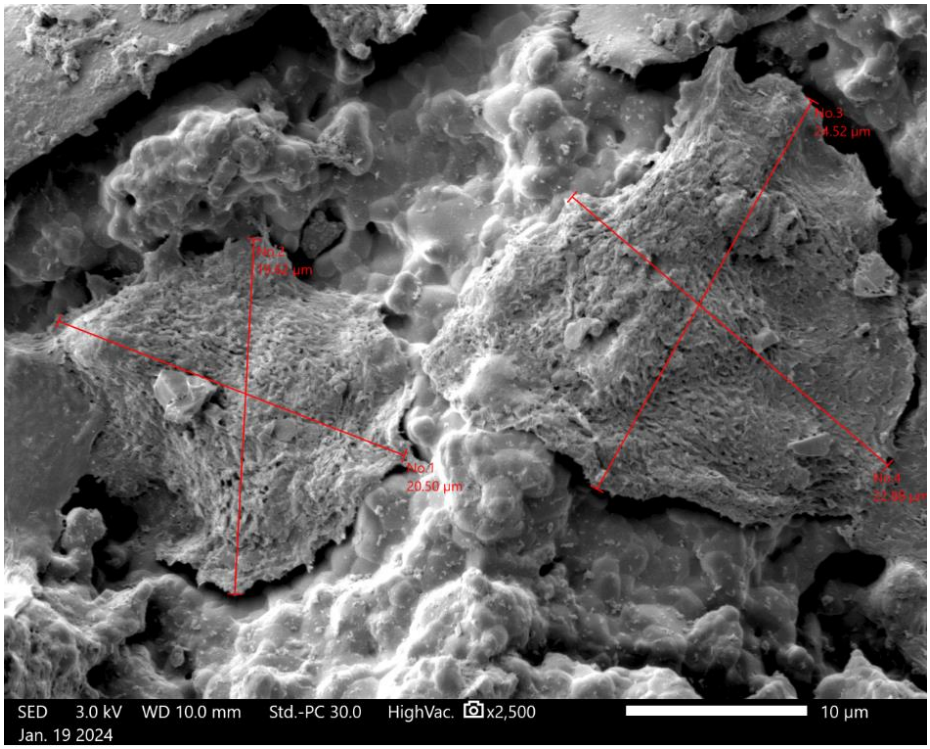

Figure 32. Osteoblasts, marked by red Xs, are shown on the scaffold surface using SEM.

4.4 Conclusion

This study demonstrates that the BR4 bioreactor and system is capable of repeatably culturing highly porous ceramic 3D scaffolds towards osteogenic differentiation. Methods development for this system emphasized that more parameters must be reported if perfusion bioreactor studies are to be comparable and reproducible. CFD and cell assay results validated the BR4 design which creates opportunity for the adoption of more multi-channel bioreactors in future studies. In this study, the inherent variability of *in vitro* cell studies were apparent, and future work will include more replicates of this study using peristaltic pumps with more fluid channels. Future work will also feature staining methods to quantify the distribution of cells on the scaffold interior which can be challenging to do in a non-destructive manner. A consistent bioreactor capable of

handling large sample volumes is essential in characterizing the cell behavior on scaffolds with greater certainty for bone tissue engineering.

References

[1] J. Henkel *et al.*, "Bone Regeneration Based on Tissue Engineering Conceptions — A 21st Century Perspective," *Bone Res.*, vol. 1, no. 3, pp. 216–248, Sep. 2013, doi: 10.4248/BR201303002.

[2] L. Vidal, C. Kampleitner, M. Á. Brennan, A. Hoornaert, and P. Layrolle, "Reconstruction of Large Skeletal Defects: Current Clinical Therapeutic Strategies and Future Directions Using 3D Printing," *Front. Bioeng. Biotechnol.*, vol. 8, p. 61, Feb. 2020, doi: 10.3389/fbioe.2020.00061.

[3] S. Bose, S. Vahabzadeh, and A. Bandyopadhyay, "Bone tissue engineering using 3D printing," *Materials Today*, vol. 16, no. 12, pp. 496–504, Dec. 2013, doi: 10.1016/j.mattod.2013.11.017.

[4] S. H. Jariwala, G. S. Lewis, Z. J. Bushman, J. H. Adair, and H. J. Donahue, "3D Printing of Personalized Artificial Bone Scaffolds," *3D Printing and Additive Manufacturing*, vol. 2, no. 2, pp. 56–64, Jun. 2015, doi: 10.1089/3dp.2015.0001.

[5] T. D. Ngo, A. Kashani, G. Imbalzano, K. T. Q. Nguyen, and D. Hui, "Additive manufacturing (3D printing): A review of materials, methods, applications and challenges," *Composites Part B: Engineering*, vol. 143, pp. 172–196, Jun. 2018, doi: 10.1016/j.compositesb.2018.02.012.

[6] L. Yuan, S. Ding, and C. Wen, "Additive manufacturing technology for porous metal implant applications and triple minimal surface structures: A review," *Bioactive Materials*, vol. 4, no. 1, pp. 56–70, Mar. 2019, doi: 10.1016/j.bioactmat.2018.12.003.

[7] A. Bigham, F. Foroughi, E. Rezvani Ghomi, M. Rafienia, R. E. Neisiany, and S. Ramakrishna, "The journey of multifunctional bone scaffolds fabricated from traditional toward modern techniques," *Bio-des. Manuf.*, vol. 3, no. 4, pp. 281–306, Dec. 2020, doi: 10.1007/s42242-020-00094-4.

[8] G. Turnbull *et al.*, "3D bioactive composite scaffolds for bone tissue engineering," *Bioactive Materials*, vol. 3, no. 3, pp. 278–314, Sep. 2018, doi: 10.1016/j.bioactmat.2017.10.001.

[9] J. An, J. E. M. Teoh, R. Suntornnond, and C. K. Chua, "Design and 3D Printing of Scaffolds and Tissues," *Engineering*, vol. 1, no. 2, Art. no. 2, Jun. 2015, doi: 10.15302/J-ENG-2015061.

[10] G. N. Bancroft, V. I. Sikavitsas, and A. G. Mikos, "Technical Note: Design of a Flow Perfusion Bioreactor System for Bone Tissue-Engineering Applications," *Tissue Engineering*, vol. 9, no. 3, pp. 549–554, Jun. 2003, doi: 10.1089/107632703322066723.

[11] B. David *et al.*, "A Perfusion Bioreactor for Engineering Bone Constructs: An *In Vitro* and *In Vivo* Study," *Tissue Engineering Part C: Methods*, vol. 17, no. 5, pp. 505–516, May 2011, doi: 10.1089/ten.tec.2010.0468.

[12] F. W. Janssen, J. Oostra, A. van Oorschot, and C. A. van Blitterswijk, "A perfusion bioreactor system capable of producing clinically relevant volumes of tissue-engineered bone: In vivo bone formation showing proof of concept," *Biomaterials*, vol. 27, no. 3, pp. 315–323, Jan. 2006, doi: 10.1016/j.biomaterials.2005.07.044.

[13] J. Rauh, F. Milan, K.-P. Günther, and M. Stiehler, "Bioreactor Systems for Bone Tissue Engineering," *Tissue Engineering Part B: Reviews*, vol. 17, no. 4, pp. 263–280, Aug. 2011, doi: 10.1089/ten.teb.2010.0612.

[14] A. Ravichandran, Y. Liu, and S.-H. Teoh, "Review: bioreactor design towards generation of relevant engineered tissues: focus on clinical translation," *Journal of Tissue Engineering and Regenerative Medicine*, vol. 12, no. 1, pp. e7–e22, 2018, doi: 10.1002/term.2270.

[15] D. A. Gaspar, V. Gomide, and F. J. Monteiro, "The role of perfusion bioreactors in bone tissue engineering," *Biomatter*, vol. 2, no. 4, pp. 167–175, Oct. 2012, doi: 10.4161/biom.22170.

[16] A. B. Yeatts and J. P. Fisher, "Bone tissue engineering bioreactors: Dynamic culture and the influence of shear stress," *Bone*, vol. 48, no. 2, pp. 171–181, Feb. 2011, doi: 10.1016/j.bone.2010.09.138.

[17] Castro, Pires, Santos, Gouveia, and Fernandes, "Permeability versus Design in TPMS Scaffolds," *Materials*, vol. 12, no. 8, p. 1313, Apr. 2019, doi: 10.3390/ma12081313.

[18] L. F. Bonewald, "Mechanosensation and Transduction in Osteocytes," *Bonekey Osteovision*, vol. 3, no. 10, pp. 7–15, Oct. 2006, doi: 10.1138/20060233.

[19] M. R. Dias, P. R. Fernandes, J. M. Guedes, and S. J. Hollister, "Permeability analysis of scaffolds for bone tissue engineering," *Journal of Biomechanics*, vol. 45, no. 6, pp. 938–944, Apr. 2012, doi: 10.1016/j.jbiomech.2012.01.019.

[20] D. Ali, M. Ozalp, S. B. G. Blanquer, and S. Onel, "Permeability and fluid flow-induced wall shear stress in bone scaffolds with TPMS and lattice architectures: A CFD analysis," *European Journal of Mechanics - B/Fluids*, vol. 79, pp. 376–385, Jan. 2020, doi: 10.1016/j.euromechflu.2019.09.015.

[21] J. R. Vetsch, D. C. Betts, R. Müller, and S. Hofmann, "Flow velocity-driven differentiation of human mesenchymal stromal cells in silk fibroin scaffolds: A combined experimental and computational approach," *PLoS One*, vol. 12, no. 7, p. e0180781, 2017, doi: 10.1371/journal.pone.0180781.

[22] A. Al-Ani, D. Toms, D. Kondro, J. Thundathil, Y. Yu, and M. Ungrin, "Oxygenation in cell culture: Critical parameters for reproducibility are routinely not reported," *PLoS One*, vol. 13, no. 10, p. e0204269, Oct. 2018, doi: 10.1371/journal.pone.0204269.

[23] J. Schmid *et al.*, "A Perfusion Bioreactor System for Cell Seeding and Oxygen-Controlled Cultivation of Three-Dimensional Cell Cultures," *Tissue Engineering Part C: Methods*, vol. 24, no. 10, pp. 585–595, Oct. 2018, doi: 10.1089/ten.tec.2018.0204.

[24] F. Liu, Z. Mao, P. Zhang, D. Z. Zhang, J. Jiang, and Z. Ma, "Functionally graded porous scaffolds in multiple patterns: New design method, physical and mechanical properties," *Materials & Design*, vol. 160, pp. 849–860, Dec. 2018, doi: 10.1016/j.matdes.2018.09.053.

[25] D. W. Abueidda, M. Elhebeary, C.-S. (Andrew) Shiang, S. Pang, R. K. Abu Al-Rub, and I. M. Jasiuk, "Mechanical properties of 3D printed polymeric Gyroid cellular structures: Experimental and finite element study," *Materials & Design*, vol. 165, p. 107597, Mar. 2019, doi: 10.1016/j.matdes.2019.107597.

[26] S. Bose, D. Ke, H. Sahasrabudhe, and A. Bandyopadhyay, “Additive manufacturing of biomaterials,” *Progress in Materials Science*, vol. 93, pp. 45–111, Apr. 2018, doi: 10.1016/j.pmatsci.2017.08.003.

[27] B. C. Gross, J. L. Erkal, S. Y. Lockwood, C. Chen, and D. M. Spence, “Evaluation of 3D Printing and Its Potential Impact on Biotechnology and the Chemical Sciences,” *Anal. Chem.*, vol. 86, no. 7, pp. 3240–3253, Apr. 2014, doi: 10.1021/ac403397r.

[28] J. Henkel *et al.*, “Scaffold-guided bone regeneration in large volume tibial segmental defects,” *Bone*, vol. 153, p. 116163, Dec. 2021, doi: 10.1016/j.bone.2021.116163.

[29] S. K. Nandi, G. Fielding, D. Banerjee, A. Bandyopadhyay, and S. Bose, “3D-printed β-TCP bone tissue engineering scaffolds: Effects of chemistry on in vivo biological properties in a rabbit tibia model,” *Journal of Materials Research*, vol. 33, no. 14, pp. 1939–1947, Jul. 2018, doi: 10.1557/jmr.2018.233.

[30] V. Karageorgiou and D. Kaplan, “Porosity of 3D biomaterial scaffolds and osteogenesis,” *Biomaterials*, vol. 26, no. 27, pp. 5474–5491, Sep. 2005, doi: 10.1016/j.biomaterials.2005.02.002.

[31] S. Sturm, S. Zhou, Y.-W. Mai, and Q. Li, “On stiffness of scaffolds for bone tissue engineering—a numerical study,” *Journal of Biomechanics*, vol. 43, no. 9, pp. 1738–1744, Jun. 2010, doi: 10.1016/j.jbiomech.2010.02.020.

[32] A. A. Zadpoor, “Bone tissue regeneration: the role of scaffold geometry,” *Biomater. Sci.*, vol. 3, no. 2, pp. 231–245, 2015, doi: 10.1039/C4BM00291A.

[33] H. Montazerian, E. Davoodi, M. Asadi-Eydivand, J. Kadkhodapour, and M. Solati-Hashjin, “Porous scaffold internal architecture design based on minimal surfaces: A compromise between permeability and elastic properties,” *Materials & Design*, vol. 126, pp. 98–114, Jul. 2017, doi: 10.1016/j.matdes.2017.04.009.

[34] F. P. W. Melchels, A. M. C. Barradas, C. A. van Blitterswijk, J. de Boer, J. Feijen, and D. W. Grijpma, “Effects of the architecture of tissue engineering scaffolds on cell seeding and culturing,” *Acta Biomaterialia*, vol. 6, no. 11, pp. 4208–4217, Nov. 2010, doi: 10.1016/j.actbio.2010.06.012.

[35] F. P. W. Melchels *et al.*, “The influence of the scaffold design on the distribution of adhering cells after perfusion cell seeding,” *Biomaterials*, vol. 32, no. 11, pp. 2878–2884, Apr. 2011, doi: 10.1016/j.biomaterials.2011.01.023.

[36] F. M. Klenke, Y. Liu, H. Yuan, E. B. Hunziker, K. A. Siebenrock, and W. Hofstetter, “Impact of pore size on the vascularization and osseointegration of ceramic bone substitutesin vivo,” *J. Biomed. Mater. Res.*, vol. 85A, no. 3, pp. 777–786, Jun. 2008, doi: 10.1002/jbm.a.31559.

[37] L. Rincón-Kohli and P. K. Zysset, “Multi-axial mechanical properties of human trabecular bone,” *Biomech Model Mechanobiol*, vol. 8, no. 3, pp. 195–208, Jun. 2009, doi: 10.1007/s10237-008-0128-z.

[38] N. Isaacson *et al.*, “Compressive properties and failure behavior of photocast hydroxyapatite gyroid scaffolds vary with porosity,” *J Biomater Appl*, p. 088532822110739, Mar. 2022, doi: 10.1177/08853282211073904.

[39] V. Baumer, E. Gunn, V. Riegle, C. Bailey, C. Shonkwiler, and D. Prawel, "Robocasting of Ceramic Fischer–Koch S Scaffolds for Bone Tissue Engineering," *JFB*, vol. 14, no. 5, p. 251, Apr. 2023, doi: 10.3390/jfb14050251.

[40] Houmard, M. et. al., "On the structural, mechanical, and biodegradation properties of HAβ-TCP robocast scaffolds.pdf," *J. Biomed. Mater. Res. - Part B Appl. Biomater.*, vol. 101, pp. 1233–1242, May 2013, doi: 10.1002/jbm.b.32935.

[41] A. J. Wagoner Johnson and B. A. Herschler, "A review of the mechanical behavior of CaP and CaP/polymer composites for applications in bone replacement and repair," *Acta Biomaterialia*, vol. 7, no. 1, pp. 16–30, Jan. 2011, doi: 10.1016/j.actbio.2010.07.012.

[42] E. Zermatten, J. R. Vetsch, D. Ruffoni, S. Hofmann, R. Müller, and A. Steinfeld, "Micro-computed tomography based computational fluid dynamics for the determination of shear stresses in scaffolds within a perfusion bioreactor," *Ann Biomed Eng*, vol. 42, no. 5, pp. 1085–1094, May 2014, doi: 10.1007/s10439-014-0981-0.

[43] F. Zhao, B. Van Rietbergen, K. Ito, and S. Hofmann, "Flow rates in perfusion bioreactors to maximise mineralisation in bone tissue engineering in vitro," *Journal of Biomechanics*, vol. 79, pp. 232–237, Oct. 2018, doi: 10.1016/j.jbiomech.2018.08.004.

[44] S. Gabetti *et al.*, "An automated 3D-printed perfusion bioreactor combinable with pulsed electromagnetic field stimulators for bone tissue investigations," *Sci Rep*, vol. 12, no. 1, Art. no. 1, Aug. 2022, doi: 10.1038/s41598-022-18075-1.

[45] J. Santos, T. Pires, B. P. Gouveia, A. P. G. Castro, and P. R. Fernandes, "On the permeability of TPMS scaffolds," *Journal of the Mechanical Behavior of Biomedical Materials*, vol. 110, p. 103932, Oct. 2020, doi: 10.1016/j.jmbbm.2020.103932.

[46] S. Tyagi and S. Mani, "Media and Buffer Preparation for Cell Culture," in *Animal Cell Culture: Principles and Practice*, S. Mani, M. Singh, and A. Kumar, Eds., in Techniques in Life Science and Biomedicine for the Non-Expert. , Cham: Springer International Publishing, 2023, pp. 77–88. doi: 10.1007/978-3-031-19485-6_5.

[47] A. Z. Mohammad, J. Sule Suso, and N. Forsyth, "OP42 - Precision control of dissolved oxygen in mammalian cell culture media impacts on in situ volatile generation and promotes improved mesenchymal stem cell yield accompanied by reduced transcriptional variability," *Free Radical Biology and Medicine*, vol. 86, p. S16, Sep. 2015, doi: 10.1016/j.freeradbiomed.2015.07.069.

[48] Angela Raucci, Paola Bellosta, Roberta Grassi, Claudio Basilico, Alka Mansukhani, "Osteoblast proliferation or differentiation is regulated by relative strengths of opposing signaling pathways" *Journal of Cellular Physiology*, vol. 215, p. 442-451, Oct. 2007, doi: https://doi.org/10.1002/jcp.21323

CONCLUSIONS AND FUTURE WORK

Basic research into BTE scaffolds is a small step towards the adoption of biomaterial constructs for treating large bone defects and improving patient outcomes. This report provided low-cost methods for reliably producing innovative scaffolds using TPMS and bioactive ceramics to accelerate translation studies. Photocasting proved to have sufficient resolution, accuracy, and precision for mimicking bone structure, and despite some manufacturing defects, performance could be tuned to match the low range of trabecular bone. Results demonstrated that FKS were 32% stronger and only 11% less permeable than Gyroids. This emphasized the unexplored potential for FKS as scaffold structure and challenged the ubiquitous use of the Gyroid. Moreover, key insights were provided into the design and benchtop characterization of scaffold structure to predict *in vivo* performance when supported by metal fixation. Lastly, a multi-channel perfusion bioreactor system was designed to overcome some limitations of current designs and emphasize parameters for repeatability and reproducibility. These chapters have been published, or are in the process of publication, to contribute this knowledge to the BTE community for the benefit of all researchers. In summation, this report demonstrates our work in design, fabrication, and characterization of scaffolds to improve performance.

Future work in this laboratory will expand on each of the chapters in this work. Improvements to the slurry formulation and fabrication method are ongoing to create scaffolds with higher strength and accuracy. The bioreactor system is in use to elucidate cellular responses to our different scaffold materials and structures. Translational medicine studies are also in progress to see how our scaffolds perform in critical defects using load-bearing *in vivo* animal models. With continued research efforts, we can improve patient outcomes and the standard of care.